NONLOCAL ACOUSTIC BLACK HOLE METASTRUCTURES: ACHIEVING

ULTRALOW FREQUENCY AND BROADBAND VIBRATION ATTENUATION

A Thesis

Submitted to the Faculty

of

Purdue University

by

Siddharth Nair

In Partial Fulfillment of the

Requirements for the Degree

of

Master of Science in Aeronautics and Astronautics

December 2019

Purdue University

West Lafayette, Indiana

THE PURDUE UNIVERSITY GRADUATE SCHOOL
STATEMENT OF THESIS APPROVAL

Dr. Fabio Semperlotti, Chair

    School of Mechanical Engineering

Dr. Jonathan Poggie

    School of Aeronautics and Astronautics

Dr. Tyler Tallman

    School of Aeronautics and Astronautics

Approved by:

    Dr. Weinong Wayne Chen

        Head of the School Graduate Program

To my family

ACKNOWLEDGMENTS

This work wouldn't be possible if not for all the help and guidance I received from a number of people at various stages of my work. I would like to take this opportunity to thank all of them for supporting me and guiding me for the successful completion of this thesis.

I would like to express my sincere gratitude to my advisor, Dr. Fabio Semperlotti, for providing me the opportunity to work on this exciting project as part of my masters thesis. I am grateful for his constant support, valuable suggestions and persistent guidance throughout the period of my masters.

I am also thankful to my thesis committee members, Dr. Jonathan Poggie and Dr. Tyler Tallman, for their invaluable comments and suggestions.

I thank all the members of Structural Health Monitoring and Dynamics Laboratory for their continuous help. Special thanks to Mr. Mehdi Jokar, PhD candidate, for extending his timely support at different stages of my work. I am grateful to Ray W. Herrick Laboratories for extending the required facilities for my project.

Lastly, I would like to thank my parents and all my family members for their unwavering support and encouragement throughout the duration of my masters degree. I am also thankful to my friends for keeping me in good spirits during my graduate school years.

TABLE OF CONTENTS

LIST OF TABLES

LIST OF FIGURES

ABSTRACT

Nair, Siddharth MS in AAE, Purdue University, December 2019. Nonlocal Acoustic Black Hole Metastructures: Achieving Ultralow Frequency and Broadband Vibration Attenuation. Major Professor: Dr. Fabio Semperlotti.

The development of novel passive techniques for vibration attenuation and control of broadband energy propagation through structural systems have been a major challenge in various complex engineering applications. These passive attenuation and control methodologies are necessary for the efficient performance of advanced lightweight aerospace and mechanical systems operating under extreme working conditions.

Acoustic Black Holes (ABH) have rapidly emerged as an effective approach to either dissipate or harvest mechanical energy in vibrating thin-walled structures. The characteristic dimension of an ABH, typically its diameter, is strictly connected to the occurrence of a cut-on frequency value below which the ABH is ineffective in absorbing the incoming wave. From a general perspective, lower the cut-on frequency, larger the ABH diameter needed to absorb the incoming wave. Design and manufacturing constraints of the host structure impose stringent limitations on the maximum ABH diameter and hence, limiting the lowest achievable cut-on frequency. The combination of these factors typically result in the poor energy extraction performance at low frequencies.

This thesis proposes the concept and explores the performance of an intentional nonlocal design for periodic grids of ABHs embedded in thin plates (referred to as ABH metastructures). The nonlocal design is conceived with the twofold objective of lowering the cut-on frequency of the ABH grids and extending the operating frequency range so as to achieve broadband performance. Different nonlocal designs are pre-

sented and their dynamic performances are investigated using numerical models. As opposed to the traditional material nonlocality, this thesis introduces nonlocal effects using an intentionally tailored geometric approach. A secondary layer is connected to the load-bearing ABH metastructure base, whose dynamic properties are sought to be controlled.

A semi-analytical model is also presented in order to characterize the role of nonlocality on the dispersion behavior and its effect on the broadband dynamic response. In linear elasticity, material nonlocality is mathematically represented by a spatially varying attenuation function. As the nonlocal model developed in this thesis follows geometric nonlocality approach, the required nonlocal attenuation factor is found to have a spatial as well as a temporal dependence. The analytical nonlocal constitutive relations in conjunction with the numerically obtained stress-strain parameters are used to identify the dynamic attenuation factor for the nonlocal ABH metastructure. The results provide substantial theoretical and numerical evidence of the potential of engineered nonlocal ABH design as an efficient ultra-low frequency passive attenuation technique for lightweight structures.

1. INTRODUCTION

1.1 A Short Overview of Vibration Attenuation and Control Methodologies

Low frequency noise and vibration is a common problem encountered in flexible lightweight designs across all engineering applications including, but not limited to, the aerospace and the automotive sectors. Industrial equipment working at low frequencies also encounter complications created by structural noise radiation [1]. The major issues associated with the vibratory response of engineering systems include stability, structure radiated noise and even structural damage of the models under consideration. More specifically:

- STRUCTURAL INSTABILITY: Stability issues in the structural elements such as aircraft propellers, turbines and jet engines, to name a few, have been a long standing challenge for the engineering community [2]. The rotor blade vibration in propellers and turbines generating an unstable rotating equilibrium is one of the most common stability problem on which engineers are still working for a solution [2, 3]. Vibration stability is an area of research even in the aerospace industry, were the rocket engine noise reflected from the ground excites and destabilizes the spacecraft structure and payloads during lift off [4]. This in turn effects the stable flight of the launch vehicle. Efficient and smooth running of all the equipment, including the rocket engines, the propeller of aircraft or the turbines of a power plant, depend on the stability achieved by eliminating the unwanted vibrations disturbing the structure [3–6].

  The stability issues due to undesirable vibrations can be devastating at times as in the case of North American P-51D airplane crash in 2011 [7]. The deterioration of a lock nut insert in this race flight resulted in the stiffness reduction

of an elevator trim system which led to an aerodynamic flutter at high speed, ending in loss of control of the flight and its eventual crash (Fig. 1.1). The aeroelastic instability or flutter is a state in which the natural frequencies of the structure are excited due to the unstable aerodynamics. Although the aircraft are usually designed within the aeroelastic stability envelope, flutters can occur when operated in configurations beyond the normal working conditions. This incident strengthened the need to study vibrations disturbing the stability of the structures.
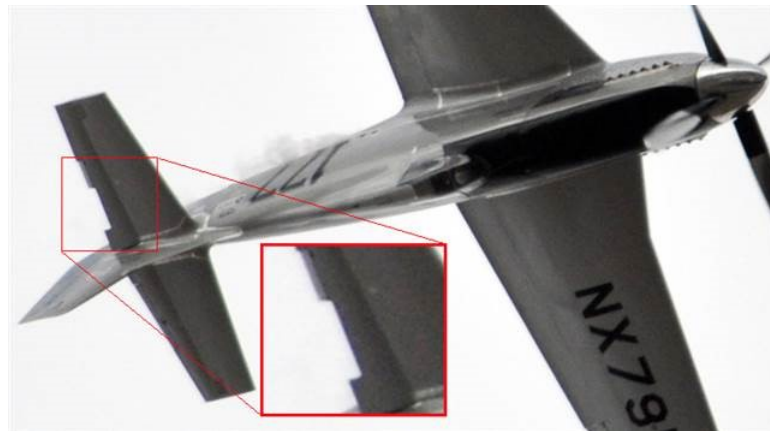
Fig. 1.1.: Aircraft P-51D Mustang right before the crash in Reno air races in 2011. Zoomed in image shows the aircraft's tail missing a key structural component. (*Source: http* : *//www.nbcnews.com/id/*44556695 *and news services*)

- NOISE GENERATION: The surface contact between different moving parts in an assembly acts as the vibration noise sources. The structure-borne noise is the most frequently encountered vibration radiated noise issue in the aircraft sector due to the excitation of the airframes. Low frequency structural excitations are encountered in vibration of rotors and gearbox of helicopters. Mechanical struts connecting the gearbox to thin walled fuselage pave way for the transmission of the above mentioned excitations to cabin, creating immense amount of cabin noise [8]. Jet noise is another common issue in these thin walled fuselage struc-

tures. The noise generated by the mixing of the turbulent flow of gases exiting jet engine with the free flowing air predominantly excites the parts of the cabin behind the engines [8].

The aircraft noise in two commercial flights were measured and compared by Ozean *et al.* [9] to understand the significance of existing cabin noise. The average noise range for parking and taxing were measured to be 58.4-65 dB(A) and 62.3-65 dB(A) respectively in both the flights. Integrating the noises of the mechanical components in takeoff, cruise and landing with the noises generated by the warning signals and announcements, the total in-cabin noise was measured to have an amplitude around 81-88 dB(A). It was found that the propeller engine based aircrafts have larger number of low frequency cabin noise sources. Most of the in flight cabin noise amplitudes were identified as values close to or well above the threshold hazardous audible range (65 dB(A)) of human health [9]. Hence, it is necessary to control thess undesirable noises.

- STRUCTURAL DAMAGE: Damage in the form of cracks or delamination of structure and its deterioration as a result of that damage is a very common failure phenomenon due to vibration [10, 11]. The pressure variation generated by the turbulent boundary flow over aircraft wings and the excitations produced by rotating aircraft engines are a major source of vibration in the aircraft structures [11]. These excitations, over a period of repeated loading cycles, initiate fatigue crack propagation. A considerable portion of the thin walled aircraft wing and fuselage life is occupied by the propagating cracks as these long cracks are sustained due to the geometry of the aircraft skin [11, 12].

  Another noteworthy incident was the crash of Braniff Airways Lockheed Electra prop engine flight in September 1959 [13]. It was learned that the rotating frequency of the flight propeller started vibrating in the resonance frequency range of the wing, opening up a crack. In time, with repeated loading, the wing tore off the fuselage making the flight plummet to the ground. Devastating incidents take place due to the lack of knowledge and poor implementation of

the vibration control and attenuation techniques. These incidents emphasize the need to dampen vibration in structures. From 1960's all the commercial flights were tested for vibration control (Fig. 1.2).
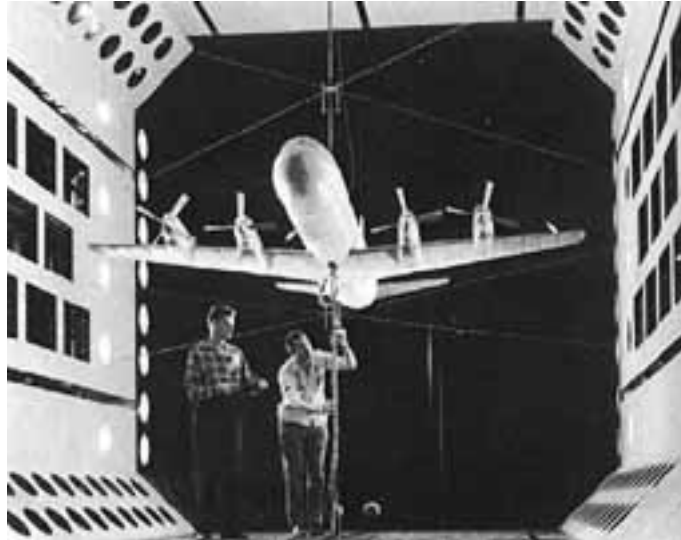
Fig. 1.2.: NASA employees testing a scaled model of Braniff Electra (1960). (*Source: http://www.hq.nasa.gov/office/pao/History/SP-440/ch6-5.htm*)

The lightweight engineering structures are designed for efficient performances with structural vibration stability and control. But even after scrutinized design phase, it is difficult to reduce the mechanical vibrations below a limit of frequency of excitation. The development of novel techniques to attenuate application specific vibrations for enhanced human comfort and extended structural health of a system is a growing field of engineering research. This can play a significant role in the cost effectiveness of the system maintenance and in providing a healthy working environment. Low and ultra-low frequency vibration attenuation has been a long standing challenge for the unimpaired working of thin walled structural mechanisms in race-cars, aircraft, helicopters and space launch vehicles [14–18]. Apart from the hindrance to the working of a given system, it also deteriorates the health of the structure in time. Hence, it is important to understand and develop an ultra-low frequency vibration attenuation technique for thin-walled structures. The available vibration control methods

can be classified into three main categories based on the fundamental principle being exploited:

1. Passive attenuation techniques:

   A vibration attenuation approach in which the interaction of the propagating structural waves with the physical structure dampens the wave energy without the use of any external energy source is termed as the passive vibration attenuation. Passive methods are generally the simplest and the cheapest damping techniques. These are easy to implement and require minimum maintenance. Various passive damping methods like the friction damping and the mass-spring damping have been implemented over the years for attenuating the high frequency excitations.

2. Active attenuation techniques:

   Active vibration control works on the principle of destructive interference of the vibration response of the parent structure using a controllable secondary source of excitation [8, 19]. An externally powered feedback system acts as the secondary source controlling the vibration response of the parent structure. An antinoise of equal amplitude with the opposite phase generated by an electromechanical or electroacoustic feedback system, in superposition with the primary (parent) noise, completely cancels the total output noise in the structure. The output response amplitude passes through the sensors in the system and is fed to the controller, which keeps constant feedback to manipulate the correct supply of the secondary damping force. Active tuned mass-damper with control algorithm [20, 21], gas pulse generators with pulse control algorithm for flexible structures [22, 23], active aerodynamic appendages to reduce the wind induced motion [24, 25] are some of the most common active attenuation methods.

   Although active attenuation methods can work at the lower frequency bandwidths with its sensitive feedback system, the implementation of these techniques are complex and costly. Bulky external power sources and feedback

systems, the necessary components of the active attenuation methods, limit the use of these techniques in the lightweight applications due to space and weight constraints. These techniques also require periodic maintenance and are susceptible to failure.

3. Semi-active attenuation techniques:

Unlike the active attenuation techniques, semi-active methods do not directly supply an external damping force on the structure, instead they maintain a control system loop to dynamically alter the damping or stiffness properties of the structure [26]. Magnetorheological dampers and piezoelectric material dampers are two common semi-active attenuation techniques [27, 28].

Although the semi-active systems do not add energy to the structure, they use small power sources to control the stiffness and damping of the system. Thus, the control loop and the sensor requirements are still the same as in the active methods, but with lower power need. Moreover, developing a controller for the semi-active damping technique and modeling the fluid behavior for it is extremely complex for the real life cases [29].

Various active and passive attenuation techniques have been developed over the years to cater the ever growing demands for reduction of unwanted excitations. The active control techniques involve external components as mentioned above and is not implicit structure generated attenuation and therefore is considered complex. Due to the operational difficulties and needs of the active methods, passive attenuation techniques are in high demand. The passive techniques do not make use of any external source to control vibration, the tailored design of the parent structure provide the implicit characteristics to attenuate the wave energy in this technique. Hence, the passive control methods are easier to implement, compared to the active attenuation methods. As it is found that most of the existing passive attenuation techniques are generally more effective for high frequency damping due to their inability to adapt to the low frequency structural characteristics, there is an evident need to develop

a novel passive vibration attenuation technique that can control the structural wave propagation at lower frequencies. Next section will elaborate on some of the commonly used passive damping techniques.

1.2   Passive Vibration Attenuation Techniques

The phenomenon of damping vibrations using the interactions of the structural waves with mechanical linkages of the physical geometry or with its material is a peculiar feature of the passive vibration attenuation technique. The knowledge of the passive attenuation methods, materials and concept implementation through novel design changes are necessary for improving the attenuation performance. Hence, it is important to understand the existing passive attenuation models. This section will focus on the principle concepts and the working characteristics of some of the existing passive damping techniques ranging from the use of viscoelastic material to the impedance interface damping models.

1.2.1   Viscoelastic material (unconstrained or free) damping

Use of a dissipating layer on the vibrating surface is a common passive damping method. Materials with high loss factors are typically preferred as added viscoelastic layer due to their high energy damping ability [30, 31]. A viscoelastic layer, an elastomer with long chain molecule, on an excited elastic structure has the ability to absorb its kinetic energy and dissipate it as heat [32]. Using the damping material provides an easy and conventional approach to attenuate the unwanted vibrations. However, making a complete structure from these materials is not feasible due to the weight constraint and varying strength requirements for specific applications. The viscoelastic materials are traditionally used for low temperature or high frequency applications as they dissipate more energy under these conditions [33, 34].

It is known that stiffness of the parent structure dominates the vibration amplitude of the system and addition of damping layer reduces the vibration by less than 10%

percentage of it, hence, in most cases there is a limit on the absorption capability of these layers [35]. Thus, vibrating structure with absorption layer efficiently attenuates at high frequencies but has its limitations in lower frequency bandwidths.

1.2.2   Tuned mass dampers

Tuning mass-spring with viscous damping or mass attached to a viscoelastic spring to negate excitation frequency response of the primary structure is another common passive damping method [36–38]. In cases like attenuating thin beam resonances, in electricity transmission lines and in case of resonance of bridges, tuned mass-spring with viscous damper system is designed to attenuate the vibrations [39]. This mass-damper system generates a region of very low amplitude vibration (anti-resonance) over several structural modes in the frequency ranges corresponding to the attenuation bandwidths of the structure [40]. Although the kinetic energy of the system at resonance will be completely absorbed by the tailored mass, stiffness, and damper, this technique adds mass to the system and is of advantage only to attenuate high resonant frequency vibrations of stationary structures [41].

1.2.3   Friction based damping

Vibrating system attached with friction dampers form another passive attenuation technique for the lightweight structures in which the auxiliary mass attached in the form of the damper mitigates the vibrations of the parent structure [42–45]. The composite sandwich panels used in the space launch vehicles are laminated with dampers in te form of *friction ledges* of carbon fiber reinforced plastic. The relative movement of these friction ledges and the composite structure casing (in Fig. 1.3) during the vibration caused delamination results in the dissipation of the excitation energy in the form of heat [46].

Particle damping technique uses a number of granular masses of tungsten carbide or ceramic material enclosed in a cavity to form a damper. A combined effect of the
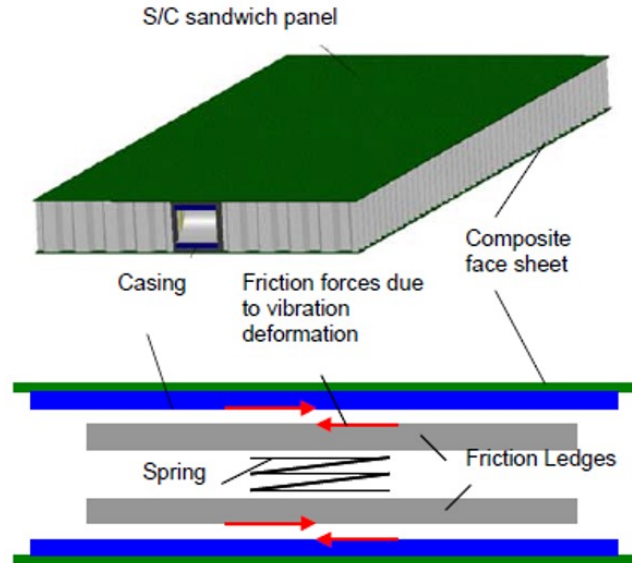
Fig. 1.3.: The relative displacements of the ledges and the composite casing produces friction based damping. *Adapted from* [46]. (*Copyright Romberg, O. et al.* [46])

momentum transfer phenomenon and the frictional loss due to the collision between the particles at the cavity boundaries are responsible for the vibration attenuation in this damper [47–50]. The particle damping method has been traditionally used in the high frequency vibration control of the beam structures [51], tennis rackets [52] and turbine blades [45]. Although the level of impact is lower in particle damping, it adds mass to the system and storage the granular masses occupies space. These friction based methods have different dampers to attenuate vibrations at high frequencies, but they remain ineffective in the low frequency regimes.

1.2.4 Constrained layer damping

The attenuation efficiency of free surface damping layer on structures is amplified by constraining it by a stiff third layer as shown in Fig. 1.9b. Here, as the damping material is sandwiched between the primary structure and the constraint layer, the shear strain generated by the constrained layer controls the wave attenuation and hence, the damping film is characterized by its complex shear modulus [53–55]. This

technique is traditionally used to attenuate flexural modes [32]. The damping layers on joints of constrained structures will enhance the wave attenuation with low weight penalty, but, similar to the above mentioned passive methods, the constrained surface damped structures attenuate only at high frequencies.
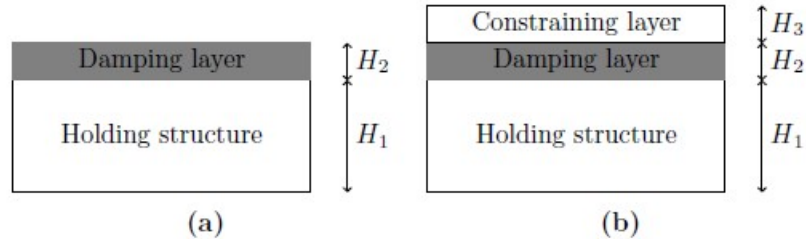
Fig. 1.4.: Schematic illustrating the surface damping techniques: (a) free damping layer (b) constrained damping layer. *Adapted from* [34]. (*Copyright Vivien Denis*)

1.2.5 Graded impedance interface damping

Different passive damping methods discussed till now use extra mass, added viscoelastic layer or friction for energy attenuation. In order to dissipate more energy in all of the above mentioned methods, the added damping material has to be bulky and efficient. On one hand there is a limit on the extra mass that can be added to the structure, while on the other hand the cost of complex, intricate and efficient designs are pretty high. Compared to the other passive damping techniques discussed in the literature till date, about 60-80% of the wave energy was attenuated (highest among all methods specified till now) without any addition of mass by employing a simple graded impedance interface at the boundaries of bars and plates [56]. The energy attenuation by this method is superior to viscoleastic damping and is obtained over wider bandwidths. Layers of different impedance stacked together create a composite structure with low reflectivity and improved damping efficiency [57]. The change in the impedance prevents the reflection of the waves from the edges of the structure and attenuates the wave energy effectively in the high frequency regime.

1.2.5.1 Geometrically tapered structures

Based on the above mentioned varied impedance interface concept and the low wave reflection characteristics, use of wedges or tapers as geometric inhomogeneities in an otherwise homogeneous structure to enhance damping is another passive attenuation technique. More recently, researchers have been focusing on the taper based structures to get better vibration damping properties without significant weight penalty. Wedges can control the wave propagation as the wave speed reduces with the varying thickness of the wedge [58]. Wedged and tapered structures have the ability to focus on the vibration attenuation in the low frequency range due to the distinctive theoretical property of zero wave reflection at the center of tapers [59, 60]. Further, it is found that enhanced low frequency attenuation characteristics are observed for tapers with larger diameter [60].

Although compared with the techniques discussed above, the tapered structures have better low frequency attenuation capability, there are some important limitations to this approach. Theoretically, ideal tapers have zero taper center thickness and can completely attenuate energy, but in practice, the residual thickness of the taper profile center will never be zero due to manufacturing and strength constraints. Hence, tapered structures cannot attenuate vibrations below a certain frequency limit. Owing to the relatively better attenuation performance of the tapered structures in the low frequencies, this thesis will try to understand the working principles of the existing tapered structures and make use of it in developing a novel passive damping technique effective in the ultra-low frequency range. Next section aims at developing a better understanding of the working of taper embedded structures.

1.3 Background on Acoustic Black Hole (ABH)

The flexural wave propagation in the tapered elastic plates have been a topic of research since the late 20th century. The wave velocity of the elastic waves propagating through varying tapered thickness decreases as they approach the center of the taper.

Internal reflection of the waves is responsible for this reduction in the wave speed. Although Pekeris [61] introduced this concept for the wave propagation in stratified fluids, Mironov [58] was among the first to explain the effect of tapers on the elastic wave propagation in structures. The study on stratified inhomogeneous medium based structure showed a linear decay in the wave velocity as the structure thickness reduces to zero [61]. It was also noted that the flexural waves traveling through the smoothly varying taper thickness propagates without any edge reflection. Mironov mathematically formulated this observation [58], he showed that a wave originating from the thicker section of the structure will take infinite time to reach the end of taper and hence, will not undergo reflection. Thus, Mironov's study theoretically explained that a plate with parabolic taper profile with residual thickness at the taper center will prevent the reflection of flexural waves completely. Special cases of this tapered plates were studied in detail by Kyrlov *et al.* [62].

$$h(x) = \epsilon x^m \tag{1.1}$$

where m$\geq$ 2.

When the taper thickness ($h(x)$) varies according to a power law relation as in Eq. (1.1), where m is the taper parameter and ϵ represents the smoothness criterion (explained in detail in the next chapter) [62], the flexural wave get confined in the taper edge and never escapes. This phenomenon is called the 'Acoustic Black Hole (ABH)' effect in structures which bears certain analogy with the better known optical black hole phenomenon in cosmology. As mentioned before, manufacturing tapers with zero residual thickness is not feasible and hence, the complete wave attenuation using ABH can never be achieved. Therefore, Eq. (1.1) is added with a term involving the residual thickness (h_{min}), representing the taper profile in real-life case [63] as shown in Fig. 1.5. Kyrlov's study provided a preliminary theoretical base on an effective flexural vibration attenuation technique using ABHs [62, 64]. In this investigation, Kyrlov demonstrated the vibration attenuation potential of the power law tapered plates coated with a thin damping layer on the surface. Thus, vibration

damping of ABH is further enhanced due to a reduction in its reflection coefficient by coating layers of viscoelastic damping material on the ABH tapers.

Feurtado et $al.$ [65] explored the effect of the high taper power, m, on the reflection coefficient and wavenumber. This work introduced the normalized wavenumber variation as a design parameter. It was observed that with an increase in the taper power (m), there was also a hike in the number of normalized wavenumbers deviating from the smoothness criterion. It was found that the violation of this smoothness criterion was an issue in the small ABHs with dimensions of the order of few centimeters in a working range up to 10kHz frequencies [65]. Independent of the working frequency, the ABH tapers with taper parameter $m = 2$ satisfies the smoothness criterion. For tapers with $m > 2$, the normalized wavenumber variation is difficult to characterize as it becomes both frequency and position dependent.
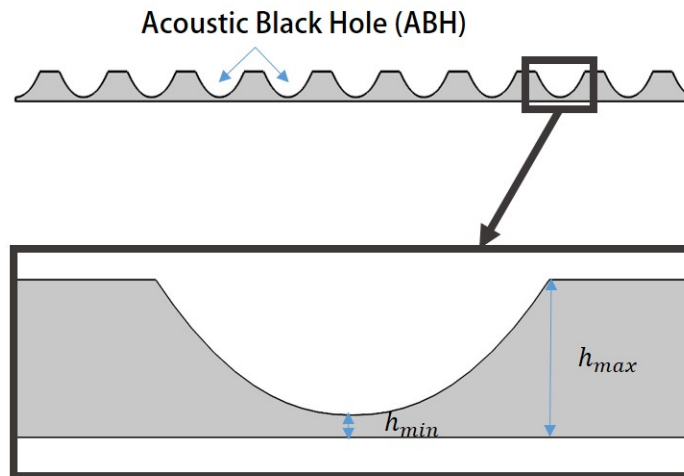
Fig. 1.5.: Two dimensional ABHs embedded plate (top) and enlarged image of a single taper with maximum thickness h_{max} and residual thickness h_{min} (bottom).

Lately, studies have shown the dependence of ABH performance on the development of local modes. Conlon et $al.$ [59] studied the characterization of structural vibration and radiated sound for low frequency responses of the ABH plates and found the dependence of the low frequency behavior on the fundamental vibration modes of the unit cells. Although at the higher frequencies the dimensions of ABH

play very less role in the wave attenuation, the ABH tapers with larger diameter holes or smaller residual thickness can control the wave attenuation properties in the low frequency ranges. Thus, the residual taper center thickness has to reduce to lower the ABH attenuation bandwidth for a taper of the given length, but manufacturing constraints limit the reduction in residual thickness. Denis *et al.* [66] studied the reflection coefficients of beams with smooth and uneven ABH terminations. The magnitude of the reflection coefficient of tapered end decreases with increase in the frequency, while the phase of the reflection coefficient indicates the wave travel time in the structure. This study defined a frequency dependent length correction for smooth taper termination. Due to the complexity in fabrication, the low residual thickness tapers end up forming ABH with some surface unevenness, Denis [67] investigated the effect of these imperfections by imitating an intentional rough taper termination. It was found that the reflection coefficient of rough tapers have higher amplitudes in comparison to the coefficient of smooth tapers. This effect is localized in a case when the damping is low and can broaden when the damping is increased. Lowering the residual thickness of tapers result, in the local modes due to the surface irregularities on it, generating traveling waves at low frequencies. The work here clearly indicates the limitation of ABH as the residual thickness of the ABH taper center cannot be lowered below a limit due to the fabrication constraint and to avoid the localized modes generated by irregular taper surface.

1.3.1   Application of acoustic black holes

The properties of ABH has been exploited for noise and vibration damping across automotive, aeronautical, and civil engineering applications. The ABH embedded structures are observed to have low wave reflection from the center of the tapers, making it a region of high energy density. Energy harvesting applications rightly exploits this property of ABHs by attaching piezo-transducers to the ABH surfaces to extract energy from these high energy density zones as shown in Fig. 1.6. In this

technique, the ABH is tailored to fit the frequency range of the energy sources [68]. Localized vibrations, low reflection coefficients, trapped modes, and low cut-off frequencies are some of the characteristic features of the ABH as shown by Pelat *et al.* [69]. The procedure for identifying the high energy density taper centers of the ABHs and incorporating an optimized position for the electromechanical circuitry needed for energy harvesting was investigated by Zhao *et al.* [70]. This study supported the claim that the center of the taper acts as a focal point of the energy focusing lens in ABH and helped design an optimal transducer network for energy harvesting. The ability of an ABH to focus the flexural energy is independent of the spectral and spatial characteristics of the extreme load applied. This knowledge helped reduce the transducer position dependent sensitivity of the harvesting system.
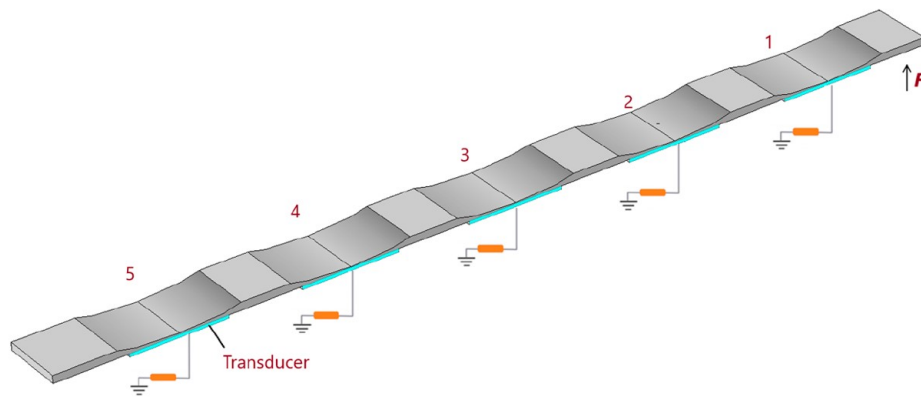
Fig. 1.6.: Schematic of piezo-transducers mounted on ABHs embedded 2D plate for energy harvesting. *Adapted from* [68, 71]. (*Copyright IOP publishing, 2014*)

Later, Krylov [72] proposed the use of 2D ABH for vibration attenuation of plates. The 2D ABHs were characterized as the symmetric cylindrical indentations following a power law taper profile with a coating of damping material on a plane plate surface. The theoretical and experimental validation for wave attenuation at the center of cylindrical tapers were provided by this investigation. The study elaborates the practical applications of ABH in turbine blades and badminton rackets. It was found that the addition of absorbing material at the center of the ABH taper center enhances

the attenuation properties effectively. The early comparisons of the attenuation performance of the ABH embedded structures with the traditional vibration attenuation methods were performed by Krylov and Bowyer [73,74]. The study introduced ABHs as the viable passive attenuation technique for the low frequency vibration damping. The self sufficient damping characteristics of the ABH introduces minimum weight penalty on the structure and thus, making it a suitable vibration damping technique for aeronautical, and automobile based engineering applications.

The application of damping structural vibrations in rotating turbines find ABH extremely apt and useful. Subsequent studies showed that covering the whole surface of blade with absorbing layer is not recommended as in traditional cases, but rather changing one of the edges of blade into an ABH with added damping layer will effectively reduce the vibration. Tapered wedges on turbine blades are shown in Fig. 1.7. Tapered bars of power law profiles are also used in tennis rackets and golf clubs. The 2D acoustic black holes can also be effectively embedded on stiffening ribs of structures without compromising its rigidity. Further, with the addition of the damping layer, these tapered structures enhance their vibration attenuation capability.
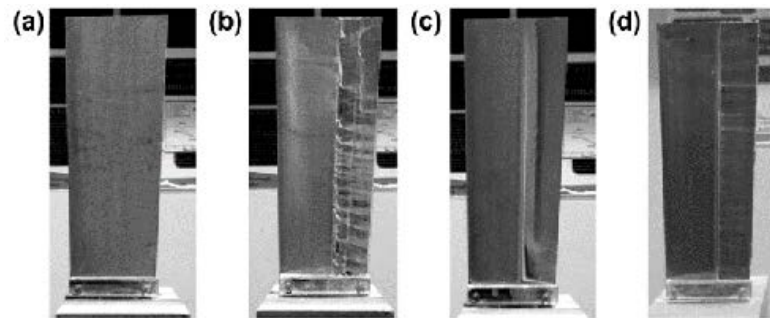
Fig. 1.7.: Flow visualization after wind tunnel testing of: (a) turbine blade, (b) turbine blade with power law wedge, (c) turbine blade with single damping layer on the power law wedge, (d) turbine blade with shaped damping layer on the power law wedge. *Reconstructed from* [71,74]. (*Copyright E.P. Bowyer and V.V. Krylov*)

Several works have studied the effect of ABH embedded elliptical plates, where a reduction in the mobility was observed when the plate was excited at its focal point [75–77]. The elliptical plates with ABH showed higher attenuation range compared

to the traditional rectangular plates due to the presence of the focal points. This investigation showed that with its ability to focus wave energy, the ABH acts as an effective damper even in complex structures. Further, Cuenca [76] in his work, also showed the effectiveness of the velocity profiles in 1D structure with its ability to control material density and Young's modulus. The same study was also conducted on the rectangular plates. All the ABH applications discussed so far effectively attenuates vibrations in the high frequency bandwidths.

As mentioned before, due to the fabrication and structural strength constraints, taper thickness cannot be reduced below certain limit. Hence, there is a lower limit for the frequencies that can be attenuated using the ABH. Besides, as reduction in the taper thickness is accompanied by taper irregularities, the lower residual thickness at the taper center of ABHs generate local resonance based responses. From the work explained in this section, it is evident that the full potential of the ABH has been extracted. In order to enhance its working range researchers developed the periodic ABH embedded structures, introduced in the next section.

1.4   Structural Periodicity and ABH Metastructures

Periodic structures have been an active field of research for sometime now. Rayleigh and Brillouin [78] were among the first to study the theoretical concepts of wave propagation in periodic structures with wavelengths comparable to the length of the structural unit cell. Investigations were also carried out on periodic beams [79, 80] as well as on the flat and stiffened plates [35]. In more recent years, the use of ABHs in periodic configurations have also been explored.

It is established that the periodic structures have the characteristic ability to attenuate certain frequency ranges due to the formation of a gap in their band structure. Mead *et al.* [35, 80] was among the first to investigate the dispersion behavior of the periodic plates stiffened with beams. The study illustrated the formation of propagating bands corresponding to the propagating wave frequencies, and bandgaps

associated with the wave attenuation frequencies on the band structure. Further, with the knowledge of the band structure, Mead performed the dynamic analysis on lightweight structures to predict and prevent the vibration induced fatigue and structure radiated noise. This study was among the first investigations on band gap formation in periodic lightweight structures. With the growing need for enhanced wave attenuation in the lightweight systems, researchers worked on the development of an artificial medium with the ability to control the propagating wave speed by introducing layers of homogeneous materials to form a composite structure called *phononic metamaterial*. In this section of thesis, we focus on the development of a *phononic metastructure* in the form of periodic ABH embedded structure and describe its characteristics. Unlike the above mentioned phononic metamaterials with stacked layers of varying material properties, the ABH metastructures alter the traditional wave propagation characteristics by introducing geometric inclusions in the form of ABH tapers with varying thickness.

1.4.1 Developement of phononic metamaterials and metastructures

The work of Rytov [81] on laminated isotropic structure was one of the very first on 1D periodic metamaterials. The investigations performed by Rytov concentrated on characterizing the electromagnetic properties of a stratified medium with alternate layers of isotropic materials embedded together to behave as an effective anisotropic medium. It was found that the use of these metamaterial in transmission lines reduced the losses in wave propagation. The inspiration from layered periodic dielectrics forming the *photonic metamaterials* was the basis for an extensive study on the elastic composite materials called the phononic metamaterials. These are composite structures with impedance differences between the layers due to density or elastic modulus dissimilarity between them [82].

An extensive literature is available on the topic of phononic crystals, acoustic metamaterials and metastructures. Interested readers can find seminal works and

reviews in [83–91]. Below, we review only the aspects that more closely relate to the topic of this research. Specifically, the studies that focused on the development of the mechanical metamaterials and metastructures for the lightweight structures. The elastic wave propagation in a composite medium of two infinite cylinders in periodic array generate frequency bandgaps as the differences in impedance control the wave propagation speed [92]. Kushwaha *et al.* [93] presented a complete calculation of the band formation of phononic metamaterials. The work describes the existence of the phononic band gaps and localization of the phonons in these acoustic gaps. In his work titled *Theory of acoustic band structure of periodic elastic composites* [94], the author provided a detailed theory of the band structure of the periodic elastic structures with material inclusions.

At the start of this decade, Liu *et al.* [95] developed a low frequency application of acoustic metamaterial, the work focused on providing an analytic model for wave propagation in a special class of three-layered composite material. The work used spheres with 3 component composite model coated with a low stiffness material in a matrix. It basically constituted of a matrix core with a soft cover as second layer and a soft shell as third layer as shown in Fig. 1.8. When excited with a waveform, this structure produced band gaps due to the local resonance of the specific layers. In this study, the author highlighted the material dependence of the structure in generating the band gaps. The study showed that the replacement of the soft layer coating by a stiffer material shifted the bandgap to a lower frequency range. It signified the importance of the properties of inclusions in generating the low frequency local resonant band gaps in a structure. This is the basis for the development of the Acoustic Black Hole (ABH) metastructures, where periodic embedded ABHs acts as the geometric inclusions with varying impedance.
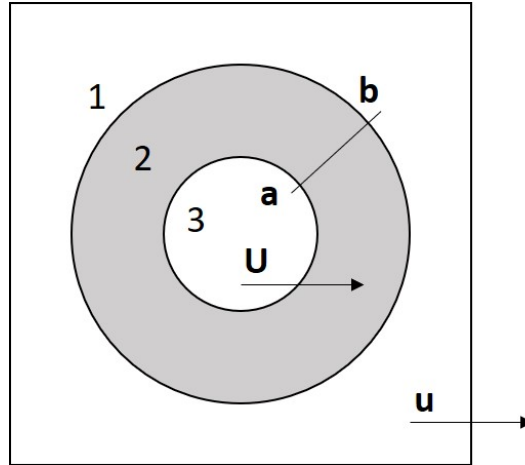
Fig. 1.8.: Schematic represents the unit cell of composite material. Mediums 1 and 3 are hard material while medium 2 is made of soft material. Arrows indicate the excitation direction for mediums 1 and 3 with respective excitation amplitudes ($\mathbf{u}$ and $\mathbf{U}$). *Adapted from* [95].

1.4.2 ABH metastructures

This section will review the attenuation performance characteristics and effectiveness of ABH metastructures in the low frequency range. Initially, the section will focus on the characteristics of periodic metastructures in general and then further, extend it to review the performance of ABH metastructures. The bandgaps in the periodic structures are generally generated by Bragg scattering, a phenomenon caused by the destructive interference of the scattered waves. However, in some cases with inclusions [96], the local resonance of a unit cell makes way for a hybridized bandgap. Yong *et al.* [79] in their work on flexural wave propagation in beams, had shown both the resonant type and the Bragg type bandgaps can co-exist. This work introduced the bandgap coupling phenomenon in which the large gap is formed due to a combination of the spatial periodicity and the local resonance. In the low frequency range, this bandgap is controlled by the variable local unit cell properties and is less sensitive to the structural periodicity.

The work by Zhu *et al.* [63] showed the existence of the above mentioned hybridized band gaps in ABH metastructures. This work used acoustic black hole embedded thin

plate in the lattice structure. Apart from the band gaps created by the periodicity in the structure, the unit cell of the ABH metastructure generated band gaps due to the local resonance of the ABH tapers. Further, Liu *et al.* [95] observed the local resonant frequencies of the unit cell to be two order of magnitudes smaller than the Bragg scattered bandgap frequencies. Thus, the ABH taper characteristics will control the low frequency attenuation properties of the metastructure. Later, Zhu *et al.* [63] also described a procedure to control the local bandgaps by tailoring the ABH taper diameter. Compared to the complex laminated elastic composite structures with varying impedance layers, the ABH metastructures are simple but effective designs [95].

The bandgaps of ABH metastructures with zero wave (group) velocity in the fundamental frequency range [97], exhibit some common properties of the bandgaps created by local resonance like negative group refraction index [98], wave filtering [99], acoustic cloaking [100] and mode anisotropy. Hence, the ABH metastructures have remarkable vibration and noise attenuation capabilities over range of frequencies.

Although the ABH metastructures generate low frequency bandgaps due to the local resonance of the ABH tapers, the dependence of these local resonant frequencies on the residual taper center thickness as mentioned in the previous section limits the low frequency attenuation range. The thesis proposes the integration of nonlocal elasticity concepts and the ABH metastructures to overcome this limitation. The upcoming sections will review some basic concepts of the nonlocal elasticity theory as a guide-way to conceive a combined effect of nonlocality and ABH metastructures.

1.5   A Short Introduction to Nonlocal Elasticity

The principle goal of this section is to briefly explore the motivation behind the development of the nonlocal elasticity theory and review the basic concepts of the theory. Nonlocal responses are prominent in several structures ranging from porous media like soil [101, 102], to biomedical materials like bones [103]. Further, the nonlocal behavior of fatigue based cracks are common in most mechanical systems [104, 105].

In the classical elasticity theory, it is approximated that stress at a point is only dependent on the strain at the same point. This holds true for most of the macro sized isotropic homogeneous structures in the real world, but as materials of varied length scales coexist in several applications as in atomic devices, sensors, and nano-electromechanical devices, the response diverges from the classical theory and exhibits the existence of long range cohesive forces within an area of influence. Hence, in order to encapsulate the elasticity concepts at all length scales, the nonlocal elasticity theory was introduced.

Eringen was among the first to develop a complete mathematical formulation of nonlocal elasticity [106]. Interested readers can refer to other seminal works on nonlocal elasticity formulations for further details [107–109]. Recently, numerous integral methods [110, 111], gradient methods [112, 113], and peridynamic approach [114, 115] based theories have been developed to capture the long range interactions in nonlocal structures. The integral model formulates the nonlocal effect by defining the nonlocal material properties as a distance dependent function using a convolution integral in the stress-strain relations [111]. Added strain gradient based terms in the constitutive relations define the nonlocal behavior in a gradient based method [113]. In the integral formulation developed by Eringen, constitutive relations were derived based on a localization residual which accounts for the interactions of all the points in the area of influence and its effect on a local material point on the structure. Later, Nowinski [116] extended this theory and formulation to nonlocal homogeneous plate structures. For an isotropic homogeneous structure the nonlocal strains are negligible and matches with the classical elasticity theory in the limit case. This work aims to use the features of nonlocality on ABH metastructures through a tailored geometry.

1.6   Limitations of Existing Vibration Attenuation Techniques

The discussions presented in the sections above highlighted several limitations of the existing passive vibration techniques. The major drawbacks are summarized below:

- Most of the passive attenuation techniques, including but not limited to the use of friction based dampers or constrained surface treatments, deteriorates the structure as they follow the principle of energy transfer by the relative motion between two surfaces in physical contact. Development of fatigue cracks results in the degradation of the performance of the structure due to the repeated rubbing motion of the surfaces in contact. Besides, these techniques add weight to the system and attenuates efficiently only in the high frequency regime.

- Other passive methods (e.g. tuned vibration absorber) tend to be effective only at a single target frequency and for stationary inputs, while their performance deteriorates rapidly in the presence of transient loads.

- Application of damping layer on the vibrating surface has been a reliable passive attenuation method. But this technique, depending on the extent of the damping required, adds weight to the structure due to the thick material coating and hence, have restricted application in the lightweight structures.

- As the active or semi-active attenuation techniques involve the use of costly feedback systems with bulky external power sources, the use of these damping methods are restricted by the space and weight constraints in the lightweight structures.

- Among the existing passive attenuation methods, the ABH metastructure was developed as an effective low frequency vibration damping technique for the lightweight systems. These metastructures have the added advantage of damping excitations by the local resonance of the tapers apart from the vibration

damping caused by the spatial periodicity of the structure. The local resonant frequencies, controlled by the diameter of the ABH tapers, developed this attenuation technique as a suitable method for low frequency damping, but the design limitation in reducing the taper diameter due to the fabrication and structural strength constraints restrict the application of this technique for vibration damping in the ultra-low frequency range.

1.7 Thesis Objectives

After studying the available literature on ABH metastructures and existing vibration damping techniques, the author could reflect upon the absence of in depth work for extending the application of ABH metastructures to ultra-low frequency vibration attenuation. Among the existing techniques, some active and semi-active attenuation techniques are capable of attenuating in the ultra-low frequency ranges, but these methods are difficult to implement in the applications involving lightweight structures due to the limitations specified in the previous section.

The broad objective of this dissertation is to design, numerically simulate and analytically study a novel ABH metastructure based nonlocal model for vibration control and attenuation of lightweight structures in the ultra-low frequency range. Further, specific objectives of the proposed approach can be listed as following:

(A) **Enhanced broadband vibration attenuation:**
   The engineered nonlocal behavior of the ABH metastructure is expected to amplify the vibration attenuation frequency bandwidths of the system in comparison to the attenuation bandwidths produced by the traditional ABH metastructures.

(B) **Ultra-low frequency vibration damping:**
   The nonlocal ABH metastructure design is also expected to extend the low frequency attenuation performance characteristics of the traditional ABH metas-

tructures to the ultra-low frequency regime. The existing passive attenuation techniques have limited applicability in the extremely low frequency range.

(C) **Reduced cut-on frequency:**

The introduction of intentional long range connections on the ABH metastructure design is also believed to lower the cut-on frequency of the system.

The specific objectives hypothesized above will be verified by implementing a technical methodology to design and analyze the performance of the proposed idea. This methodology is further classified into two sub-objectives as follows:

1. **Development of the nonlocal geometry:**

The work focuses on introducing a novel design of *nonlocal ABH metastructures* as a means to overcome the above mentioned limitations of the existing passive attenuation techniques. The design methodology exploits the characteristics of the traditional ABH metastructures and creates artificial long range connections via added hierarchical layers.

A simple example of this design approach is shown in Fig. 1.9. The unit cell of an ABH metastructure shown in Fig. 1.9 (top) is assumed as the baseline design. The addition of a tailored top layer connected with rigid links on this baseline structure is expected to produce a system as shown in Fig. 1.9 (bottom). The baseline geometry is the load-bearing member of this system, while the non load-bearing top layer with the rigid connectors link distant points on the baseline structure. Thus, these long range connections are expected to introduce a geometric nonlcality on the baseline ABH metastructure. The nonlocal designs developed in this thesis will be similar to the sample design shown in Fig. 1.9.

2. **Performance analysis of the nonlocal ABH metastructure:**

The static and dynamic behavior of the nonlocal ABH metastructure will be studied numerically and analytically. The numerical simulation results are expected to segregate the characteristic behavior of the nonlocal ABH metastructure from the baseline ABH metastructure design based on the damping
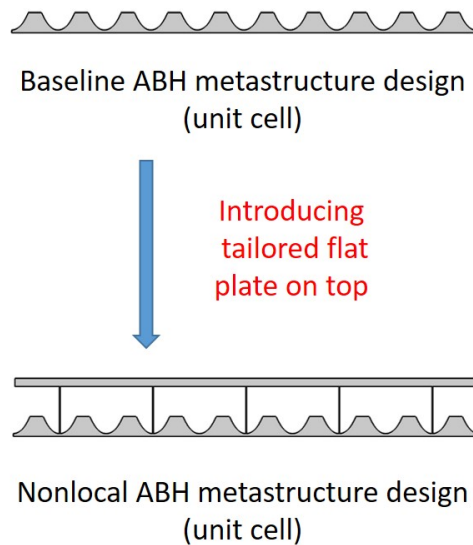
Fig. 1.9.: Schematic showing the developement of a nonlocal ABH metastruture (bottom) design based on a baseline ABH metastructure design (top).

frequencies, attenuation bandgaps and cut-on frequencies. Further, a nonlocal elasticity theory based semi-analytical approach will be proposed to capture the dynamic behavior of the nonlocal geometries and is expected to verify the numerically obtained nonlocal characteristics.

1.8   Thesis Outline

The thesis focuses on demonstrating the effectiveness of a nonlocal ABH metastructure design for vibration attenuation in the ultra-low frequency regime. The initial part of Chapter 1 studies the existing attenuation methodologies and motivates the need for a novel passive attenuation technique for ultra-low frequencies. The chapter continues presenting a review of the background concepts of the ABH metastructures and the nonlocal elasticity.

As the thesis exploits the properties of the ABH metastructures by introducing geometric inhomogeneities in it, Chapter 2 focuses on the fundamental principles and

on the characterization of ABH and ABH metastructures. The final part of Chapter 2 briefly introduces the theoretical background of the numerical simulation setups required for analyzing the performance of the new designs.

Chapter 3 develops a semi-analytical approach to extract the dynamic nonlocal properties of the system. As the traditional nonlocal elasticity equations for thin plates were developed for structures with nonlocal materials, this chapter of the thesis focuses on modifying the analytical formulations to capture the dynamic behavior of the tailored nonlocal geometry. Based on the modified analytical formulations, a semi-analytical procedure for calculating the dynamic nonlocal factors is developed.

The initial part of Chapter 4 introduces all the designs and elaborates the procedure for designing these nonlocal ABH metastructures. Later, the chapter continues to discuss the results of numerical simulations and analyze, and compare the dynamic performances of the individual designs. A comparison is drawn between the attenuation performances of the nonlocal ABH metastructures based on the damping frequencies, attenuation bandgaps and cut-on frequencies obtained. Lastly, the semi-analytical nonlocal factors obtained in Chapter 3 is matched with the numerical simulation based results in this chapter.

Chapter 5 summarizes all the numerical and analytical work. This conclusive chapter focuses on elaborating the major contributions of this dissertation. It also provides a road-map of the future work that could be implemented for enhanced efficiency of the novel ultra-low frequency passive vibration attenuation methodology.

2. FUNDAMENTALS OF ACOUSTIC BLACK HOLE AND ABH METASTRUCTURES

Acoustic black holes are an integral part of the work presented in this thesis. Literature presents ABH metastructures as an effective passive vibration attenuation approach for lightweight composite structures [73, 74]. Understanding the working principles of the ABH is decisive in extending the potential of ABH tapers to lower frequencies. Hence, this chapter explores the theoretical and experimental behavior of the ABH along with a review of its performance. The initial part of the chapter explores the concept of an ABH in 1 dimension. Then, the description is extended to two dimensional ABHs. The section continues with a summary of the reviews from the literature illustrating the experimental implementation and the performance characteristics of ABH embedded in thin 2D structures. The final part of the chapter briefly explores the theoretical background of the methodologies followed to simulate the performance of ABH metastructures.

2.1 One Dimensional Acoustic Black Hole

The basic working principle of ABH can be presented by understanding the wave propagation in a wedge, as shown in Fig. 2.1. The physical principle exploited in the ABH was extended to acoustics by Mironov [58], the study observed that flexural waves in a thin plate with exponentially tapered thickness will theoretically never reflect back, forming a *zero reflection wedge*. Thus, researchers discovered the existence of a peculiar taper profile in which the waves propagate with asymptotically decaying wave speed as it nears the taper extremity. Theoretically, the flexural waves are not reflected as thickness tend to zero at the center of this taper. This taper profile is often termed as an ABH in 1D. The mathematical proof for the existence of

parabolic taper profile with asymptotically reducing wave speed was first presented by Mironov [58] and it will be reported in this chapter for completeness. Later, this section also helps in visualizing the wave propagation in 2D ABHs with the assistance of geometric acoustics principle explored in the work done by Krylov [72]. The last part of this section also explores the effect of added viscoelastic damping layers on 1D tapers [72].
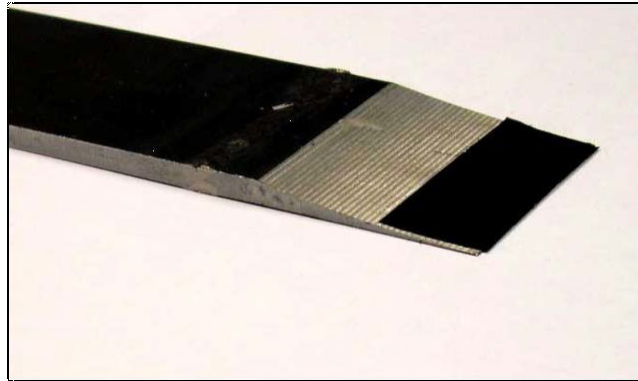
Fig. 2.1.: A 1D acoustic black hole with a damping layer near the center of taper for bending wave attenuation along the taper length. *Adapted from* [72]. (*Copyright Victor V. Krylov*)

2.1.1 Governing equation of a 1D zero reflection wedge

Based on the earlier work from Mironov [58], the mathematical formulation for wave propagation through tapers in non-reflecting wedges and 1D ABHs will be explored below.

The following theoretical relations were derived by Mironov for a wave of amplitude A, traveling through a thin plate structure of maximum thickness h:

$$k = \frac{3\rho\omega^2}{Eh^2(x)} \tag{2.1}$$

$$A = A_0\left[\frac{h_0}{h(x)}\right]^{\frac{3}{4}} \tag{2.2}$$

where ω is the angular frequency, ρ is the material density, E is the Young's modulus and A_0 is the wave amplitude at minimum thickness of taper h_0. Here, x represents the wave prorogation direction in 1D ABH. The Eq. (2.1) represents the local wavenumber (k) variation of the propagating wave in the structure. Further, on applying the law of conservation of energy to the elastic wave traveling through varying taper thickness, the amplitude A of propagating wave can be derived as a function of varying taper thickness $h(x)$ as in Eq. (2.2).

Based on the argument that the change in the wavenumber must be smaller than the propagating wavelength for a steady traveling wave without backscattering, Mironov [58] developed a smoothness criterion for the ABH taper profiles as formulated below:

$$\frac{1}{k^2}\frac{dk}{dx} \ll 1 \tag{2.3}$$

Further, substituting the Eq. (2.1) in Eq. (2.3), we get:

$$\frac{1}{2}\left(\frac{El}{3\rho\omega^2}\right)^{\frac{1}{4}}\frac{1}{h^{1/2}}\frac{dh}{dx} \ll 1 \tag{2.4}$$

The mathematical constraint formulated in Eq. (2.4) must be satisfied for an efficient taper design. It was found that the smoothness criterion was satisfied by a power law profile of the form $h(x) = \epsilon x^m$, that vanishes over a finite interval x for the taper parameters $m \geq 2$. This power law equation is the varying thickness profile $(h(x))$ of ideal taper designs used in the ABH, but a modified taper profile equation is used for the real life applications of ABH.

2.1.1.1 Effect of the residual taper thickness

The taper thickness profile formulation for an ideal ABH was revisited in the previous section. Since manufacturing a smooth taper with zero taper center thickness is impossible, complete wave attenuation using ideal ABH can never be achieved. It was found that for practical purposes the thickness at the center of taper will never

be zero and will always have a minimum residual thickness. Hence, the taper profile
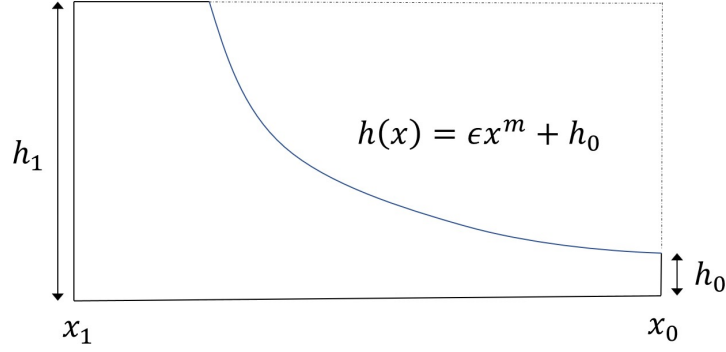
Fig. 2.2.: Schematic illustrating the taper profile of a 1D acoustic black hole with residual taper thickness h_0.

equation suggested by Mironov was modified in literature [62,117] with an extra term incorporating the residual taper thickness (h_0) as shown in Fig. 2.2, the mathematical representation of the taper profile in all the real-life cases is as follows [63,118]:

$$h(x) = \epsilon x^m + h_0 \tag{2.5}$$

Similar to the ideal ABH profile, the taper profile with residual thickness in Eq. (2.5) must also satisfy the smoothness criterion $\epsilon=(3\rho\omega^2/E)^{\frac{1}{2}}$ for m≥2 to maintain a steady reduction in phase and group velocities as wave propagates to the center of taper [63]. Considering the wave propagation through the updated taper profile (Eq. (2.5)), the variation in the local wavenumber $(k(x))$ can be defined as [70]:

$$k(x) = 12^{1/4}k_l^{1/2}(\epsilon x^m + h_0)^{-2} \tag{2.6}$$

$$k_l = \frac{\rho(1 - \nu^2)\omega^2}{E} \tag{2.7}$$

where $k_l = \omega/c_p$ and $c_p = 2c_t\left[1 - \dfrac{c_t^2}{c_l^2}\right]^{\frac{1}{2}}$. Here, k_l is the longitudinal wavenumber of the propagating wave in ABH taper, c_p is its phase velocity, c_l and c_t are the

longitudinal and the shear wave velocities respectively. The angular frequency of the wave is defined as $\omega = 2\pi f$, where f is the linear wave propagation frequency, and ν is the Poisson's ratio.

From Eq. (2.6), it is known that the wavenumbers vary as a function of the spatial coordinate x and is independent of the frequency characteristics of the incoming wave [68]. As x increases, the value of the local wavenumber $k(x)$ propagating through the varied thickness reduces. In the limiting case of the taper profile (i.e $h_0 = 0$), the local wavenumber in Eq. (2.6) nears infinity and the wave phase matches with the characteristics of the ideal ABH tapers.

Mironov [58] studied another interesting feature of the ABH taper, describing the spatial variation of the wave speeds. In this work, he defines the local bending stiffness (D) of a 1D ABH embedded thin plate of thickness h as $D = Eh^3/(12(1 - \nu^2))$ [58]. Further, Krylov [62] used this stiffness relation to derive the following phase (c_p) and group (c_g) velocity equations:

$$c_p = \sqrt[4]{\frac{E}{12\rho(1 - \nu^2)}} \sqrt{\omega(\epsilon x^m + h_0)} \qquad (2.8)$$

$$c_g = \sqrt[4]{\frac{4E}{3\rho(1 - \nu^2)}} \sqrt{\omega(\epsilon x^m + h_0)} \qquad (2.9)$$

Both the phase (c_p) and group (c_g) velocities tend to zero as the spatial coordinate x approaches zero (ideal case) in Eq. (2.8-2.9) and thus, verifying the characteristic property of zero reflection from taper center of an ideal ABH. In ideal conditions the taper center will act as a point of high energy density, but in the case of ABH tapers with residual thickness, the energy propagating wave is reflected from the taper center and has lower energy density.

2.1.1.2   Calculation of the reflection coefficient (R_0)

The reflection coefficient has proved to be an exact measure of the efficiency of an ABH, lower the reflection better the attenuation performance of the design [119]. For an ABH taper with a quadratic shape profile $h(x) = \epsilon x^2 + h_0$, the reflection coefficient amplitude is given as [62]:

$$R_0 = e^{-2 \int_{x_0}^{x_1} Im(k(x)) dx} \tag{2.10}$$

where R_0 is the reflection coefficient, x_0 is the x-coordinate of the taper center, x_1 is the x-coordinate at the thick edge of the taper and $Im(k(x))$ represents the imaginary component of the local wavenumber $k(x)$.

An infinitely small damping, defined by $Im(k(x))$, results in the zero reflection co-efficient in an ideal ABH (i.e $x_0 = 0$). Whereas, reflection coefficient R_0 of higher amplitude is calculated for tapers with residual thickness due to the larger imaginary component of the wavenumber. A small change in x_0 enhances R_0 by as much as 10%. Krylov [62, 72] investigated the effects of residual thickness on the wave attenuation properties of the ABH and found that the reflection coefficient values were as high as 50-70% due to the presence of residual taper thickness. This introduced the need for an extra damping material on the ABH tapers to attenuate the reflected waves.

2.1.1.3   Integration of viscoelastic damping layers

The vibration attenuation performance in ABHs with residual taper thickness is enhanced by coating layers of viscoelastic damping materials on the tapers for reduc-ing the reflection coefficient of the geometry [64]. The material loss factor (ν), defined as the ratio of the energy dissipated to the maximum strain energy stored, represents the effectiveness of a viscolelastic damping layer for a given material. Higher damping is associated with the higher material loss factor. As the absorption of the incident flexural waves predominantly occur at the taper extremities, it is sufficient to attach a thin viscoelastic damping layer at the center of the taper profile to maximize the

wave attenuation performance of the ABH embedded structures. Using the damping material for attenuation is a traditional technique and it is known that the in-plane deformations of the added layer is responsible for this film induced absorption. The in-plane deformations of the absorption layer under the impact of flexural waves on the taper surface is as follows:

$$u_x = -z\left(\frac{\partial^2 u_z}{\partial^2 x}\right) \tag{2.11}$$

where u_x is the deformation in the x-direction, z is the length in the z-direction and $\left(\frac{\partial^2 u_z}{\partial^2 x}\right)$ is the curvature of the shear deformation in the x-z plane.

The reflection coefficient for flexural wave propagation in ABH coated with thin layer of viscoelastic material is calculated by using the geometrical acoustic approximations [62]. For a thin plate of thickness h with an added absorption layer of thickness δ, the corrected loss factor (ξ) is given as [62] [120]:

$$\xi = \frac{\nu}{1 + (\alpha_2 \beta_2(\alpha_2^2 + 12\alpha_{21}^2))^{-1}} \tag{2.12}$$

where ν is the material loss factor of the viscoelastic layer, $\alpha_2 = \delta/h$, $\beta_2 = E_2/E_1$, $\alpha_{21} = (1 + \alpha_2)/2$ and E_1, and E_2 are the Young's modulus of the plate and the viscoelastic layer respectively.

The expression in Eq. (2.12) is further simplified by assuming a viscoelastic material coating on both the surfaces of the ABH taper. Taking $\alpha_2\beta_2 << 1$ as $\alpha_2 = \delta/h << 1$ due to the use of thin damping layer, the corrected loss factor in the reduced form is:

$$\xi = 6\alpha_2\beta_2\nu = 6\frac{\delta}{h}\frac{E_2}{E_1}\nu \tag{2.13}$$

Using Eq. (2.13), the local wavenumber ($k(x)$) is obtained. For further reference, the complete derivation is provided in [117]. The imaginary part of the $k(x)$ is of the form:

$$Im(k(x)) = \left(\frac{12^{1/4}k_p^{1/2}}{h(x)^{1/2}}\right)\left(\frac{\eta}{4} + \frac{3}{2}\frac{\delta}{h(x)}\frac{E_2}{E_1}\nu\right) \tag{2.14}$$

In order to calculate the reflection coefficient, the integral in Eq. (2.10) is evaluated after substituting Eq. (2.14). For simplicity, we assume the ideal quadratic taper profile $h(x) = \epsilon x^2$ with the damping layers attached on either sides of the taper. The obtained reflection coefficient is given as follows:

$$R_0 = e^{(-2\mu_1 - 2\mu_2)} \tag{2.15}$$

where;

$$
\begin{aligned}
\mu 1 &= \frac{12^{1/4} k_p^{1/2} \eta}{4\epsilon^{1/2}} \ln \frac{x_1}{x_0} \\
\mu 2 &= \frac{3.12^{1/4} k_p^{1/2} \nu \delta}{8\epsilon^{3/2}} \frac{E2}{E1} \frac{1}{x_0^2} \left(1 - \frac{x_0^2}{x_1^2}\right)
\end{aligned}
\tag{2.16}
$$

It is observed that the additional absorption layers further reduce the reflection coefficient based on the loss factor of the added film. The equations of μ_1 and μ_2 (Eq. (2.15-2.16)) were evaluated for thin (δ) viscoelastic layers. Thus, these equations have the limitation of failing under the use of thick absorption film or when the residual taper thickness is insignificant. Further, a general mathematical approach overpowering this limitation was developed for calculating the flexural wave reflection coefficient of ABH tapers attached with arbitrary thickness of the damping layer. This approach generates a reflection coefficient for general cases with rather complex numerical integration.

It is proved that the values of the reflection coefficients of tapers with thin absorption layers are significantly lower than the reflection coefficients of the ABH tapers without a damping layer. The relations in Eq. (2.15)- Eq. (2.16) with general taper parameters of the damped ABH, calculated reflection coefficients R_0 values as low as 1-3 %. Krylov *et al.* [121] verified the theoretical formulations of the damped ABHs by experimentally studying the mobilities on a damped wedge with quadratic taper profile.

2.2 Two Dimensional Acoustic Black Hole

Two dimensional acoustic black holes can be adjudged as cylindrical pits carved on a flat plate as shown in Fig. 2.3. These forms of cylindrical indentations on a flat plate were studied by Kyrlov [119].

It is convenient to use the geometrical acoustics in Hamiltonian formulation to study the bending wave propagation in thin plates with 2D tapers. As the 2D structure with cylindrical indentations has no geometrical anisotropy, application of Hamiltonian approach is simple to analyze the wave propagation velocity in these structures. It

Fig. 2.3.: A 2D acoustic black hole in the form of circular indentation for flexural wave attenuation. *Adapted from* [72]. (*Copyright Victor V. Krylov*)

can be shown that the incident ray trajectories (as per geometrical acoustics) of the waves propagating through the cylindrical indentations is as follows:

$$\frac{dr}{d\theta} = r \frac{1}{\tan \alpha}$$
$$\frac{d\alpha}{d\theta} = -1 - \frac{r}{n} \frac{\partial n}{\partial r} \qquad (2.17)$$
$$nr \sin \alpha = constant$$

These equations are in the polar reference frame with r and θ coordinates measured along the middle plane of the plate as shown in Fig. 2.4. Assuming a bending wave vector $\mathbf{k}$, α is angle between r and $\mathbf{k}$. Further, the bending wave refraction index in the taper area is defined as $n(r) = c_0/c(r) = h_0^{1/2}/h(r)^{1/2}$ where c_0 and $c = c(r)$

are wave phase velocities in a constant plate thickness h_0 and tapered local thickness $h(r)$ respectively as in the one dimensional case. The final expression in Eq. (2.17) is the Snell's law formulated for the axisymmetric case.

An excitation point outside the taper is marked as the starting point of the ray trajectory with properties r_0, α_0 and $n_0 = 1$ and a point inside the taper (near to the center) marking the end of the ray trajectory with properties r,α and n (Fig. 2.4) will follow Snell's law as formulated below:

$$nrsin\alpha = r_0sin\alpha_0 = \rho \tag{2.18}$$
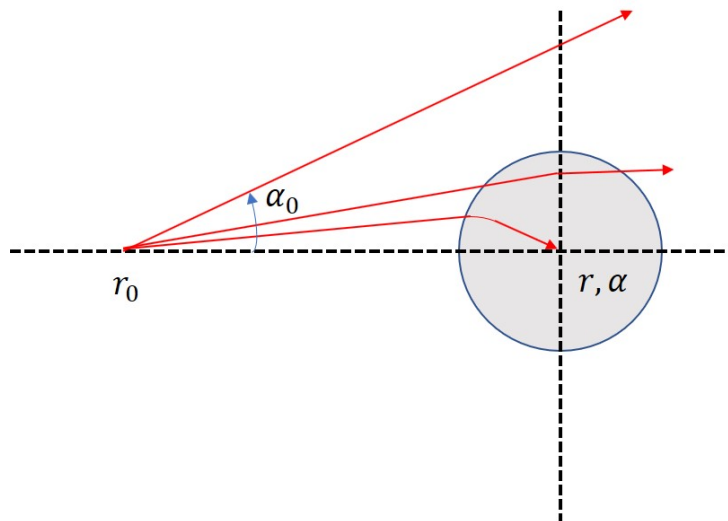
Fig. 2.4.: Three ray trajectories illustrating the propagation of flexural waves over a taper profile indentation. Bottom most ray is trapped at the center of taper and has zero reflection coefficient theoretically. *Adapted from* [119].

In Eq. (2.18), a constant impact parameter $\rho = n_0 r_0 sin\alpha_0$ is introduced for a given α_0. The combination of r_0 and α_0 specifies the distance between the straight line ray trajectory and the center of the polar coordinate reference in the absence of the taper. In the presence of the taper profile on the 2D plate structure (shown by a circle in Fig. 2.4), these ray trajectories would no longer remain on a straight path. Analyzing the above equation for wave propagation in symmetric cylindrical indentations with a

power exponential $m >= 2$, all rays with $|\rho|$ less than a critical value (even with direct ray i.e $\rho = 0$) will deflect towards the center of the taper in a direction normal to it as shown in Fig. 2.4. As the major contribution to reduce the reflection coefficient is from the center of the taper, towards which rays get deflected, all the 2D ABH reflection coefficient calculations follow the 1D ABH reflection coefficient calculation procedure and hence, is not presented here [119].

These 2D ABHs in the form of cylindrical pits will not reflect any wave deflected towards its center and hence, engraving these indentations on a plate or shell will enhance its structural damping performance substantially. An array of ABHs can be manufactured on thin plates to amplify this effect and the number and taper dimensions are only be limited by the constraints of the specific application.

2.3   Practical Implementation and Characteristics of ABH

The sections on 1D and 2D ABHs detailed above helped in understanding the theory behind the working of ABH profile with and without additional damping layer. This section focuses on reviewing some major results of numerical simulations, and experimental studies conducted on ABHs and thus, validating the analytical work for its practical implementation.

A 1D rectangular plate with a wedge at one end and a similar rectangular plate covered completely in damping material were experimentally and numerically compared to understand the attenuation performance of each of the damping techniques [122]. It was found that the incorporation of a power law based taper profile produces enhanced damping in frequency ranges where the effect of viscoeleastic layers alone were insignificant. Thus, ABH embedded on a flat plate has higher attenuation capacity than a damping layer on the same flat plate. It was also learned that the application of damping material on the ABH enhances the vibration attenuation capacity of the ABH further.

Later, experiments were conducted to locate the optimal position of damping mate-

rial on tapers for efficient attenuation. The addition of a damping layer at the thicker taper edge has minimal effect, while the wave attenuation performance enhances as the damping layer is moved towards the taper center. Application of damping film away from the taper center does not enhance wave attenuation but rather increases the total mass of the structure. It was also found that the lower the value of the ratio between absorbtion film and the taper thickness, lesser is the damping efficiency in the higher frequency bandwidth. This study also showed that the application of the damping layer on the taper center of the ABHs reduces the wave speed in the mid and high frequency ranges, while the addition of the damping layer on ABH does not significantly improve the ultra-low frequency (fundamental modes) damping [123].

Experiments were further carried out to analyze the attenuation performance of rods embedded with quadratic power profile 2D tapers [124]. It was observed that the rods completely covered by damping layers alone had minimal attenuation characteristics, while the taper ended rods coated with damping layer attenuated wave propagation significantly. This also supports the theoretical observation of low reflection coefficient for damped ABHs. This technique was later implemented on badminton rackets where the handles of rackets were incorporated with damping film on taper ended rods [125]. The results showed 10 dB reduction in the racket handle vibrations at high frequencies.

The attenuation performance of beams and elliptical plates embedded with 2D tapers were also experimentally investigated [77]. Similar to the 1D tapered structures, it was observed that the addition of damping layer on 2D ABH embedded beams and plates help in enhancing their vibration attenuation capability. It was found that the larger the material loss factor of the added absorption layer, lower the coefficient of reflection and better the attenuation performance of ABH embedded structures.

2.4   Mathematical Models Analyzing the Response of ABH Metastructure

The previous chapter reviewed the literature on periodic ABH embedded structures known as ABH metastructures. It was noted that the introduction of periodic ABHs enhanced the vibration attenuation performance of the system. Therefore, with the background of ABH from the above sections, the author would like to review the dispersion and steady state frequency mathematical models as tools analyzing the performance of the ABH metastructures in this section.

Consider an isotropic 2D thin plate embedded with periodic distribution of 1D ABH tapers under plane strain condition as shown in Fig. 2.5. The plate has a thickness h_1 with a taper profile $h(x) = \epsilon x^m + h_0$, where h_0 is the residual taper thickness. The 2D thin plate with ABH in Fig. 2.5(a) is the unit cell which repeats itself to form the periodic ensemble of ABH metastructure (Fig. 2.5(b)).
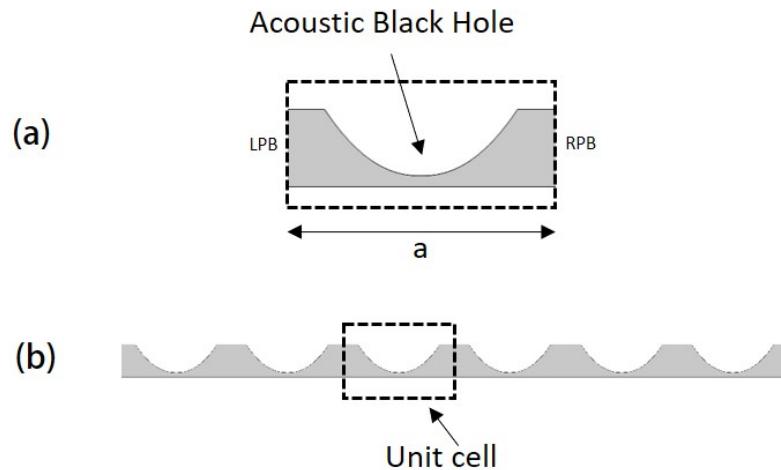
Fig. 2.5.: The schematic represents the sample models of: (a) a unit cell of ABH embedded thin plate with left periodic boundary (LBP) and right periodic boundary (RPB), and (b) an ABH metastructure obtained after assembling six unit cells.

The elastodynamic response of this ABH metastructure is governed by the Navier's equation as given below [63]:

$$\rho\frac{\partial^2\mathbf{u}}{\partial t^2} = \nabla \cdot (\mathbf{C} : \varepsilon) \tag{2.19}$$

where ρ is the density, $\mathbf{u}$ is the displacement vector, $\mathbf{C}$ is the stiffness tensor and $\varepsilon = \frac{1}{2}\left[(\nabla\mathbf{u})^T + \nabla\mathbf{u}\right]$ is the strain tensor. Traction-free boundary conditions $\mathbf{T} = \sigma(\mathbf{r}) \cdot \mathbf{n}(\mathbf{r}) = 0$ are applied on the upper and lower surfaces of the structure (Fig. 2.5(b)) in Eq. (2.19), where $\mathbf{n}(\mathbf{r})$ is the normal vector to the surface, $\sigma(\mathbf{r})$ is the local stress tensor and $\mathbf{r}$ is the position vector from the center of the ABH taper.

2.4.1 Dispersion analysis

The dispersion relations of the 2D ABH metastructure is derived from Eq. (2.19) after application of traction free boundary conditions and fourier series expansion of the material stiffness tensor ($\mathbf{C}$). Interested readers can refer to the works of Zhu *et al.* [63] and Hou *et al.* [126] for complete derivation. The application of fourier expansion and fourier transform (in time) on Eq. (2.19) yields the following dispersion relation:

$$-\rho\omega^2\mathbf{u} = \nabla.(\mathbf{C} : \varepsilon) \quad , \qquad -i\omega = \lambda \tag{2.20}$$

where ω is the circular frequency and λ represents the eigen frequency values.

Further, using the Bloch theorem, the wave function ($\boldsymbol{\phi}$) at the periodic boundary of the structure (Fig. 2.5(a)) is given by [127]:

$$\phi(x + Na) = \phi(x) \tag{2.21}$$

where N is a positive integer and a is the length of the periodic unit cell. For an uniform periodic chain with constant length of the periodic unit cell, the wave function (ϕ) can be generalized in terms of the structural displacement $\mathbf{u}$ [127]. The

generalized displacement relation for a periodic unit cell of the structure is given by the Floquet boundary condition as follows:

$$\mathbf{u}(x + a) = \mathbf{u}(x)e^{-i\mathbf{k}a} \tag{2.22}$$

where $\mathbf{u}(x + a)$ is the displacement at the right periodic boundary, $\mathbf{u}(x)$ is the displacement at the left periodic boundary, $\mathbf{k}$ is the wavenumber vector of the traveling wave and a is the periodic unit cell length.

Substitute the Floquet boundary condition (Eq. (2.22)) in the dispersion relation (Eq. (2.20)) and solve for λ to obtain the eigenfrequencies of the ABH metatsructure. The corresponding eigenvectors represent the mode shapes of the structure. A detailed description of the dispersion analysis along with the characteristics of dispersion curves are presented in the appendix.

2.4.2 Steady state forced frequency analysis

Similar to the dispersion relation obtained from the Navier's equation (Eq. (2.19)), a forced frequency response formulation of the ABH metastructure can also be derived from Eq. (2.19) with an additional forcing term integrated to account for the external harmonic excitation. On substituting the Fourier expansions and applying Fourier transform in time on Eq. (2.19), we obtain the following relation:

$$-\rho\omega^2\mathbf{u} = \nabla.(\mathbf{C} : \boldsymbol{\varepsilon}) + \mathbf{F}e^{i\psi} \tag{2.23}$$

where $\mathbf{F}$ is the amplitude of the external force vector and ψ represents the phase of the harmonic excitation. Here, $\mathbf{F}$ can be a point load or a distributed load. The relation in Eq. (2.23) is solved for different frequencies (ω) to obtain the forced response $\mathbf{u}$ of the ABH metastructure.

In specific cases when enforced displacements are supplied in place of external forces (i.e $\mathbf{F} = 0$) in the frequency domain, Eq. (2.23) reduces to the characteristic dis-

person relation Eq. (2.20). The reduced equation is then solved with the supplied displacement as the initial condition.

In this thesis, we use low reflecting boundary condition to evaluate the forced frequency dynamic response of the ABH metastructure as the low reflecting boundary condition limits the variation in the structural response due to the spurious boundary reflected flexural waves.

The differential formulations of dispersion and forced frequency analysis are difficult to solve analytically for varied range of frequencies and hence, the performance of all the structures developed in this work are numerically simulated in a FE based software called COMSOL.

2.5   Summary

Theoretically, the complete elimination of wave reflection using ABH is viable, but in practice none of the techniques developed so far has the capability to enhance the wave attenuation beyond the limitations governed by the manufacturing constraints of minimum residual taper thickness and smoothness of the taper profile. Lot of engineering applications require the use of rigid structures to maintain the stiffness and strength of the system, but ABH has its limitations in such applications. Although the use of ABH metastructure is an efficient passive damping technique in the high and mid frequency regimes, there is an ever mounting need for enhancing its attenuation in the ultra-low frequency range. From the knowledge gathered in the previous sections of this chapter, it is learned that the 1D ABH metastructure has a distinctive wave propagation pattern in which the wave passes through the individual ABH and makes the periodic system an effective broadband absorber. Hence, 1D ABH metastructure is chosen as a baseline design in this thesis. Later chapters in this thesis work on enhancing the potential of ABH metastructures with the help of a modern elasticity theory known as *nonlocal elasticity*. The mathematical models developed in the final section of this chapter can be numerically extended to evalu-

ate the performance of the new nonlocal 1D ABH metatstructure designs in further chapters.

3. EFFECTIVE PROPERTIES IN GEOMETRICALLY NONLOCAL STRUCTURES

The discussions in previous chapter illustrated the effectiveness of the ABH absorbers above the cut-on frequency along with their rapidly degrading performance at ultra-low frequencies. In the following chapter, we will present a novel design of an ABH metastructure that leverages intentionally designed nonlocality to improve the vibration absorption performance. In order to perform numerical analysis of this novel structure and to characterize its dynamic performance, we also develop appropriate technical procedures in this chapter.

The mechanical behavior of solids are illustrated by the atomic lattice theory and the continuum based classical elasticity theory [107]. It is well known that the classical elasticity theory considers internal forces in a structure as contact forces having zero long range interactions. As real materials tend to have cohesive forces over finite or infinite ranges, the classical elasticity theory fails to accurately capture their dynamic effects [107]. In order to overcome this drawback, a theory of nonlocal elasticity was formulated to incorporate the cohesive forces within a finite range. Similar to the lattice theory, the nonlocal elasticity theory introduces distance dependent kernel based effective material properties of the continuum [128, 129].

This thesis explores the use of nonlocal elasticity in conjunction with ABH metastructures. Section 3.1 introduces the concepts of nonlocal elasticity according to the works of Eringen [106] and Nowinsky [116]. Section 3.2 focuses on developing a semi-analytical formulation to capture the dynamic behavior of nolocal ABH metastructures, while another part of the section focuses on applying these formulations to solve the dispersion relations.

3.1 Fundamentals of Nonlocal Elasticity Theory

We start reviewing the nonlocal elasticity formulation introduced by Eringen [106] for a 1D solid. Then, we discuss the extension of this theory for 2D structures based on the work carried out by Nowinski [116]. A complete overview of the constitutive relations for 2D solids and related material parameters are also presented in this section.

3.1.1 Linearized nonlocal formulation for 1D wave propagation

Consider a homogeneous and isotropic thin infinite plate structure. According to the theory of classical elasticity, the constitutive equations relating stress and strain at a given point is expressed as follows:

$$\tau_{xx} = e_{xx}(2\mu_x + \lambda_x) \tag{3.1}$$

where τ_{xx} is the normal stress in x-direction, μ_x and λ_x are the Lame's material constants at a given point x, and $e_{xx} = \frac{\delta u}{\delta x}$ is the strain in the x-direction where u is the displacement in x-direction. Eq. (3.1) is further simplified as:

$$\frac{\tau_{xx}}{2\mu_x + \lambda_x} = \frac{\partial u}{\partial x} \tag{3.2}$$

Analyzing Eq. (3.2), it is evident that τ_{xx} at a given point is dependent only on the strain $\frac{\delta u}{\delta x}$ at the same point. As mentioned before, this is not the case for all the physical systems. Unlike classical mechanics, nonlocal continuum mechanics postulates that the stress at a point in a structure is influenced not only by the strain at the point but also by the strain distribution throughout the volume of the structure. Eringen formulated stress-strain constitutive relations for nonlocal elastic media, using a nonlocal residual function called the *nonlocal attenuation factor* (α) that relates the local stress with the nonlocal strain distribution [106]. The nonlocal attenuation

factor is a function of displacement and deformation gradient of all the points on the structure.

$$\frac{\tau_{xx}}{2\mu_x + \lambda_x} = \frac{\partial u}{\partial x} + \int_{-\infty}^{\infty} \alpha(|x - \xi|)\frac{\partial u}{\partial \xi}d\xi \tag{3.3}$$

Eq. (3.3) is one of the common representations of the nonlocal elasticity theory for a 1D design. The integral term in Eq. (3.3) captures the total nonlocal strain acting at the point x. Note that the integral is the weighted summation of the strains at all points on the structure (Fig. 3.1). The weight ($\alpha(|x - \xi|)$) assigned to every point ξ, based on the distance from point of stress measurement x, is the nonlocal attenuation factor. The functional form of the nonlocal kernel was obtained by Eringen [106] by enforcing functional invariance on the homogeneous and isotropic continuous formulation given in Eq. (3.3). The nonlocal attenuation factor can be a nonlinear function for inhomogeneous, anisotropic, and nonlocal elastic solids. Here, we assume a homogeneous and isotropic material for the reference structure for which the constitutive equations are invariant under transformations. Therefore, these constitutive relations (Eq. (3.3)) have only a linear dependence on the local (x) and nonlocal (ξ) coordinates via the relative distance between them, $\delta\xi' = |x - \xi|$. This concept can also be extended to higher dimensional structures [116].
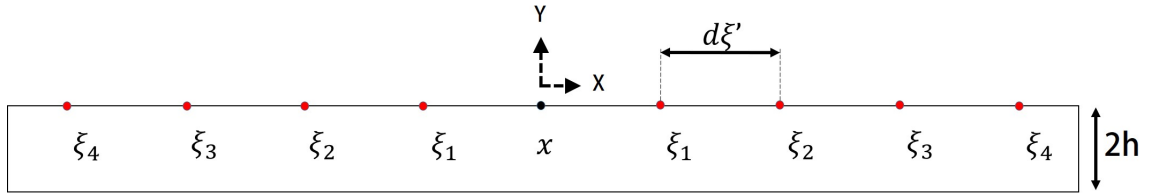
Fig. 3.1.: Schematic representing the local and nonlocal coordinates in a 1D structure with $2h$ thickness. Local point x is at the center of the structure and all the nonlocal points ξ_i are at a distance $\delta\xi' = |x - \xi_1|$ from the adjacent point.

3.1.2 Nonlocal formulation and disperion relation for wave propagation in plates

Eringen [106] developed the nonlocal formulation using a distance dependent attenuation function that controls the contribution of nonlocal strains at a location ξ_i on the stress of a given point x. For a homogeneous plate, the stress at x only depends on the strain at the point x and it is independent of the strains at ξ_i (as in classical elasticity). In such case, the attenuation factor reduces to a delta function which is unity at the point x and zero everywhere else. This property is indeed consistent with the main assumptions of Eringen's theory. It can be assured that for a homogeneous plate with local properties, the attenuation function tends to zero and therefore the integral in Eq. (3.3) will be insignificant. Thus, in the limit case, the nonlocal relation converges to the classical stress-strain relation. Whereas, a plate with nonlocal material properties will generate a significant attenuation factor value with non-zero integral term.

Nowinski [116] used the nonlocal model developed by Eringen (Eq. (3.3)) to derive the dispersion curves for an infinite plate having nonlocal material properties. According to this model, we assume a rectangular plate of thickness $2h$ (Fig. 3.1) with the mid-plane of the structure coinciding with the xz plane of the coordinate system and the wave front propagating in the x-direction. Time dependent displacements of the plate structure due to flexural vibrations are set as $u_x = u_x(x, y, t)$ in the x-direction, $u_y = u_y(x, y, t)$ in the y-direction, and $u_z = 0$ in the z-direction, while the corresponding strains are given as follows:

$$
\begin{aligned}
e_{xx} &= \frac{\partial u_x}{\partial x} \\
e_{yy} &= \frac{\partial u_y}{\partial y} \\
e_{xy} &= \frac{1}{2}\left(\frac{\partial u_x}{\partial y} + \frac{\partial u_y}{\partial x}\right)
\end{aligned}
\tag{3.4}
$$

where e_{xx} and e_{yy} are the normal strains in the x and y-directions, and e_{xy} is the shear strain in the xy plane. The generalized constitutive relations for 2D nonlocal plate, as defined by Nowinski [116], is given in tensor notation as:

$$\tau_{ij} = 2\mu e_{ij} + \lambda e_{kk}\delta_{ij} + \int_S (2\mu' e'_{ij} + \lambda' e'_{kk}\delta_{ij})dS' \tag{3.5}$$

where $i, j, k \in [x, y]$, τ_{ij} is the total stress tensor at the local point, e_{ij} and e'_{ij} are the local strain tensor and the nonlocal strain tensor respectively, μ and λ are the Lame's constants, and μ' and λ' are the nonlocal elastic moduli that depend on the distance between the arbitrary point and the measurement point according to $\mu' = \mu'(|x - \xi_x|, |y - \xi_y|)$ and $\lambda' = \lambda'(|x - \xi_x|, |y - \xi_y|)$.

For dynamic problems, the stress-strain relations (Eq. (3.5)) are a function of both space and time. The double Fourier transform of the relations in Eq. (3.5) (taken in both time (t) and space (x)) generates nonlocal constitutive relations in the frequency (ω) and wavenumber (k) domain. The transformed constitutive relations are defined in the frequency-wavenumber domain as follows [116]:

$$\overline{\tau}_{xx} = -ik(2\mu + \lambda)\,\overline{u}_x + \lambda\frac{\partial\overline{u}_y}{\partial y} + \int_{-h}^{h}\left[-ik(2\mu'_* + \lambda'_*)\,\overline{u}'_x + \lambda'_*\frac{\partial\overline{u}'_y}{\partial y}\right]d\xi_y$$

$$\overline{\tau}_{yy} = (2\mu + \lambda)\frac{\partial\overline{u}_y}{\partial y} - ik\lambda\,\overline{u}_x + \int_{-h}^{h}\left[(2\mu'_* + \lambda'_*)\frac{\partial\overline{u}'_y}{\partial y} - ik\lambda'_*\,\overline{u}'_x\right]d\xi_y \tag{3.6}$$

$$\overline{\tau}_{xy} = \mu\left(\frac{\partial\overline{u}_x}{\partial y} - ik\overline{u}_y\right) + \int_{-h}^{h}\mu'_*\left[\frac{\partial\overline{u}'_x}{\partial y} - ik\overline{u}'_y\right]d\xi_y$$

where the barred quantities represent values in the frequency-wavenumber domain, ω is the circular frequency, k is the wavenumber, $\mu'_* = \mu'_*(k, |y - \xi_y|)$ and $\lambda'_* = \lambda'_*(k, |y - \xi_y|)$ are transformed nonlocal Lame's constants.

The equilibrium equations for the nonlocal elastic material defined by the constitutive relations in Eq. (3.5) can be described as:

$$\frac{\partial \tau_{xx}}{\partial x} + \frac{\partial \tau_{xy}}{\partial y} - \rho \frac{\partial^2 u_x}{\partial t^2} = 0$$
$$\frac{\partial \tau_{xy}}{\partial yx} + \frac{\partial \tau_{yy}}{\partial y} - \rho \frac{\partial^2 u_y}{\partial t^2} = 0$$

$$(3.7)$$

Applying the double Fourier transform on Eq. (3.7), we obtain the equilibrium equations in the frequency-wavenumber domain (Eq. (3.8)).

$$-ik\, \overline{\tau}_{xx} + \frac{\partial \overline{\tau}_{xy}}{\partial y} + \rho \omega^2\, \overline{u}_x = 0$$
$$-ik\, \overline{\tau}_{xy} + \frac{\partial \overline{\tau}_{yy}}{\partial y} + \rho \omega^2\, \overline{u}_y = 0$$

$$(3.8)$$

The barred quantities in Eq. (3.7-3.8) are defined in the transformed domain.

The exact solution for $\overline{u}_x$, $\overline{u}_y$ in the frequency-wavenumber domain is obtained by substituting Eq. (3.6) in Eq. (3.8) and then, solving the developed coupled integro-differential equations. The exact solution present serious mathematical challenges, hence approximate methods are typically used. According to the classical continuum theory, a Dirac delta function is used as a mathematical representation of the particle interactions due to their zero effective range. In nonlocal elasticity, various mathematical functions can represent the effect of the inter-molecular forces. Here, a δ-sequence is employed, $\delta_n(y - \xi_y)$ with n=1,2..., which at n near infinity becomes a Dirac delta function, $\delta(y - \xi_y)$. Following Nowinski's work [116], we make two assumptions:

(a) for significantly large values of the unit cell length (l) (larger than the inter-particles interaction distance), it is acceptable to make the following substitution:

$$\int_0^l f(\xi_y)\delta_n(y - \xi_y)d\xi_y \approx \int_{-\infty}^{\infty} f(\xi_y)\delta(y - \xi_y)d\xi_y$$

$$(3.9)$$

(b) for n≫1, $\delta_n(y - \xi_y)$ acquires the shifting property, characteristic of the δ-function

$$\int_0^l f(\xi_y)\delta_n(y - \xi_y)d\xi_y \approx f(y) \tag{3.10}$$

Based on these assumptions, the nonlocal material properties for a given frequency are set in Eq. (3.6) as a function of the wavenumber alone as $\mu'_* = \mu'(k) \cdot \delta_n(|y - \xi_y|)$ and $\lambda'_* = \lambda'(k) \cdot \delta_n(|y - \xi_y|)$. Thus, the updated Lame's constants for the whole structure are:

$$\mu_{total} = \mu + \mu'(k) \tag{3.11}$$

$$\lambda_{total} = \lambda + \lambda'(k) \tag{3.12}$$

3.1.2.1 Rayleigh-Lamb dispersion relations for nonlocal waveguides

Knowledge of the updated nonlocal parameters is critical to implement the approach presented in the previous section. Here, assumed approximate solutions of the form $\overline{u}_x = U_x(k)e^{-\alpha y}$ and $\overline{u}_y = U_y(k)e^{-\alpha y}$ are used. The displacements in the frequency-wavenumber domain are obtained by substituting the approximate solutions in Eq. (3.6) and then in Eq. (3.8). Thereafter, setting the determinant of the system of equations to zero yields the nontrivial solutions of the form:

$$\begin{aligned}
\overline{u}_x &= A\ \sinh(\nu_1 y) + B\ \cosh(\nu_1 y) + C\ \sinh(\nu_2 y) + D\ \cosh(\nu_2 y) \\
\overline{u}_y &= B\kappa_1\ \sinh(\nu_1 y) + A\kappa_1\ \cosh(\nu_1 y) + D\kappa_2\ \sinh(\nu_2 y) + C\kappa_2\ \cosh(\nu_2 y)
\end{aligned} \tag{3.13}$$

where $\nu_1 = \left(k^2 - \rho\frac{\omega^2}{\Gamma_3}\right)^{\frac{1}{2}}$, $\nu_2 = \left(k^2 - \rho\frac{\omega^2}{\Gamma_1}\right)^{\frac{1}{2}}$ and $\kappa_n = \frac{i\alpha_n(\Gamma_1 - \Gamma_3)}{\alpha^2\Gamma_1 - k^2\Gamma_3 + \rho\omega^2}$ with $\Gamma_1 = 2\mu_{total} + \lambda_{total}$, $\Gamma_2 = \lambda_{total}$ and $\Gamma_3 = \mu_{total}$.

$$\overline{\tau}_{yy}\Big|_{z=\pm h} = 0, \quad \overline{\tau}_{xy}\Big|_{z=\pm h} = 0 \tag{3.14}$$

Further, substituting the solutions (Eq. (3.13)) in the transformed constitutive relations (Eq. (3.6)) and by applying the traction free boundary conditions (Eq. (3.14)), we obtain the classical *Rayleigh-Lamb* equations for symmetric and antisymmetric modes:

Symmetric mode:

$$\frac{\tanh(\nu_1 h)}{\tanh(\nu_2 h)} = \frac{4\nu_1\nu_2 k^2}{(\nu_1^2 + k^2)^2} \tag{3.15}$$

Antisymmetric mode:

$$\frac{\tanh(\nu_1 h)}{\tanh(\nu_2 h)} = \frac{(\nu_1^2 + k^2)^2}{4\nu_1\nu_2 k^2} \tag{3.16}$$

These are transcendental equations whose solution provide the so-called dispersion relations linking the frequency and the wavenumber. By using the nonlocal constitutive relations presented above, the *Rayleigh-Lamb* equations provide the dispersion relations for the nonlocal structure. In the following sections, we focus will on the antisymmetric modes given that the flexural modes are more easily excited in the practical applications of thin plate structures.

3.2 Geometry Induced Nonlocality and Nonlocal Attenuation Factor

The previous section presented a summary of the nonlocal theory for thin plates as presented by Eringen [106] and Nowinski [116]. From the above summary, it is evident that the determination of the nonlocal attenuation factor is a key element to implement this theory. In this section, we develop a semi-analytical approach that builds upon the nonlocal elasticity theory and is capable to determine the attenuation factor for the nonlocal ABH metastructures. Once this factor is obtained, the modified nonlocal Lame's constants are determined according to Eq. (3.11)-(3.12). All the nonlocal elasticity relations reviewed in the previous section are calculated using these nonlocal material properties.

In this work, we introduce nonlocality via a specific geometric design. The first part of this section will focus on presenting the concept of geometry-induced nonlocal effect

in ABH metastructures. The second part of the section will present the procedure to extract the nonlocal attenuation factors of all nonlocal ABH metastructures.

3.2.1 Introducing the geometric nonlocal effect

We first use a simple example based on a discrete spring-mass model to illustrate the general idea behind the nonlocal geometric design. The continuous designs used for the practical implementation of this concept will be described in detail in the next chapter.

Following the work of Di Paola *et al.* [130], a local discrete medium can be characterized as a series of linear elastic springs with constant stiffness, while the long range interactions for a nonlocal discrete model can be captured by linear elastic springs with distance-decaying stiffness. The nonlocal effect is introduced by connecting every point mass n to the adjacent $(n-1, n+1)$ masses and also to non-adjacent masses $(n-2, n+2)$ using the distance decaying elastic springs as shown in Fig. 3.2. The springs connecting adjacent masses have stiffness K^l, while the non-adjacent masses are connected by springs with distance decaying stiffness, $K^{nl} = K^l f(|x - \xi|)$. Here, K^l is the local spring stiffness between adjacent masses, K^{nl} is the nonlocal spring stiffness between non-adjacent masses and $f(|x - \xi|)$ is a decaying function of the distance between the mass at x and the point mass at ξ. The authors theoretically showed that this discrete model can accurately replicate the constitutive relations and the equilibrium equations formulated by Eringen's nonlocal theory. This discrete system is valid for infinitesimal values of Δx (distance between two point masses) and hence can be implemented for finite element analysis of continuous systems like beams and plates. This general concept proposed by Di Paola for a discrete system is taken as the basis to develop physical designs of nonlocal ABH metastructures. A possible implementation of this idea in the form of a continuous system is schematically shown in Fig. 3.3 [130].
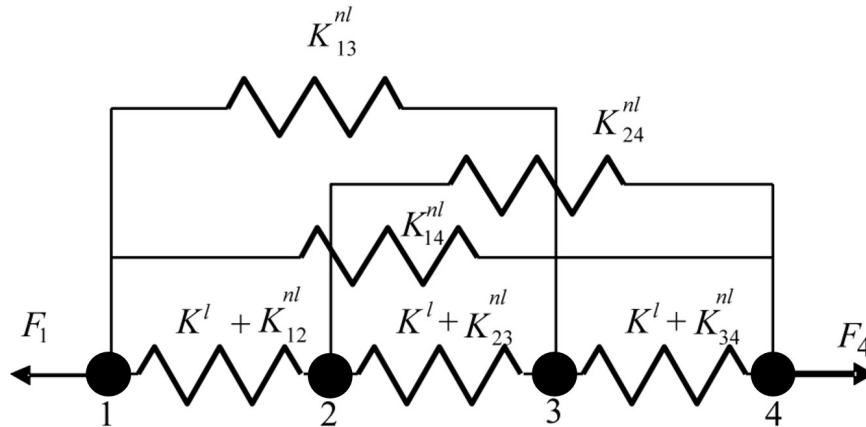
Fig. 3.2.: Discrete spring mass system with nonlocal linearly elastic spring of distance decaying stiffness, representing the framework of nonlocal geometry design. *Adapted from* [130]. (*Copyright M. Di Paola, G. Failla and M. Zingales*)
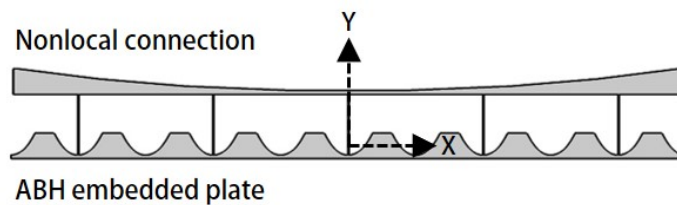
Fig. 3.3.: ABH metastructure at the bottom with nonlocal connections on top. A continuous model based on the discrete spring-mass nonlocal system.

The continuous model (Fig. 3.3) is intended to produce nonlocality by means of a tailored geometric design. More specifically, we introduce artificial connections between different ABH units to achieve this result. These connections implemented via a set of rigid links are conceptually analogous to the long-range interactions in the traditional nonlocal materials and the second layer can potentially host a secondary ABH embedded thin plate. Note that this second layer does not serve a structural (i.e. load bearing) role and it is mainly used to control the degree of nonlocality. The connections play a dual role: 1) they allow to create complex energy propagation paths through the structure, and 2) they enable every ABH indentation to contribute to the global dynamics, independent of their spatial location. In some regard, the

connecting layer tends to spatially delocalize the effect of individual ABH. This basic design concept serves as the foundation for the geometric nonlocal plate designs that will be explored in the following chapters.

3.2.1.1   Nonlocal attenuation factors

The model presented in section 3.1.2, based on the theory of Eringen [106] and Nowinski [116], needs nonlocal material properties to be provided as input. Hence, in order to leverage this formulation in conjunction with the proposed geometrically nonlocal design, we must obtain the equivalent nonlocal properties of the design. The central role of the nonlocal attenuation factor in determining the nonlocal properties was mentioned in the previous section. Earlier, Eq. (3.3) highlighted that in the classical nonlocal material theory the nonlocal attenuation factor ($\alpha(|x-\xi_x|, |y-\xi_y|)$) is only a function of the geometric distance. On the contrary, in the present work, the material properties of the nonlocal ABH metastructures do not have explicit nonlocal characteristics. In fact, the nonlocal behavior is introduced by a purely geometry based design. Also, in this case it is realistic to envision that the attenuation factor will involve the geometric parameters as well as the dynamic behavior of the ABH metastructure. In other terms, we expect the attenuation factor to be a function of both space and time ($\alpha(|x - \xi_x|, |y - \xi_y|, t)$). It follows that the general form of the constitutive equation used for the nonlocal ABH metastructure design can be written as:

$$\tau_{ij} = (2\mu + \lambda)(e_{ij} + e_{kk}\delta_{ij} + \int_S \alpha(|x - \xi_x|, |y - \xi_y|, t) \ (e'_{ij} + e'_{kk}\delta_{ij})dS') \qquad (3.17)$$

where $\alpha(|x - \xi_x|, |y - \xi_y|, t)$ is the nonlocal attenuation factor for the 2D plate, and all the other parameters were previously defined in Eq. (3.5). Comparing Eq. (3.5) and Eq. (3.17), we get the nonlocal material properties $\mu' = \alpha(|x - x'|, |y - y'|, t) \ \mu$ and $\lambda' = \alpha(|x - \xi_x|, |y - \xi_y, t|) \ \lambda$ as a function of the nonlocal attenuation factor, $\alpha(|x - \xi_x|, |y - \xi_y|, t)$, of the developed design.

All the models used in this work are based on plane strain assumptions, and it is learned that bending stress is the dominant component in the low frequency regime. Considering Kirchhoff's thin plate theory for pure bending [131, 132], we assume that the stress in the y-direction (i.e through the thickness) in low frequency regime is negligible compared to stress in x-direction. Thus, assuming plane wave propagation in 1D, the constitutive relation of thin plates can be simplified as:

$$\tau_{xx} = (2\mu + \lambda)\Big[\ e_{xx} + \int_x \alpha(|x - \xi|, t)\ e'_{xx}\ d\xi\ \Big] \tag{3.18}$$

This modified constitutive equation (Eq. (3.18)) forms the basis to extract the nonlocal attenuation factor, $\alpha(|x - \xi_x|, |y - \xi_y|, t)$. For simplicity and ease of calculation, we separate the nonlocal attenuation factor in two main components:

1. **Static nonlocal attenuation factor**

   The static stress τ_{xx}^s at a point x of the nonlocal ABH metastructure is related to the time independent local (e_{xx}^s) and nonlocal $(e'_{xx}{}^s)$ strains at points x and ξ_i. The characteristic distance dependent kernel, here named as the *static nonlocal attenuation factor* (α_s) is given by:

   $$\tau_{xx}^s(x) = (2\mu + \lambda)\Big[\ e_{xx}^s(x) + \int_x \alpha_s\ e'_{xx}{}^s(\xi)\ d\xi\ \Big] \tag{3.19}$$

   On comparing Eq. (3.19) with Eringen's nonlocal formulation (Eq. (3.3)) for static stress analysis, we have $\alpha_s = \alpha(|x - \xi|)$.

2. **Dynamic nonlocal attenuation factor**

   The constitutive relation accounting for the dynamic behavior of the nonlocal ABH metastructures can be formulated as:

   $$\tau_{xx}(x, t) = (2\mu + \lambda)\Big[\ e_{xx}(x, t) + \int_x \alpha_d\ e'_{xx}(\xi, t)\ d\xi\ \Big] \tag{3.20}$$

   where α_d is defined as the *dynamic nonlocal attenuation factor*. On comparing Eq. (3.20) and Eq. (3.18), we know that $\alpha_d = \alpha(|x - \xi|, t)$. Observing that the

static and dynamic nonlocal attenuation factors vary only by the time period dependent behavior of the metastructure, α_d can be represented as a function of α_s as:

$$\alpha_d(|x - \xi|, t) = \alpha_s(|x - \xi|) \cdot u(t) \tag{3.21}$$

where $u(t)$ is the time dependent displacement profile of the nonlocal ABH metastructure.

Following Nowinski's work [116], the constitutive relation in Eq. (3.20) is double Fourier transformed with respect to space-time $(x-t)$ into the wavenumber-frequency $(k - \omega)$ domain to understand the dynamic effect of nonlocal geometry through a frequency based study as given below:

$$\overline{\tau}_{xx} = -ik(2\mu + \lambda)\left[\,\overline{u}_x + \alpha_d(k, \omega)\,\overline{u}'_x\right] \tag{3.22}$$

where all barred parameters are assumed in the transformed domain.

Comparing Eq. (3.22) with Eq. (3.6), the nonlocal Lame's constants of the new geometry are $\mu'(k) = \alpha_d(k, \omega)\mu$ and $\lambda'(k) = \alpha_d(k, \omega)\lambda$. Given the updated nonlocal Lame's constants, we can rewrite the overall material properties in Eq. (3.11)-(3.12) as:

$$\mu_{total} = \mu + \mu'(k, \omega) = \mu\,(1 + \alpha_d(k, \omega)) \tag{3.23}$$

$$\lambda_{total} = \lambda + \lambda'(k, \omega) = \lambda\,(1 + \alpha_d(k, \omega)) \tag{3.24}$$

Here, $\alpha_d(k, \omega)$ is the dynamic nonlocal attenuation factor in the transformed domain, hence as a function of wavenumber and frequency. Using the inverse Fourier transform in the wavenumber domain, the dynamic nonlocal attenuation factor can be presented in the spatial-frequency domain as $\alpha_d(|x - \xi|, \omega)$.

The following section, will focus on the development of a semi-analytical procedure to determine α_s and α_d. A detailed procedure to capture the static attenuation

factor is described on the basis of Eq. (3.19). The procedure to extract the dynamic attenuation factor is presented afterwards.

3.2.2 Static nonlocal attenuation factor (α_s)

From Eq. (3.19), it can be seen that the nonlocal attenuation factor could be obtained by inverting the formulation for α_s. Here, we propose a semi-analytical approach to evaluate the parameters necessary to calculate α_s.

3.2.2.1 Enforced Gaussian displacement

Eq. (3.19) can be simplified by enforcing localized strains at points ξ_i and by not applying strain at the point x. In terms of the static stress distribution, we obtain:

$$\tau_{xx}^s(x) = (2\mu + \lambda) \int_x \alpha_s \; {e'_{xx}}^s(\xi) \; d\xi \tag{3.25}$$

The application of a localized strain at a single point will reduce the integral in Eq. (3.25) to a single term, and thus simplify the α_s calculation by using a numerically evaluated stress distribution.

A static analysis is setup by applying a prescribed localized displacement of the form of a Gaussian function in the y-direction at a single point ξ as shown in Fig. 3.4. Ideally, a displacement following a Dirac-delta distribution in space would be required. However, for practical simulations, the abrupt change in the Dirac-delta distribution based displacement generates residual strains in addition to the local strain. The gradually varying tailed displacement profile of the Gaussian distribution (Fig. 3.4) in space generates minimal residual strains. This procedure is repeated for coordinates ξ_i which are dx' distance apart and spanning the entire length of the plate, i.e $\xi_i \in \left[-\dfrac{a}{2}, \dfrac{a}{2} \right]$.

Localization of the displacement is necessary to calculate the α_s from Eq. (3.25) as it is difficult to numerically separate the local ($e_{xx}^s(x)$) and nonlocal (${e'_{xx}}^s(\xi)$) strain
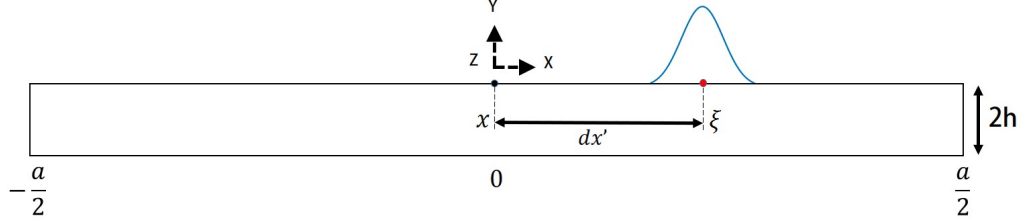
Fig. 3.4.: Schematic illustrating the enforced Gaussian displacement profile applied on a flat plate at a point ξ which is dx' distance away from the local point x. The total stress is measured at x (center of the unit cell).

components for the calculation. In the nonlocal stress-strain relation (Eq. (3.25)), the enforced Gaussian displacement at ξ contributes only to the nonlocal strain component $(e'_{xx}{}^{s}(\xi))$ at the point of measurement of stress, x. For a given study, as localized displacement is enforced only at ξ, the local strain at the measurement point x is zero and hence, only the nonlocal strain contributes to the total stress at the center of the unit cell (x).

3.2.2.2 Semi-analytical procedure for the calculation of α_s

The static nonlocal attenuation factor (α_s) is calculated from the constitutive relation in Eq. (3.25). In order to calculate α_s, it is necessary to evaluate the values of all other variable parameters defined in Eq. (3.25). Hence, this section focuses on developing a numerical procedure to evaluate all these parameters and to calculate the α_s from the analytical formulation (Eq. (3.25)) as follows:

1. A finite element (FE) model of the metastructure is used to simulate the static response of the structure.

2. The Gaussian displacement, elaborated in the previous section, is enforced at point ξ of the numerical model (Fig. 3.4). The Gaussian displacement profile (shown in Fig. 3.4) has a maximum amplitude at x, while the tails reduce the value to zero (approximately) on either sides of point ξ.

3. Once the enforced displacement is setup, the metastructure geometry is meshed. The regions close to ξ are meshed with quadrilateral (quad) mesh elements for accurate results, while the regions near the tails of the enforced Gaussian displacement are meshed with triangular (tri) mesh elements as depicted in Fig. 3.5. The rest of the geometry is mapped with the distribution functions available in the numerical software and is meshed with rectangular elements.
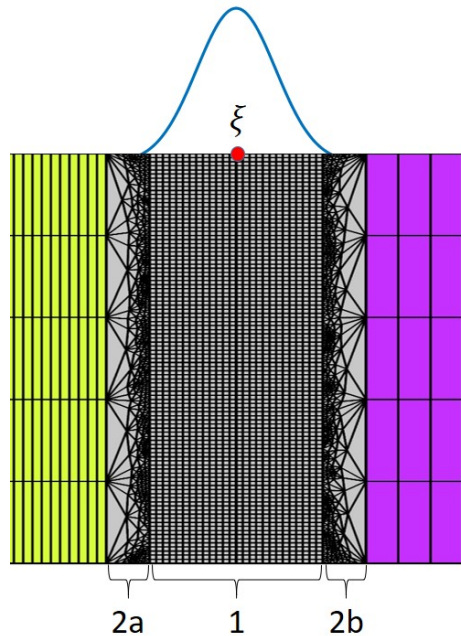
Fig. 3.5.: Schematic showing the meshing pattern in the proximity of enforced Gaussian displacement. Region 1 is meshed with quadrilateral elements, while regions 2a, and 2b are meshed with triangular elements.

4. The numerical design with the enforced displacement is subjected to a static analysis in a FE based software COMSOL.

5. The total static stress (τ_{xx}^s) at x and the time independent nonlocal strain $(e'_{xx}{}^s)$ value at ξ are measured from the data gathered by post processing the completed numerical simulation. Further, Lame's constants (μ and λ) are calculated from the material properties (E and ν) used for simulating the design. After enumerating all the parameters from the FE simulation for a single Gaussian

displacement enforced at ξ, the α_s is calculated by reorganizing the analytical relation in Eq. (3.25) as shown below:

$$\alpha_s = \frac{\tau_{xx}^s(x)}{(2\mu + \lambda) \, e'_{xx}{}^s(\xi)} \tag{3.26}$$

6. The procedure from 1-5 extracts single α_s value for a specific Gaussian displacement profile enforced at ξ which is at dx' distance from x. Similarly, the static numerical simulations are carried out for the enforced Gaussian displacements which are at $i \cdot dx'$, where i=0,1,2..., distances from x. A parametric sweep in i is setup in the FE software to obtain the α_s values for all the Gaussian displacements enforced along the length of the metastructure. On post processing, we gather i values of α_s corresponding to the i Gaussian displacements enforced. An α_s plot for the i points will generate a geometric distance dependent *nonlocal attenuation function.*

7. The static nolocal attenuation function of individual geometries are calculated and plotted by repeating the procedure from 1 to 6 for all the numerical designs developed in this work. Next chapter discusses the results and observations obtained by implementing this procedure.

3.2.3 Dynamic nonlocal attenuation factor (α_d)

In this section, we focus on the development of a procedure to obtain the dynamic nonlocal attenuation factor (α_d). Further, the later part of the section develops a procedure to solve the Rayleigh-Lamb dispersion equation in order to evaluate the dynamic behavior of the metastructure using α_d. The procedure is subdivided into two main sections:

3.2.3.1 Numerical procedure for the calculation of α_d

As per Eq. (3.21), we know that α_d is explicitly expressed as a function of distance dependent α_s and time dependent displacement u of the structure. As the detailed procedure to extract α_s was elaborated in section 3.2.2, this section focuses only on the development of a numerical procedure to obtain the structural displacement. Nowinski [116] discussed the use of the frequency dependent α_d based material properties (Eq. (3.23)-(3.24)) to evaluate the dispersion behavior of the structure, hence a numerical procedure is established to directly evaluate the displacement in the frequency domain and to calculate $\alpha_d(x, \omega)$ as follows:

1. A FE model of the metastructure is used to simulate the dynamic response of the structure.

2. The numerical design consists of 20 unit cells of the metastructure concatenated on either sides of the parent unit cell as shown in Fig. 3.6. The periodic ensemble is designed to capture the complete wave attenuation near band gap frequencies of the structure. As an added advantage, long wavelengths will be accurately captured by this periodic design.
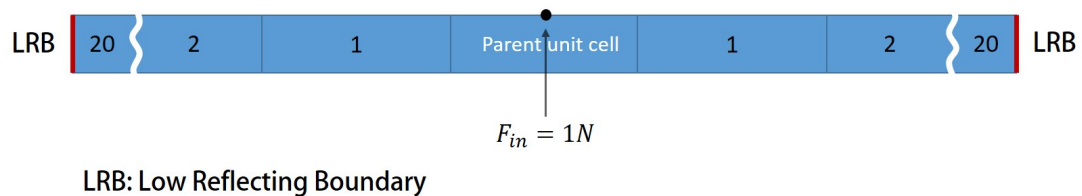
Fig. 3.6.: Schematic illustrates the ensemble designed for forced frequency analysis to understand the dynamic behavior of a given structure. Design in figure depicts a generalized framework for all the structures.

3. The ensemble is subjected to an external harmonic force of 1N magnitude (Fig. 3.6) at the center of the design. Low reflective layers are appended on the boundaries of the structure as shown in Fig. 3.6 to prevent any anomaly in

the resultant frequency based displacement amplitudes of the structure due to the flexural wave reflection from the boundaries.

4. Further, the periodic structure is meshed with free quad elements. After meshing, the structure enforced with the above prescribed force and the boundary conditions is subjected to a steady state forced frequency analysis in a FE software COMSOL. A specific metastructure design is simulated over a range of frequencies.

5. The procedure from 1 to 4 is repeated for all the geometries developed in this thesis.

6. After post-processing, the frequency dependent displacement profile of a specific design is physically subtracted from the displacement profile of its corresponding load-bearing baseline structure (flat and tapered plate) to separate-out the effective structural response due to the presence of the geometric nonlocality. As the local baseline structures lack nonlocal geometric connections, their effective displacement profiles equate to zero.

7. For each structure, the effective displacement profile is normalized by the peak displacement amplitude at the specific frequency. Further, the distance dependent α_s is physically multiplied to the above mentioned frequency based effective displacement profile to produce a spatial and frequency dependent α_d (Eq. (3.21)).

3.2.3.2 Semi-analytical procedure for solving the dispersion equation

From section 3.1.2, we know that the complete dynamic behavior of the metastructure is obtained by solving the Rayleigh-Lamb dispersion relation (Eq. (3.15)-(3.16)) using the effective nonlocal material properties [116]. As the effective material properties of the geometrically nonlocal metastructure depends on the α_d of the specific

structure calculated from the above section, the following procedure is developed to solve the dispersion relation:

1. From Eq. (3.24), we know that the material properties of the geometric nonlocal designs will vary as a function of $k-\omega$ dependent α_d. Hence, the $x-\omega$ dependent α_d calculated in the previous section is numerically fast Fourier transformed into the $k - \omega$ domain.

2. The numerical simulation procedure elaborated in the above section to calculate α_d measures the structural displacement u in the $x - \omega$ domain. As per Nowinski [116], the displacement in the $k - \omega$ domain is used to solve the Rayleigh-Lamb equations and, thus the $u(x,\omega)$ obtained in the above section is fast Fourier transformed into $U(k,\omega)$, where U is the displacement in the transformed domain.
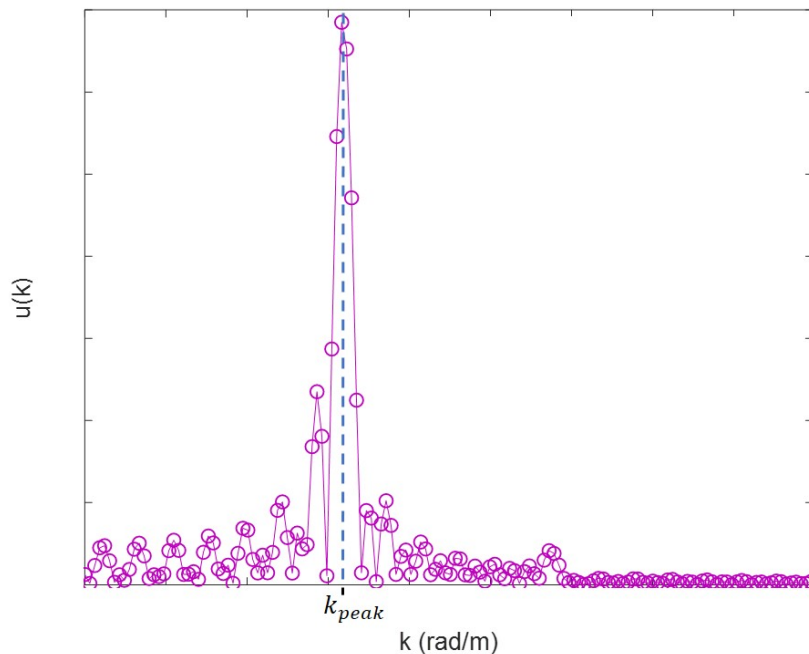
Fig. 3.7.: Plot shows the wavenumber (k_{peak}) corresponding to the peak value of $U(k)$=FFT$[u(x)]$ at a specific frequency ω_0 for a sample structure.

For a given structural response at a specific frequency (ω_0), we obtain a $U(k)-k$ plot as shown for a sample structure in Fig. 3.7. For each ω_0, the $U(k)$ plot (Fig. 3.7) peaks at a specific wavenumber k_{peak}, and the α_d corresponding to this k_{peak} and ω_0 combination is evaluated as the $\alpha_d(k, \omega_0)$. This procedure is repeated for range of frequencies to obtain all the $\alpha_d(k, \omega)$ values for the numerical design.

3. Once the effective nonlocal material properties of the structure are calculated using the $\alpha_d(k, \omega)$ values, the work further focuses on solving the Rayleigh-Lamb's antisymmetric mode equation (Eq. (3.16)). An unconstrained minimization technique with user defined gradient is numerically implemented to solve this nonlinear Rayleigh Lamb equation. Detailed explanation about the minimization technique used and the results obtained are in the next chapter.

4. The procedure described above is repeated for all the geometries developed in the thesis.

The next chapter evaluates the dynamic performance of all the designs based on the results obtained by implementing the above mentioned semi-analytical approach, and numerical simulation procedures.

4. DESIGN AND NUMERICAL VALIDATION OF NONLOCAL ABH METASTRUCTURES

The previous chapters presented the necessary theoretical tools to study the performance of nonlocal ABH metastructures. This chapter focuses on the design of nonlocal ABH metastructures and on understanding their characteristics. The first part of this chapter introduces the general idea of a 2D nonlocal ABH metastructure and its design principles. The reminder of the chapter is dedicated to presenting the numerical results obtained and analyzing the performance. Particular attention will be given to the characterization of the dynamic performance in the ultra-low frequency regime and to the evaluation of the cut-on frequency of the ABH metastructures.

4.1 Nonlocal ABH Metastructure: Basic Concepts And Designs

This section explores the possible designs of ABH metastructures, intentionally conceived to provide a highly nonlocal dynamic response of the entire assembly. In the following section, we identify a few possible design configurations that will be used as the benchmark to characterize the performance of the nonlocal metastructure. Specifically, we intend to analyze the effect of the intentional nonlocal design on the cut-on frequency of the ABH metastructure and on its broadband vibration attenuation behavior.

4.1.1 Engineering the nonlocality in ABH metastructures

Although different design strategies can be conceived in order to achieve nonlocal properties, in this study we chose to use an artificial add-on structure consisting of a set of highly rigid beam connectors and a flexible thin plate. The artificial structure

is connected to the supporting load bearing ABH structure whose dynamic properties are sought to be controlled. The role of the different components is explained in the following sections.

4.1.1.1 Rigid beam connectors

Among the various combinations of rigid beam connector design parameters including the quantity and the locations that can be conceived, we selected a configuration with five connectors as shown in Fig. 4.1 and Fig. 4.4 (middle, bottom). This configuration is the result of a parametric study conducted to achieve long range force interactions without significant increase in the stiffness of the system. The chosen number of rigid connections maintain the flexibility without compromising the nonlocal effect (a higher number of connectors will increase the stiffness, hence diminishing the effect of the strain at a distance), while their position at the center of the tapers create energy paths through structural locations characterized by high energy density (i.e the ABH centers).

4.1.1.2 Non-load bearing (NLB) layer

The artificial layer connected to the ABH metastructure is not load bearing and can be either a flat plate or an ABH plate. Although both the designs will produce a nonlocal effect, it is expected that the NLB layers integrating ABH embedded layers could offer better energy control in the low frequency regime.
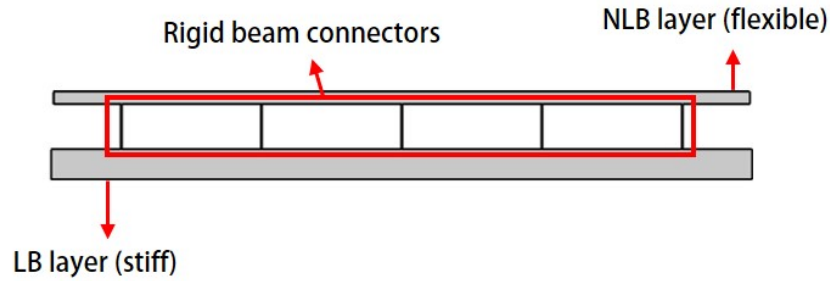
Fig. 4.1.: Schematic classifying the three components of the nonlocal system design with flat base plate: (i) rigid beam connectors; 5 thin beams provide the long range connections, (ii) NLB layer; flexible and non-load bearing plate for vibration control, and (iii) LB layer; stiff and load bearing component.

4.1.1.3 Load bearing layer

In order to have a reference configuration for a clear assessment of the performance, we developed two baseline structures without using the nonlocal geometric design. These baseline structures simply consist of the load bearing layer as shown in Fig 4.2-4.3. We will refer to these configurations as the *baseline structures*. The two baseline designs are:

1. Flat plate:
   A thin rectangular flat plate with $\dfrac{l}{t} \gg 1$ is chosen as the first type of local baseline structure, as shown in Fig 4.2.
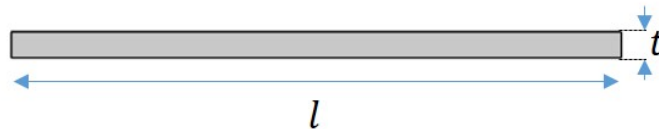
Fig. 4.2.: Schematic of a thin flat plate baseline structure.

2. Tapered plate:
   An embedded lattice of periodic tapers with a maximum thickness t, length l

and the same material properties of flat plate (refer Table 4.1) is the second baseline design (Fig 4.2).
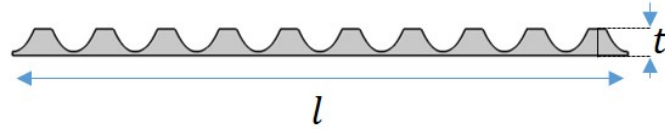
Fig. 4.3.: Schematic of a tapered plate baseline structure (embedded with 10 ABHs).

The static and dynamic response of both the baseline structures will be the reference for comparing the performances of the nonlocal designs.

4.1.2 Nonlocal ABH metastructure design

Design Nomenclature	CAD model
Flat plate	
Top Flat Bottom Flat (TFBF)	
Top Tapered Bottom Flat (TTBF)	

Fig. 4.4.: Schematics of the different types of designs employing a flat plate baseline structure. Flat plate (top) is the local baseline design while TFBF (middle) and TTBF (bottom) are its nonlocal models.

Design Nomenclature	CAD model
Tapered plate	
Top Flat Bottom Tapered (TFBT)	
Top Tapered Bottom Tapered (TTBT)	
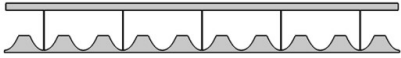
Fig. 4.5.: Schematics of the different types of designs employing a tapered plate baseline structure. Tapered plate (top) is local baseline design while TFBT (middle) and TTBT (bottom) are its nonlocal models.

From the previous section, we know that a nonlocal design is modeled by integrating a NLB layer (i.e flat or ABH plate) on to a LB layer (i.e flat or tapered plate). In total, we will analyze four nonlocal and two baseline structures as shown in Fig. 4.4 and Fig. 4.5. We classify these structures into two different groups based on their baseline geometry:

1. **Flat plate**

    A flat plate baseline design is shown in Fig. 4.4 (top). This reference configuration does not exhibit nonlocal effects. The flat plate based nonlocal designs are:

    (a) Top Flat Bottom Flat (TFBF): The flat plate baseline structure is connected to a thin flat plate on top using a series of rigid beam connectors as shown in Fig. 4.4 (middle).

(b) Top Tapered Bottom Flat (TTBF): The flat plate baseline structure is connected to a thin ABH plate on top using a series of rigid beam connectors as shown in Fig. 4.4 (bottom).

2. **Tapered plate**

The flat plate with ten embedded ABHs as shown in Fig. 4.5 (top) is referred to as the tapered plate baseline structure. This reference configuration does not exhibit nonlocal effects. The nonlocal designs based on the tapered plate are:

(a) Top Flat Bottom Tapered (TFBT): The tapered plate baseline structure is connected to a thin flat plate on top using a series of rigid beam connectors as shown in Fig. 4.5 (middle).

(b) Top Tapered Bottom Flat (TTBT): The tapered plate baseline structure is connected to a thin ABH plate on top using a series of rigid beam connectors as shown in Fig. 4.5 (bottom).

The properties and the dimensions of the baseline structures and their corresponding nonlocal designs used in the thesis are described in the next section.

4.1.3   Geometric details of the nonlocal designs

The baseline structures have a periodic unit cell length l of 1.4m. The tapered plate baseline design has an embedded lattice of periodic ABHs repeated every 0.14m with minimum thickness of 1.5mm and maximum thickness of 8mm. To maintain structural integrity, the tapered plate baseline structure is embedded with ten small sized tapers in place of a single big taper. A single taper along the plate length with high $\dfrac{l}{t}$ will produce regions of small stiffness and low strength on the structure, while more than ten ABHs along the unit cell length will be difficult to manufacture and will generate a flexible layer with reduced load bearing property.

Table 4.1.: Material properties of LB layer, NLB layer and rigid beam connectors used for all the geometries.

Geometry	Density (kg/m^3)	Young's Modulus (GPa)	Poisson's ratio
LB layer	2700	79	0.33
NLB layer	1000	2	0.35
Connectors	10	1000	0.27

Table 4.2.: Dimensions of LB layer, NLB layer and rigid beam connectors used for modeling the baseline structures and their nonlocal designs.

Plate	Properties	Flat plate	TFBF	TTBF	Tapered plate	TFBT	TTBT
LB layer	Width (m)	1.4	1.4	1.4	1.4	1.4	1.4
	Max Height (m)	0.008	0.008	0.008	0.008	0.008	0.008
	Min Height (m)	0.008	0.008	0.008	0.0015	0.0015	0.0015
	No. of Tapers	0	0	0	10	10	10
	Taper power-m	-	-	-	2.2	2.2	2.2
NLB layer	Width (m)	-	1.39	1.39	-	1.39	1.39
	Max Height (m)	-	0.0033	0.008	-	0.0033	0.008
	Min Height (m)	-	0.0033	0.0012	-	0.0033	0.0012
	No. of Tapers	-	0	0	-	1	1
Connectors	Width (m)	-	0.002	0.002	-	0.002	0.002
	Height (m)	-	0.012	0.012	-	0.0189	0.0189

These baseline structures are connected with a thin NLB flat or ABH plate of length moderately shorter than the baseline layer (refer Table 4.2 for exact dimensions). Both types of NLB layers have the same total surface areas to accurately

compare the introduced nonlocal effect. A large single taper is used for the NLB ABH plate in the nonlocal assembly as major part of the strength and support is provided by the baseline structure. It also reduces the complexity of the design.

The properties and the exact dimensions of the local and nonlocal geometries introduced in the previous section are enumerated in Table 4.1 and Table 4.2 respectively. The dimensions and the properties listed in Table 4.1 and Table. 4.2 are not optimized. All models are 2D plane strain thin structures with dominant bending stress at low frequencies. The performance of all the models are numerically investigated with a FEM based software in the next section. Models are built and solved in COMSOL Multiphysics, while the data post processing is carried out in MATLAB.

4.2   Evaluation of the Nonlocal Dynamic Response

Series of numerical simulations are performed to understand the effect of nonlocality on the dynamic response of the above defined structures. Numerical evaluation of dispersion curves and transfer functions are used to explore the performance of the proposed nonlocal designs. The dispersion results obtained using an eigenfrequency based analysis are discussed in the first part of this section. The semi-analytical approach developed in the previous chapter to extract the nonlocal attenuation factors is implemented in this section to capture the fundamental dispersion modes. The last part of this section discusses the steady state response of the nonlocal structures.

4.2.1   Dispersion analysis

The analysis of the dispersion band structure is performed by solving an eigenvalue problem for both the local and the nonlocal designs. From a numerical standpoint, the dispersion equations are evaluated by solving an eigenvalue problem based on the homogeneous form of Navier's equation (covered extensively in section 2.4.1). Here, the frequency and the wavenumber based dispersion relation characterize the modal behavior of the structure.

The structural unit cells are designed as per the properties and dimensions mentioned in Table 4.1-4.2. Floquet boundary conditions are enforced on either edges of a unit cell of length l to simulate an infinite periodic structure. Using Brillouin's theory [78], wavenumber k_x is parametrically swept in the $[0, \text{pi}/l]$ range. Once setup, the unit cell is meshed with quad elements and solved numerically. Converged numerical eigen-frequency study provides the frequency and the corresponding wavenumber based dispersion curve for the structure. This procedure is repeated to capture dispersion curves for all local and nonlocal structures.

As mentioned in the previous section, the effective dynamic properties obtained from the dispersion of the nonlocal designs are compared to their baseline configurations. Before exploring the dynamic performance of the nonlocal designs, we analyze and compare the baseline configurations based on their dispersion characteristics in the next section.

4.2.1.1 Comparison of the baseline structures
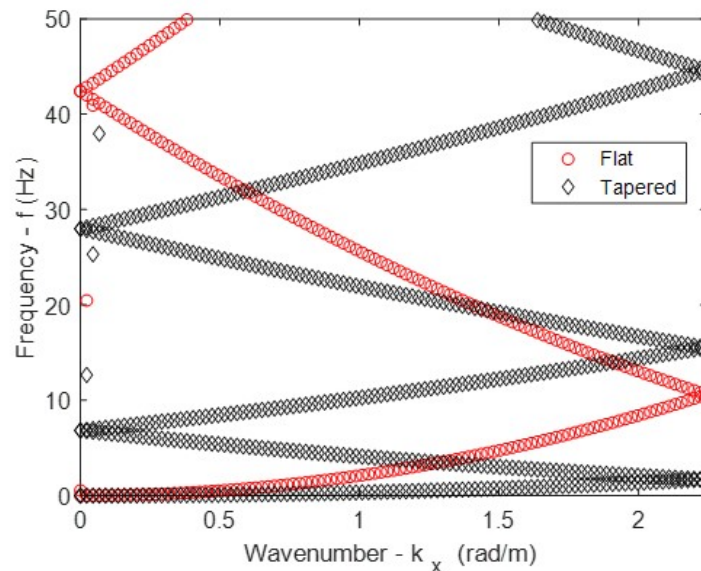
Fig. 4.6.: Dispersion curves of flat and tapered plates.

The dispersion bands of both the flat and the tapered baseline plates are shown in Fig. 4.6. From the direct comparison of the dispersion bands in the low frequency range, we observe steeper slopes for the flat plate dispersion bands compared to the same bands of the tapered plate. This result indicates that the flexural waves travel faster in the flat plate in comparison to its tapered counterpart. The lower elastic wave velocity in tapered plates can be attributed to the lower bending stiffness of the ABH metastructure. The low thickness regions generated by the taper profiles reduce the local stiffness of the tapered plate in comparison to the flat plate of the same length, and constant thickness and as a consequence the dispersion bands of the tapered plate have a visible downward frequency shift (Fig. 4.6) with respect to the flat plate.

4.2.1.2   Comparison of flat plate, TFBF, and TTBF

The following observations can be made about the dynamic behavior of the non-local designs TFBF, and TTBF when compared to their corresponding flat plate baseline structure:

1. As illustrated by Nowinski [116] in a general study of the dynamic behavior of thin plates with and without nonlocal material properties, the dispersion bands of plates with nonlocal properties tend to shift to lower frequencies. On the contrary, in the nonlocal designs developed in this thesis we do not observe a significant downward shift in the frequency bands of TFBF and TTBF with respect to flat plate, as shown in Fig. 4.7. This is attributed to the characteristic feature of the proposed nonlocal geometries in which the addition of a NLB layer enhances the stiffness of the nonlocal structure. On one hand, the introduction of the nonlocal behavior lowers the band structure as illustrated by Nowinski [116], while on the other, the higher stiffness of the structure due the introduced NLB layer pushes the bands to higher frequency range. Thus, as the stiffening effect of TFBF and TTBF superimposes the nonlocal effect, the band structure
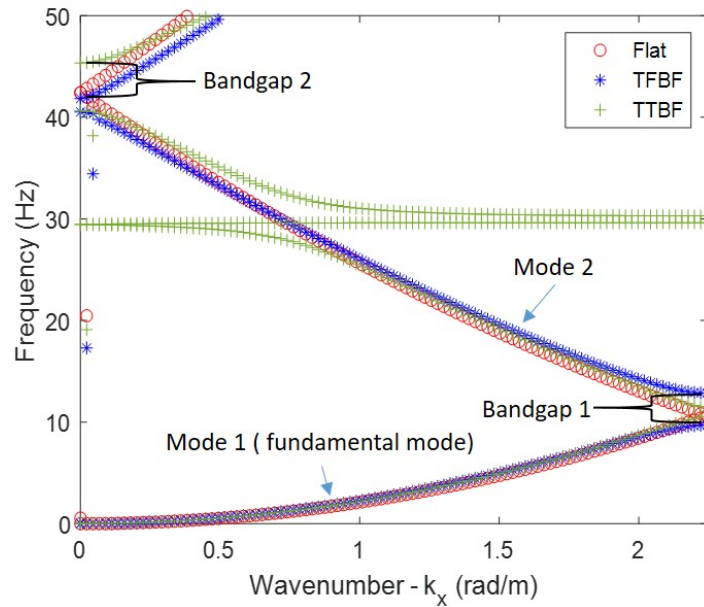
Fig. 4.7.: Plot comparing the dispersion curves of flat plate, TFBF, and TTBF.

seems to have a slight upward shift compared to the flat plate. This up-shift with respect to the bands of the flat plate is not prominent in Fig. 4.7 as the majority of the stiffness contribution is from the flat LB layers of TFBF and TTBF.

2. Fig. 4.7 only shows the real wavenumbers that represent the propagating waves (Fig. 4.8a-b), while the frequencies with purely imaginary wavenumber solutions are associated with the evanescent waves (Fig. 4.9b) and correspond to the bandgaps (Fig. 4.9a). The first two band gaps in the long wavelength (low frequency) regime, bandgap 1 and bandgap 2, in Fig. 4.7 are characterized by the destructive interference of the scattered waves caused by the introduction of flexible NLB layer in conjunction with the periodicity of the structure. All structures, irrespective of the type of NLB layer connections involved, have similar dynamic behavior in the long wavelength regime. Hence, the bandgap 1 (Fig. 4.7 and Fig. 4.9a) generated around a central frequency of 10 Hz by both TFBF and TTBF is due to the periodicity of the nonlocal structures and
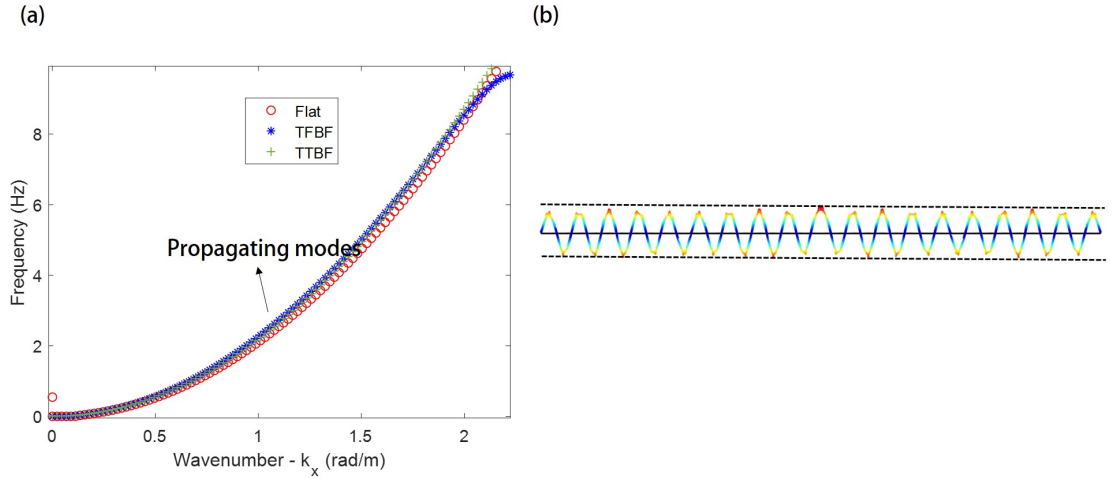
Fig. 4.8.: (a) The dispersion of the fundamental mode for different configurations with flat LB layer, and (b) the eigen displacement on a periodic TTBF structure at a frequency f=9 Hz which is within the propagating range.
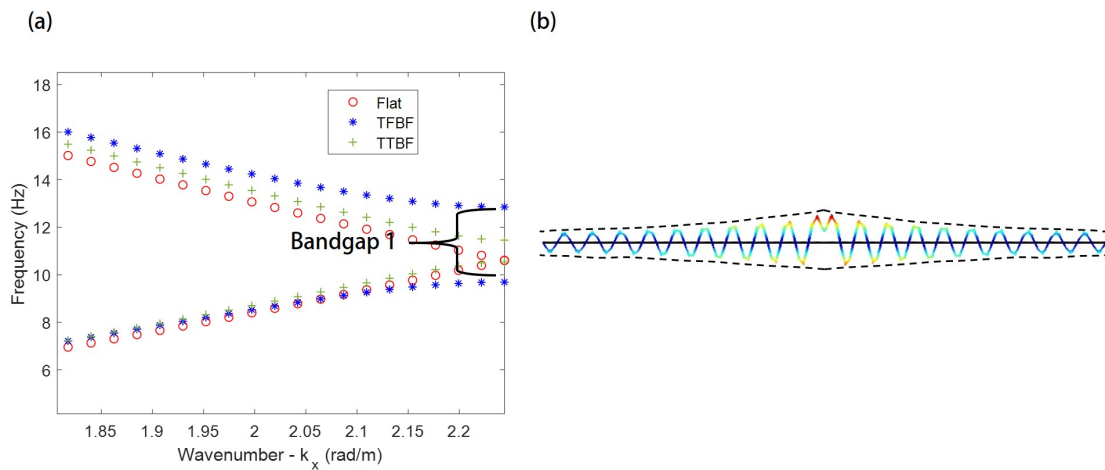
Fig. 4.9.: (a) Bandgap between first and second modes in dispersion of different configurations with flat LB layer (b) eigen displacement of an evanescent wave pattern on a periodic TTBF structure at a frequency f=10.55 Hz which is within the first band gap.

it is independent of the nonlocal geometry. This is also evident in the mode shape obtained from a frequency in bandgap 1 (Fig. 4.10a). Starting from the second band this behavior begins to diverge. The NLB layer has a significant

contribution to the dynamic behavior of the structure in bandgap 2 (Fig. 4.7), as observed in the mode shape in Fig. 4.10b
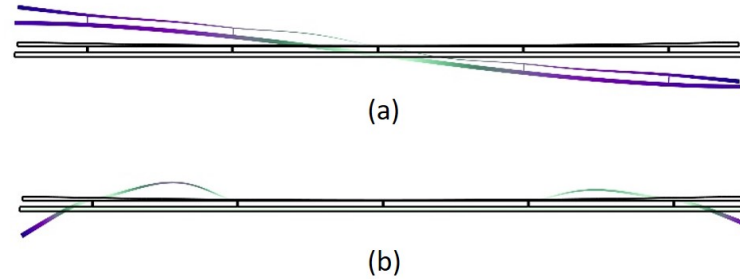
Fig. 4.10.: Mode shapes obtained by the eigenvalue analysis of TTBF: (a) at frequency $f=$ 10.546 Hz in bandgap 1, and (b) at frequency $f=$ 54.162 Hz in bandgap 2.

3. The local resonance of the NLB layer, in the nonlocal design, results in the formation of standing waves as shown in Fig. 4.11a. Fig. 4.11b shows the eigenstate corresponding to a frequency in the flat band which confirms the standing wave pattern.
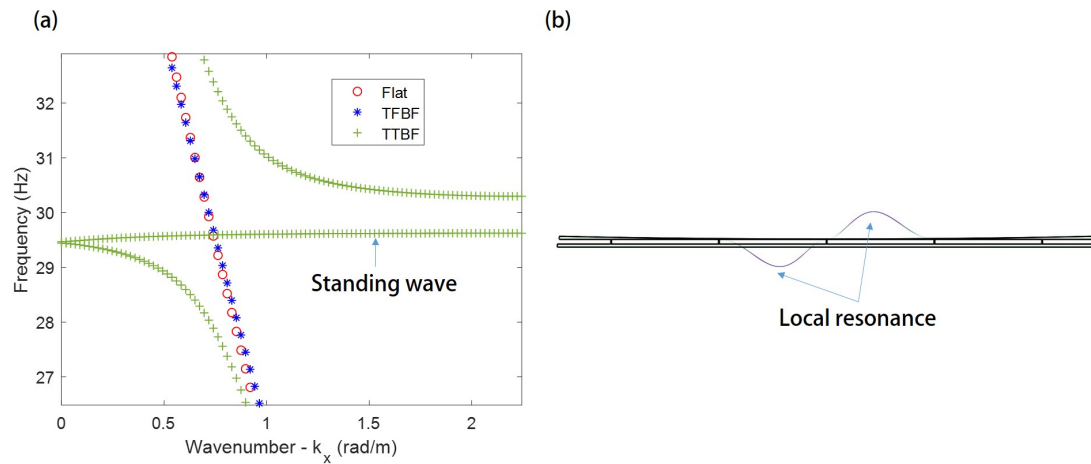
Fig. 4.11.: (a) Flat band corresponding to a standing wave localized on the NLB layer, and (b) the corresponding eigenstate for the TTBF structure at resonant frequency $f =$ 29.623 Hz.

4. Fig. 4.12 highlights that the TTBF configuration, which uses ABH plate as the NLB layer, visibly enhances the bandwidth in bandgap 2 compared to the TFBF (refer to Fig. 4.7). As previously indicated, this effect can be attributed to the higher energy attenuation property of ABHs due to their taper profiles.
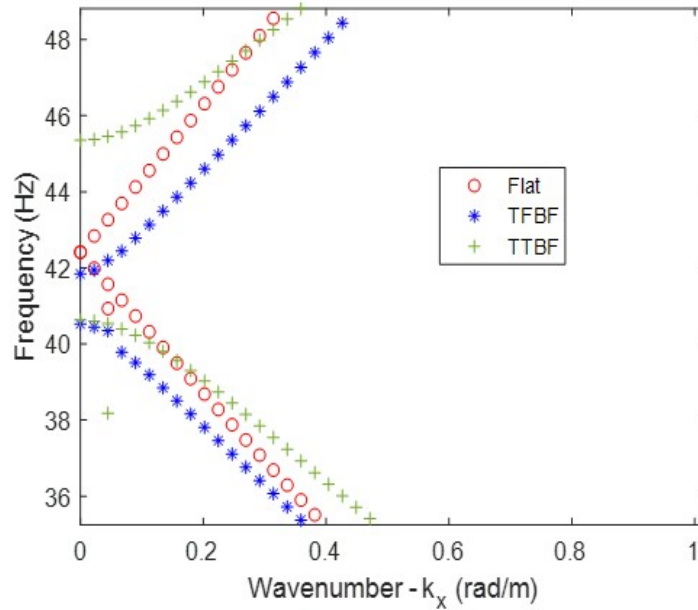
Fig. 4.12.: Zoomed in view from Fig. 4.7, showing the details of bandgap 2 for both the TFBF and the TTBF configurations.

Similar observations can be made on comparing the nonlocal structures with a common tapered baseline plate. This will be elaborated in the section below.

4.2.1.3   Comparison of tapered plate, TFBT, and TTBT

The direct comparison of the dispersion curves of the nonlocal designs with the corresponding baseline designs exhibit some similarities regardless of the type of the LB layer and the NLB layer involved. Hence, this section will only focus on the characteristic differences generated in the dispersion by using a LB layer of the form

of a tapered plate. The following remarks can be made about the dynamic behavior of the nonlocal designs with tapered LB layer from Fig. 4.13:
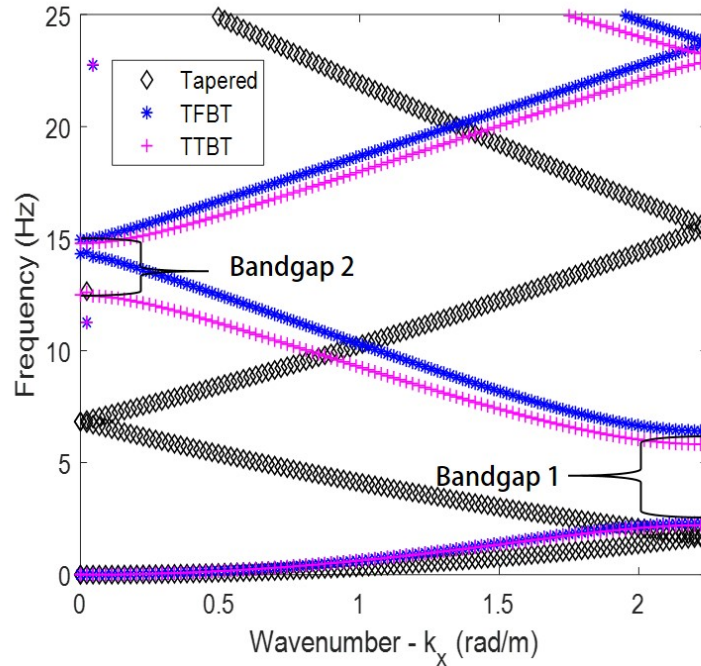
Fig. 4.13.: Plot comparing the dispersion curves of tapered plate, TFBT, and TTBT.

1. Similar to the observation made about the nonlocal structures with flat LB layer, dispersion bands of the nonlocal structures with tapered LB layer (TFBT and TTBT) shows an upward shift in Fig. 4.13 due to their higher stiffness compared to the tapered plate baseline structure. Further, on comparing Fig. 4.7 and Fig. 4.13, it is noted that the upward shift in the dispersion bands of the nonlocal structures with the tapered LB layer is higher than the dispersion shift of the nonlocal flat LB layer structures. This is attributed to the lower stiffness of the tapered LB layer. Nonlocal structures with low stiffness tapered LB layer have higher stiffness contribution from the added NLB layer, but the stiffness contribution from the NLB layer of the nonlocal designs with stiff flat LB layer is meager.

2. As elaborated before, regardless of the type of the NLB layer connected, periodicity in the nonlocal structures (TFBT and TTBT) is responsible for bandgap 1 (Fig. 4.13) in the low frequency regime. The NLB layer tends to have an effect on the dynamic behavior of the nonlocal structure starting from second band and, thus contributes significantly to the formation of bandgap 2 (Fig. 4.13).

3. Due to the inability of the taper in the NLB ABH layer to capture at least a complete wavelength at the low frequency range (2.3-6.4 Hz) of the bandgap 1 in Fig. 4.13, we observe a rather smaller bandgap in the TTBT (even with NLB ABH layer) compared to the TFBT (with NLB flat layer). Further, as the wavelength reduces (higher frequencies) and at least one complete wavelength is captured by the taper in the NLB ABH layer of the TTBT at frequencies corresponding to the bandgap 2 (Fig. 4.13), the ABH effect attenuates the wave energy and enhances the bandgap width.

4.2.2 Effective nonlocal material properties: semi-analytical approach

The procedure for extracting the dynamic material properties of the nonlocal structure was described in chapter 3. The nonlocal elasticity formulation was modified to capture the nonlocal material properties as a function of the geometric attenuation factor. Here, we evaluate the attenuation factor for all the models proposed above. The attenuation factor for each design can be calculated in two parts, namely, the static and the dynamic attenuation factor. Finally, the attenuation factor based nonlocal material properties will be used to asses the the dispersion behavior of the nonlocal designs.

4.2.2.1 Static nonlocal attenuation factor (α_s)

The procedure introduced in section 3.2.2 to evaluate the effective nonlocal properties is implemented here to specifically find the static nonlocal attenuation factor (α_s).

A Gaussian displacement (refer to section 3.2.2.1) is enforced at every dx'=12.6mm, starting from the total stress measurement point (originally at the center of the unit cell) as shown in Fig. 4.14. For each dx'=12.6mm, the total static stress (τ_{xx}^s) measured at the center of the unit cell, and the time independent nonlocal strain $({e'_{xx}}^s)$ measured at the displacement enforced position are used to calculate the α_s as in Eq. (3.26). All the parameters necessary to evaluate α_s are measured from the static numerical simulation results, as elaborated in section 3.2.2.

The α_s evaluated for all the proposed designs are plotted as a function of the spatial
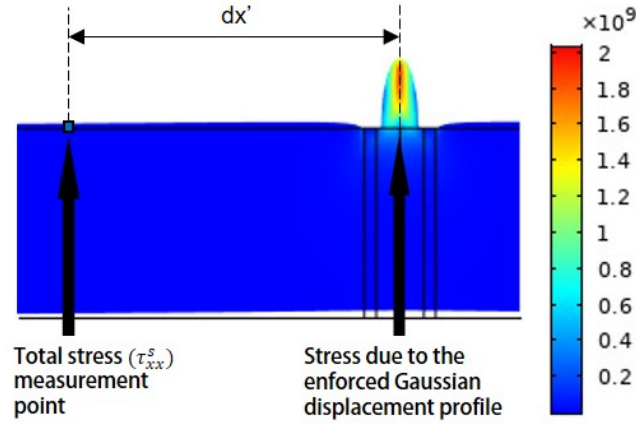
Fig. 4.14.: Stress plot on a flat plate due to the enforced Gaussian displacement (obtained from static FE simulation). The enforced Gaussian displacement generated strain $({e'_{xx}}^s)$ at dx' distance is the only strain contribution to the total stress (τ_{xx}^s) measurement point.

position of the enforced displacement in Fig. 4.15 and 4.16. Further, the following observations can be deduced from the results obtained:

1. **General observations on the static nonlocal attenuation factor (α_s):**
   The plots shown in Fig. 4.15-4.16 represent the trend of the static nonlocal attenuation factor obtained from Eq. (3.26). The vertical axis corresponds to a normalized α_s, while the horizontal axis represents the spatial position of the enforced Gaussian displacement (extending on either sides from the center of the individual structure). When the point of application of the enforced

displacement is very close to the total stress measurement point (which is the center of the structure), α_s has the maximum value (shown by the peaks in Fig. 4.15 and 4.16) as the enforced displacement in close proximity generates near local strain profile on the stress measurement location on a continuum scale. This behavior is consistent with the response of the baseline structures, which are local in nature. As the point of application of the enforced displacement moves away from the center of the structure, there is a sharp drop in the α_s value of the baseline structures, while the factor drops gradually for the nonlocal designs. The α_s amplitudes of the nonlocal designs and the baseline structures are similar only at the boundaries of the unit cell of the structures, at positions where the nonlocality controlling NLB layers end.

2. **Effect of the NLB layer:**

   Analyzing the α_s plots of the nonlocal structures with the flat plate (Fig. 4.15) and the ABH plate NLB layers (Fig. 4.16), it is established that the introduction of a low density and flexible NLB layer increases the magnitude of the attenuation factor at distant points of the structure in both the cases. In the nonlocal structures with flat plate LB layer (TFBF and TTBF), a gradual reduction in α_s is observed between any two consecutive rigid beam connectors while a small but sudden dip in α_s is noticed at the end of every rigid beam connector. Observe the variation of α_s with the unit cell distance of the TFBF and the TTBF structures in Fig. 4.15 to visualize the above mentioned effect. Similar pattern is also observed in the TFBT and the TTBT (Fig. 4.16) structures. The rigid beam connectors act as a pathway to propagate flexural waves through the NLB layer to distant points on the baseline structure and, thus establishing the nonlocal effect.
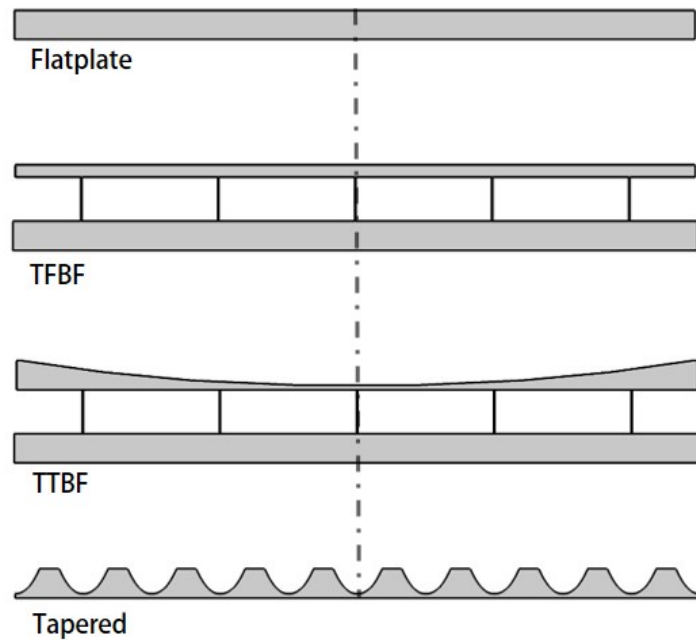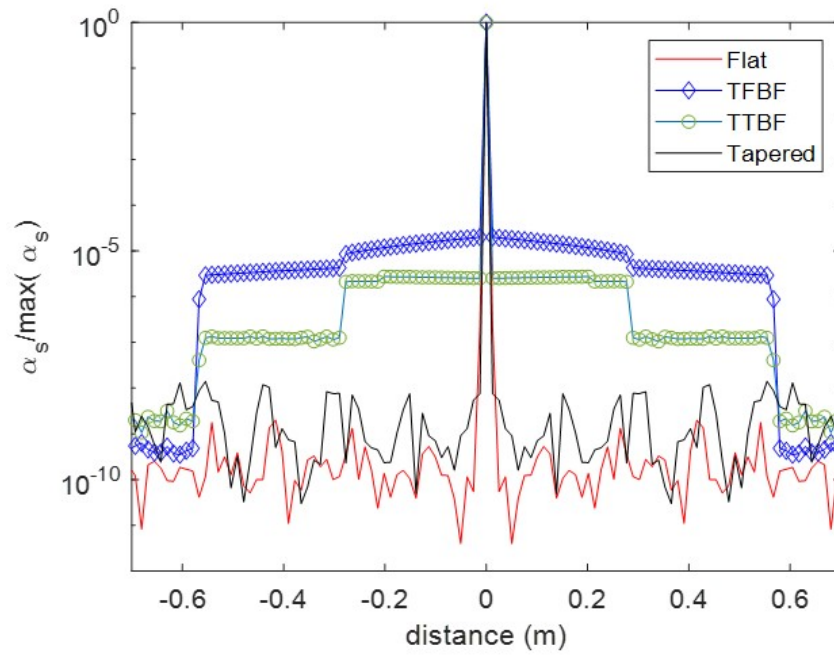
Fig. 4.15.: The static attenuation factors of flat plate, tapered plate, TFBF, and TTBF. The stress reading is always taken at the center of each structure while the enforced displacement is moved along the unit cell length on either side of the measurement point.
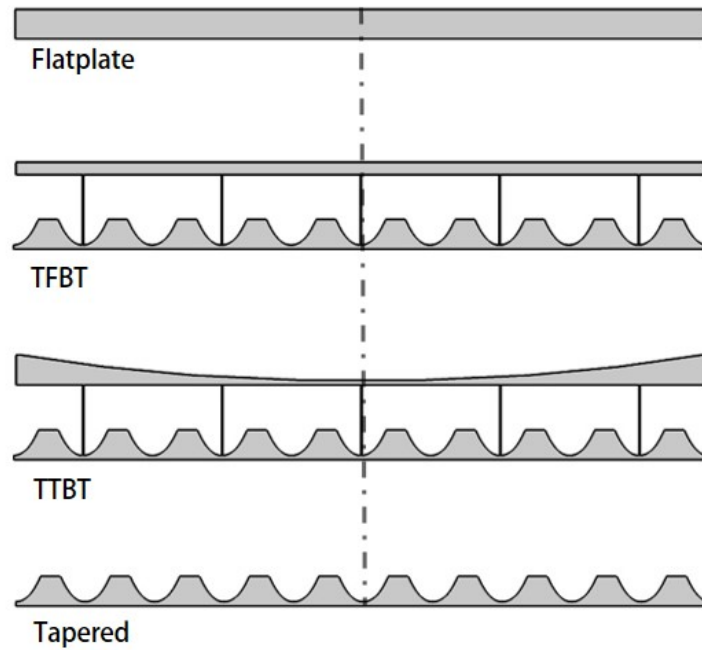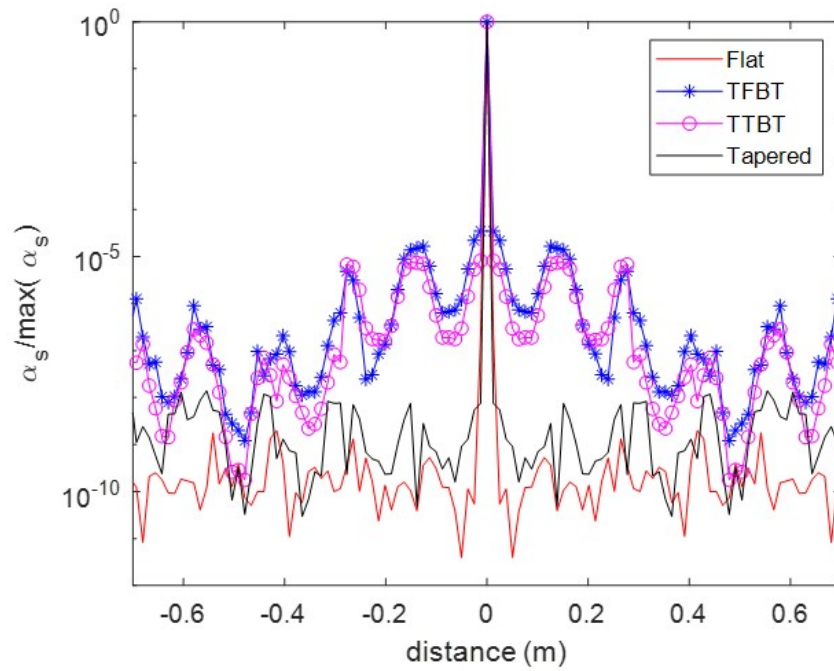
Fig. 4.16.: The static attenuation factors of flat plate, tapered plate, TFBT, and TTBT. The stress measurement is always taken at the center of each structure while the enforced displacement is moved along the length of the unit cell on either side of the measurement point.

3. **Effect of the ABH:**

   Due to the periodic nature of the ten tapers on the LB layer within the single unit cell, nonlocal structures with tapered plate LB layer has an oscillating attenuation factor decaying at a higher rate after the end of each rigid beam connector as shown in Fig. 4.16. Observe α_s of TTBT and TFBT varying with the position of the enforced displacement in Fig. 4.16.

   Further, as the ABH plate NLB layer is more flexible than the flat plate NLB layer, the amplitude of the normalized α_s for the TTBF and the TTBT nonlocal structures with tapered plate NLB layer is slightly lower in magnitude compared to the TFBF and the TFBT nonlocal structures with flat plate NLB layer as shown in Fig. 4.15 and Fig. 4.16.

4.2.2.2   Dynamic nonlocal attenuation factor (α_d)

The procedure elaborated in section 3.2.4 is implemented here to evaluate the dynamic nonlocal attenuation factor (α_d). From section 3.2.3, it is known that the nonlocal material properties are a function of the frequency-wavenumber dependent dynamic nonlocal attenuation factor ($\alpha_d(k,\omega)$). Unlike the frequency independent α_s, a frequency dependent α_d has to be calculated for the individual structure. In this section, a steady state frequency response analysis is numerically simulated to evaluate the frequency dependent displacement profile of each structure, which in conjunction with the α_s produces the α_d. Later, the nonlocal properties calculated with α_d using Eq. (3.23-3.24) are used to plot the fundamental modes of the dispersion curves by solving the Rayleigh-Lamb equation (Eq. (3.16)). Further, the numerically obtained dispersion curves of the structures evaluated in section 4.2.1 are matched with dispersion produced by solving the Rayleigh-Lamb equation for the antisymmetric modes. This will verify the dynamic performance characteristics evaluated from the semi-analytically calculated nonlocal attenuation factors.

1. **Calculating the dynamic nonlocal attenuation factor (α_d):**

   A steady state frequency response analysis (refer to section 2.4.2) is numerically simulated to calculate the displacement profile of each structure for range of frequencies in the fundamental dispersion bands. The simulated periodic ensemble has sufficient length to capture small wavenumbers ($k_x \geq 0.05^*\pi/l$), as elaborated in section 3.2.3.1.

   Further, the displacement profile of the baseline structure is subtracted from the displacement profile of the nonlocal structure with the corresponding LB layer to generate an effective displacement profile (u_{eff}) for each nonlocal system. These effective displacement profiles are normalized by the maximum amplitude of the displacement at that specific frequency for the given structure. Finally, a product of the normalized static nonlocal attenuation factor ($\overline{\alpha}_s$) and the normalized displacement profile ($\overline{u}_{eff}$) from the frequency response calculates a spatial and frequency dependent dynamic nonlocal attenuation factor (α_d), as formulated below:

   $$\alpha_d(x_i, \omega^j) = (\overline{u}_{eff}^j)_i \, \overline{\alpha}_{si} \tag{4.1}$$

   where $(\overline{u}_{eff}^j)_i = \dfrac{(u_{eff}^j)_i}{max(u_{eff}^j)}$, and $\overline{\alpha}_{si} = \dfrac{\alpha_{si}}{max(\alpha_{si})}$ are normalized effective displacement, and normalized static attenuation factor respectively for the jth frequency at the $i \cdot dx'$ position coordinate along the length of the structure. Further, the fast Fourier transform (FFT) of $\alpha_d(x_i, \omega^j)$ produces a wavenumber dependent dynamic function for the jth frequency of the given structure. The dominant wavenumber is chosen from the peak magnitude of the FFT of the nonlocal structure's displacement (u^j) profile, the obtained position is used to find a single $\alpha_d(k, \omega_j)$ for each frequency (refer to section 3.2.3.1).

2. **Numerical solution of the Rayleigh-Lamb equation:**

   The nonlocal material properties are evaluated with the $\alpha_d(k, \omega_j)$ calculated above. The theoretical Rayleigh-Lamb formulation (Eq. (3.16)) is solved with the α_d to plot the dispersion curves. The non-linearity of the transcendental

equation (Eq. (3.16)), and the existence of infinite number of solutions create serious challenges in calculating the numerical solution. In his work, Nowinski [116] used mathematical approximations of the transcendental equations to plot the dispersion curves. In this work, an accurate solution is obtained by using an optimizer. An unconstrained minimization technique for non-linear problems is used to solve the transcendental equation. A gradient based solver (*fminunc*) from MATLAB's optimization toolbox is used with the *trust-region* algorithm and a user-defined gradient of the objective function. To avoid ill-conditioning due to extremely small function values and exit conditions obtained during minimization, logarithmic value of the transcendental equation is taken as the objective function to be minimized.

The initial guess of the wavenumber is supplied by calculating the transverse wave speed and the frequency [133]. The transverse wave speed is calculated using the shear modulus (μ_{total}) and the effective material density (ρ_{eff}). The effective density (ρ_{eff}) of the baseline structures are equal to the material density (ρ=2700 kg/m^3), but for the nonlocal designs, the effective density is calculated by the rule of mixtures using the volume fractions of the LB layer (l), the rigid beam connectors (c), and the NLB layer (n) as presented below:

$$\rho_{eff} = \frac{V_l \ \rho_l + V_c \ \rho_c + V_n \ \rho_n}{V_l + V_c + V_n} \tag{4.2}$$

where V is the volume and ρ is the material density of the specific part of the structure.

The transcendental equation for the antisymmetric mode is solved for wavenumber k_0 at the given frequency ω_0 with the corresponding dynamic nonlocal attenuation factor $\alpha_d(k, \omega_0)$. The optimized wavenumber solutions obtained for range of frequencies are then used to plot the dispersion bands.

3. **Validation of the semi-analytical dispersion:**

The semi-analytical solution is matched with the numerical eigenvalue analysis

based dispersion curves obtained in section 4.2.1. Comparing the dispersion of the structures with common flat LB layer in Fig. 4.17a-b, it is observed that the semi-analytical dispersion curve has a good match with the numerical dispersion curve of TFBF and TTBF for the fundamental bands. It can also be observed that the transcendental equation with dynamic properties obtained using the proposed semi-analytical approach is not an exact match for part of the numerical dispersion bands with zero group velocities, as the Rayleigh-Lamb relations, traditionally derived for the propagating waves, cannot solve for complex wavenumber solutions (decaying waves). Moreover, the numerically obtained displacement profiles $(u(x))$ for nonlocal structures do not capture the dynamic behavior due to the ABH and the nonlocal effects efficiently. Thus, propagating bands of the dispersion curves are matched with good accuracy by using this technique. Following quantitative observations can be summarized about the nonlocal structures with flat LB layer:

(a) It is found that the semi-analytically obtained TFBF dispersion has a maximum deviation of 6.5% from the numerical results (Fig. 4.17a). As the sensitivity of the transcendental equation to α_d increases with increase in the frequency, the deviation in the semi-analytical solutions broadens at higher frequencies.

(b) From the dispersion plot in Fig. 4.17b, it is observed that the maximum deviation in the propagation bands of the semi-analytically obtained dispersion of the TTBF structure is just under 10%. However, the reader can also observe around 18% deviation at the ends of the second band due to the inability of the structural response $(u(x))$ to capture the effect of local resonance of the ABH plate NLB layer in TTBF.

From Fig. 4.18a-b, for structures with common tapered LB layer (TFBT and TTBT), it is observed that the propagating part of the first band is captured with high accuracy. There is a downward shift in the semi-analytically obtained

second dispersion bands due to the inability to capture the complete dynamic response $(u(x))$ of the tapered LB layer of the structures in the higher frequency range. Similar to the flat LB layer designs, the following quantitative observations can be summarized about the nonlocal structures with tapered LB layer:

(a) The semi-analytical dispersion of TFBT has a maximum deviation of 9.6% from the numerical results (Fig. 4.18a) in the first mode, while an error of around 25% is observed at a wavenumber k=1.4, on the inter-junction of the propagating and the standing waves in the second band.

(b) The semi-analytically obtained first dispersion band of TTBT presented in Fig. 4.18b has a maximum deviation of 11% from the numerical results, and a maximum of 20% deviation is observed in the second dispersion band.

(c) A combined effect of the higher sensitivity of the transcendental equation to α_d at high frequencies, the inability of the structure displacements $(u(x))$ to capture taper dynamics of the ABH embedded plates, and the approximated total density (Eq. (4.2)) of the nonlocal designs with tapered LB layer are responsible for the larger deviation in the semi-analytical solutions of the nolocal ABH metastructures (Fig. 4.18).
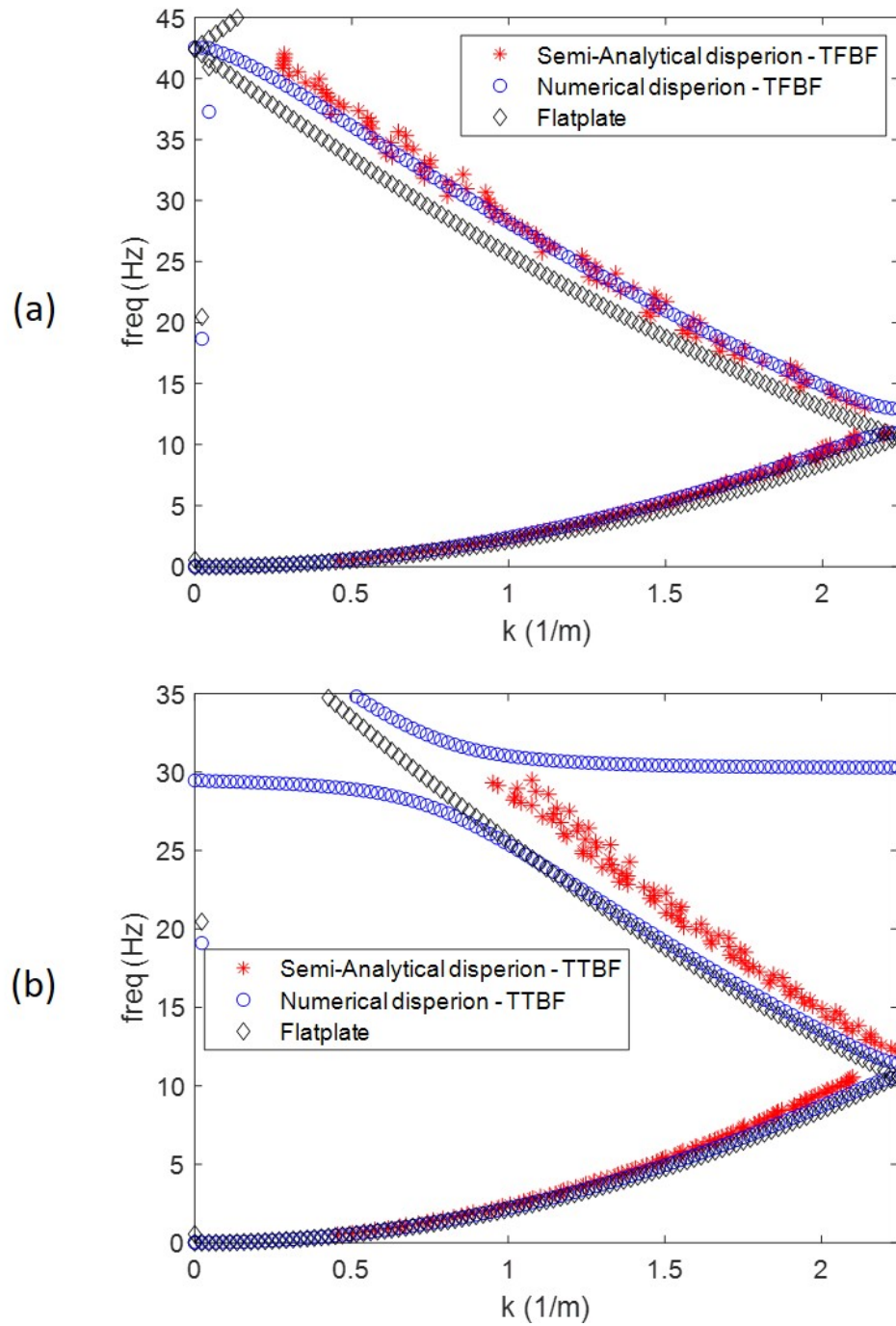
Fig. 4.17.: Dispersion curves obtained semi-analytically and numerically for the nonlocal structure: (a) TFBF, and (b) TTBF.
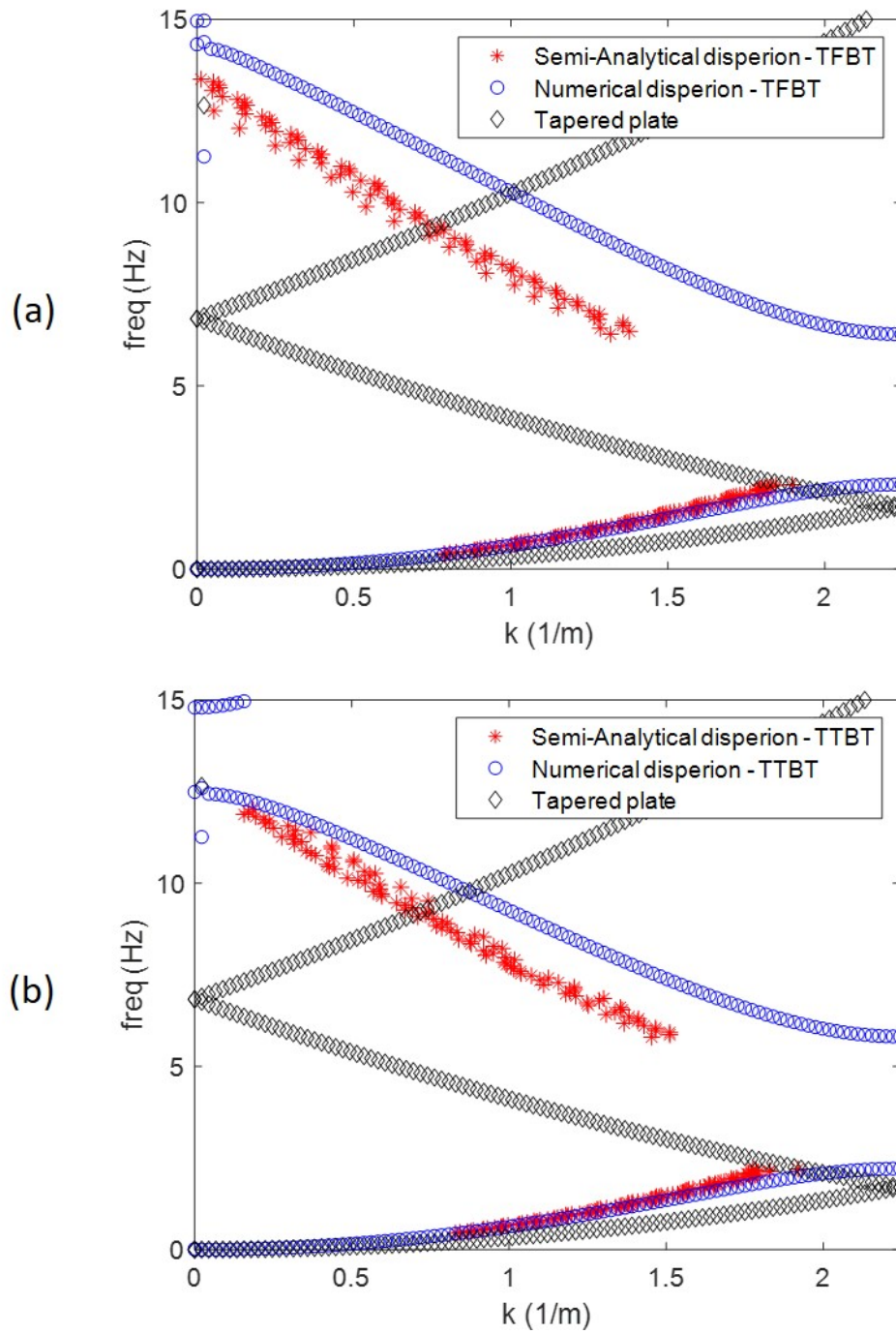
Fig. 4.18.: Dispersion curves obtained semi-analytically and numerically for the nonlocal structure: (a) TFBT, and (b) TTBT.

4.2.3   Steady state forced frequency response

This section investigates the steady state frequency response (refer section 2.4.2) of the proposed designs to a harmonic load. Based on the dynamic behavior obtained, methodologies are developed to evaluate and compare the performance of the individual designs qualitatively. The unit cells of all the designs are subjected to a symmetric boundary condition to replicate structural periodicity on either boundaries. Numerical designs in this work are developed with the aim of enhancing flexural wave damping. Depending on the type of application, either a transfer function based single point response or a spatially averaged damped response over the length of the structure to capture the effect of the energy localization on the baseline structure is evaluated.

When 1 N point load is applied at a position P near the left boundary, the enforced excitation passes through the nonlocal connections throughout the unit cell and a cumulative effect is measured as an output acceleration at a point Q near the right boundary (Fig. 4.19). This method represents a transfer function based numerical technique with force as input and acceleration as output.
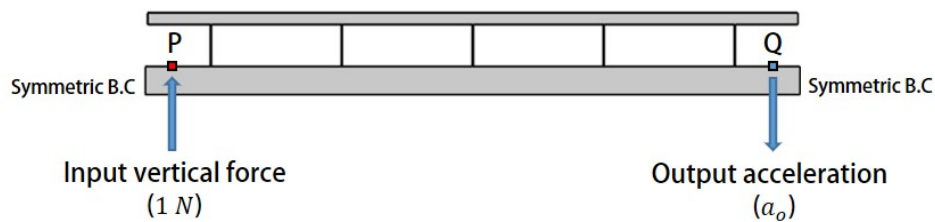
Fig. 4.19.:   Transfer function configuration: A vertical force (F=1 N) at P as input near the left boundary generates point acceleration (a_o) as the output at point Q near the right boundary.
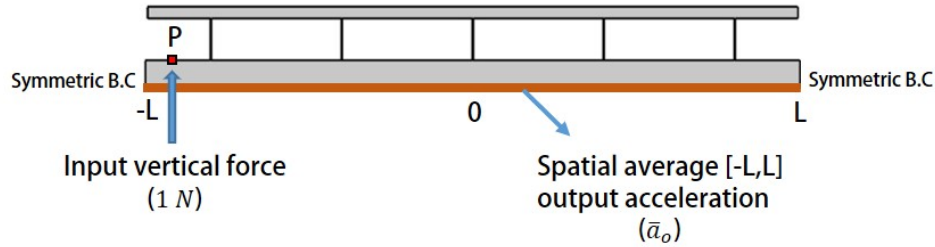
Fig. 4.20.: Spatial average configuration: A vertical force (F=1 N) at point P as input near the left boundary generates an average acceleration ($\bar{a}_o$) output over the length of the unit cell $[-L, L]$.

The transfer function based output acceleration only illustrates the dynamic response at the boundary point Q of the numerical design, and is efficient to measure only the point based transmission outcomes, but certain applications, as mentioned before, make use of the complete structural response for energy attenuation and therefore, we need a methodology to capture the behavior of the whole design. Hence, a spatially averaged output acceleration is measured along the lower edge of each design as shown in Fig. 4.20 to capture the energy attenuation ability of the complete structure. Further, from the previous chapters it is known that the ABH metastructures are most effective with a viscoelastic damping layer on the ABH tapers. Hence, in this section, the spatially averaged output acceleration of all numerical designs with and without damping layers are also compared with the objective of maximizing the attenuation potential of the ABH metastructures. The dimensions of the viscoelastic layers as shown in Fig. 4.21 were chosen from different configurations by trial and error. The results might improve with optimized damping layer dimensions.

Acceleration is chosen as the frequency response output in both the transfer function based and the spatially averaged numerical techniques, as it is a measure of the response energy in the structure and, hence an indicator of the effective structural damping and cut-on frequency of the system. Lower the frequency at which the energy in the structure starts attenuating, lower is its cut-on frequency.

Differences in the impedance of the structures generate irregular responses for the
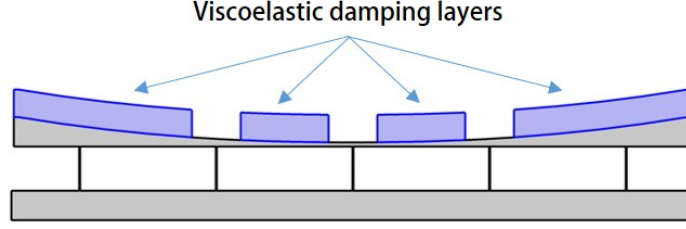
Fig. 4.21.: Schematic illustrates the position of the viscoelastic damping layers on the tapered NLB layer of the TTBF structure. The position of the damping layers along the length of the unit cell remains same for all the proposed designs.

same input force, and in order to compare the output accelerations for various structures in the thesis, a normalization technique is implemented.

$$P_{in} = F \cdot V \tag{4.3}$$

The input power (P_{in}) is defined as the dot product of the input force (F) and the velocity (V) as in Eq. (4.3), and as the response velocity of each structure differs, the input power of the individual design will vary. Hence, the numerically obtained output acceleration is formulated as a function of a factor which scales the supplied input power (P_{in}) to unity in all the structures, as shown below:

$$a_{s_o} = a_o \sqrt{\frac{P_{in}^e}{P_{in}}} \tag{4.4}$$

where P_{in} is the supplied input power, $P_{in}^e = 1\ W$ is the expected unit input power, F is input force at point P, V is input velocity at point P, a_o is the obtained output acceleration, and a_{s_o} is the scaled output acceleration at the point Q.

Similarly, the spatially averaged scaled acceleration $(\bar{a}_{s_o})$ over the entire length of the unit cell with same input force (F) at point P is given by:

$$\bar{a}_{s_o} = \frac{1}{2L} \int_{-L}^{L} a_{s_o} dL \tag{4.5}$$

Based on Eqs. (4.4)-(4.5), the transfer function and the spatially averaged scaled output accelerations are separately plotted with the corresponding frequencies for a given structure.

At first, the numerically obtained frequency dependent scaled acceleration (a_{s_o} and $\overline{a}_{s_o}$) plots of the baseline structures (flat and tapered plates) are compared below.

4.2.3.1   Baseline Structures

The scaled acceleration plots in Fig. 4.22 and Fig. 4.23 compare the dynamic response of the flat and the tapered baseline plates. The energy attenuation of a propagating wave through a given structure is observed as sudden drops in the amplitudes of these acceleration plots. Both a_{s_o} (Fig. 4.22) and $\overline{a}_{s_o}$ (Fig. 4.23) plots depict a gradual and significant deviation between the acceleration responses of tapered and flat baseline plates at a frequency around 65 Hz. The flexural wave propagation wavelength is about 3.5 times the ABH diameter of the tapered baseline plate at 65 Hz and, thus the effectiveness of the ABH taper increases beyond 65 Hz as observed by the dips in a_{s_o} and $\overline{a}_{s_o}$. The threshold frequency at which the energy of the tapered plate response starts attenuating is defined as the *cut-on frequency*. From the $\overline{a}_{s_o}$ plot (Fig. 4.23), it is observed that the cut-on frequency of the tapered baseline design is at a frequency of 65 Hz. Further, as discussed before, the first bandgap of the tapered plate design satisfies the Bragg's criterion (Eq. (A.4)). According to the Bragg's criterion, the first band gap is formed around the frequency at which the propagating wavelength is approximately twice the ABH diameter. Analyzing the dispersion curve and $\overline{a}_{s_o}$ plot of the tapered baseline design, it is observed that the first band gap is developed at a frequency around 170.3 Hz. Further, it can also be noted that the flat baseline plate has high cut-on frequency (no cut-on observed until 300 Hz).

Based on the characteristics of the a_{s_o} and the $\overline{a}_{s_o}$ plots of the baseline structures described above, the scaled output acceleration plots of all the nonlocal designs can

be compared and analyzed separately in the following frequency ranges for better understanding (Fig. 4.22):

1. Low frequency range (f_l) is defined between 0-65 Hz.

2. Mid frequency range (f_m) is defined between 65-170.3 Hz.

3. High frequency range (f_h) is defined between 170.3-300 Hz.
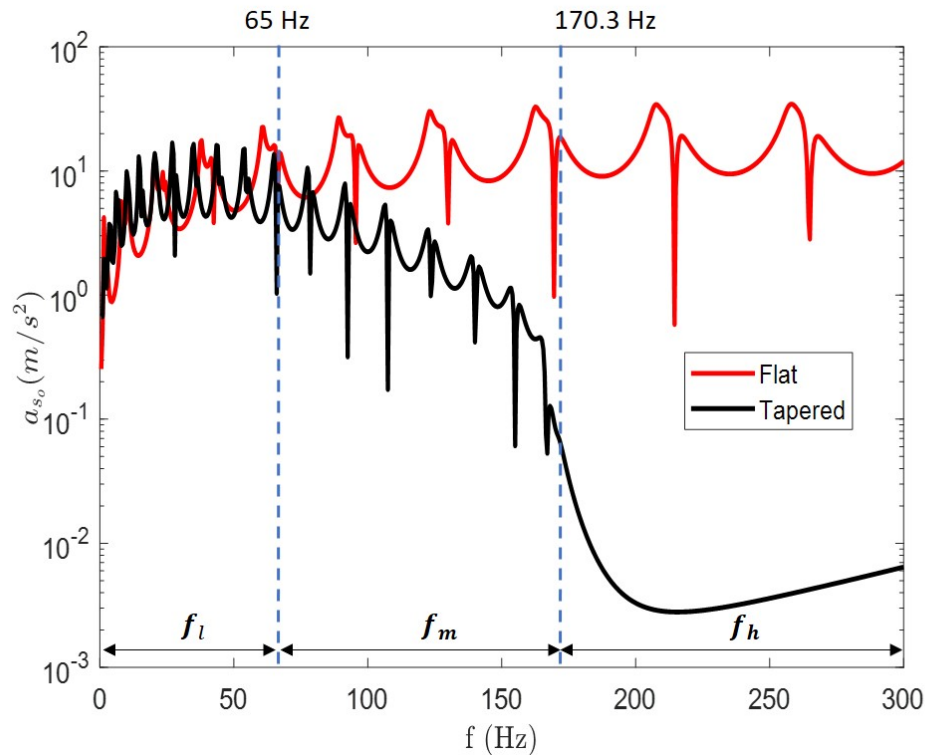
Fig. 4.22.: $a_{s_o} - f$ plot for the flat and tapered baseline plates. The plot is divided into low (f_l), medium (f_m), and high (f_h) frequency ranges. The dotted blue line at $f = 65$Hz represents the cut-on frequency of the tapered baseline plate.

From Fig. 4.22 and Fig. 4.23, it can be noted that the scaled acceleration plots alone are insufficient to understand the effectiveness of a given structure due to the complicated dynamic behavior over this extended range of frequencies. Due to this complex dynamics, a single methodology might not be efficient in vibration attenuation of the
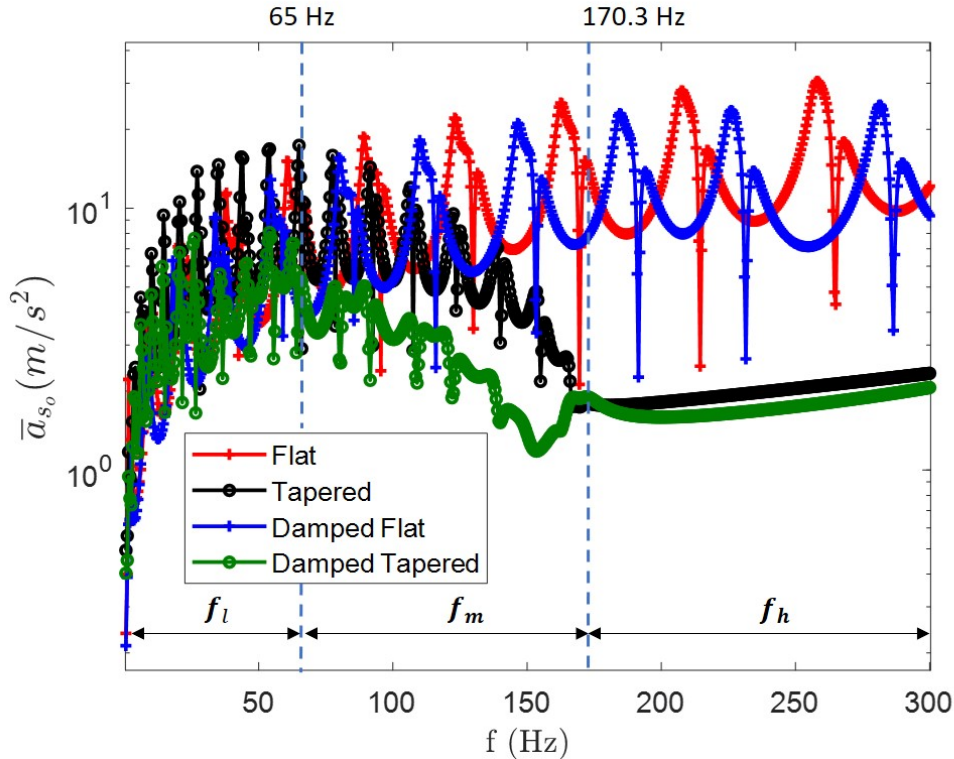
Fig. 4.23.: $\bar{a}_{s_o} - f$ plot for the flat and tapered baseline plates. Similar to $a_{s_o} - f$ plot, it is divided into low (f_l), medium (f_m), and high (f_h) frequency ranges. The dotted blue line at $f = 65$Hz represents the cut-on frequency of the tapered baseline plate and the line at $f = 170.3$ Hz corresponds to the start of the bandgap of the tapered baseline plate.

extended frequency range (0-300 Hz) and, hence the following techniques are proposed as tools to illustrate the overall dynamic behavior of each design in f_l, f_m, and f_h frequency ranges separately:

1. **Normalized acceleration ratio (A_r):** The cumulative dynamic response of the structures, illustrated by the transfer function based scaled acceleration plots in f_l, f_m, and f_h, will be represented by a normalized acceleration ratio (A_r). The ratio $A_r = \dfrac{A_o}{A_i}$, where $A_o = \sum_{j=1}^{n} a_{s_o}^{j}$ is the cumulative scaled output acceleration and $A_i = \sum_{j=1}^{n} a_{s_i}^{j}$ is the cumulative scaled input acceleration over n frequencies, is defined as a metric to measure the effectiveness of the dynamically tailored designs in elastic wave attenuation.

As observed in Fig. 4.24, the tapered baseline plate is effective in vibration attenuation (lower A_r value) compared to the flat baseline plate in f_l and f_m. The effectiveness of the tapered plate in f_h is evident from Fig. 4.22 and, hence is not reiterated in Fig. 4.24.
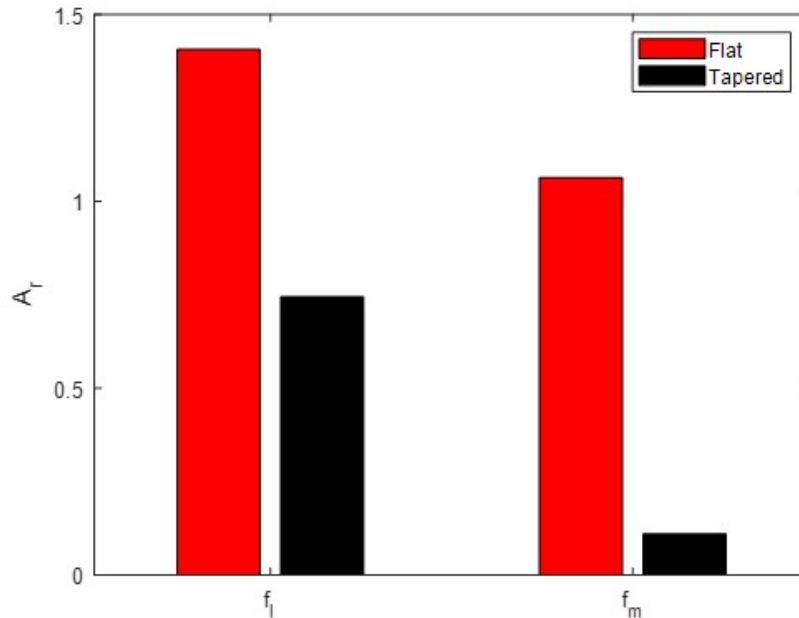
Fig. 4.24.: Comparison of the cumulative normalized acceleration ratio index of the flat and the tapered baseline plates in f_l and f_m ranges.

2. **Normalized mean of the spatial average acceleration (A_m):** The cumulative dynamic response of the structures, illustrated by the spatially averaged scaled acceleration plots, will be represented by a normalized mean of the spatial average acceleration (A_m) over the different range of frequencies (f_l, f_m, and f_h). We define $A_m = \dfrac{\overline{A}_{s_o}}{n \left(\frac{\overline{A}_{s_o}^{i}}{n}\right)_{max}}$, where $\overline{A}_{s_o} = \sum_{j=1}^{n} \overline{a}_{s_o}^{j}$ is the cumulative spatially averaged scaled output acceleration over n frequencies, and $\left(\dfrac{\overline{A}_{s_o}^{i}}{n}\right)_{max}$ represents the maximum value of $\dfrac{\overline{A}_{s_o}}{n}$ among the i undamped and damped designs under comparison.
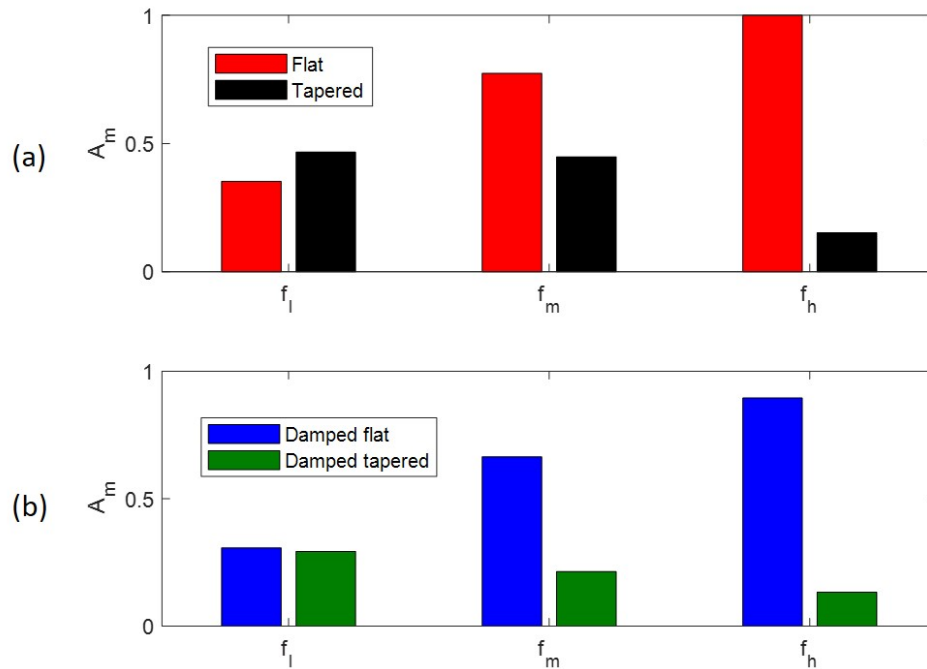
Fig. 4.25.: Comparison of the cumulative normalized mean of the spatial average scaled acceleration index in the f_l, f_m, and f_h ranges of: (a) flat and tapered baseline plates, (b) flat and tapered baseline plates with viscoelastic damping layers.

In Fig. 4.25a, we can observe that although the undamped tapered baseline structure has a better performance in f_m and f_h ranges due to the taper design, the undamped flat baseline plate has better attenuation capability in the f_l range as, in this range, the propagation wavelengths are much larger than the ABH diameter. The addition of viscoelastic damping layer on the ABH significantly enhances the attenuation bandwidth of the tapered baseline plate (lower A_m) in all the frequency ranges as shown in Fig. 4.25b.

All the techniques (a_{s_o}, $\bar{a}_{s_o}$, A_r and A_m) introduced in this section will be used to effectively evaluate and compare the dynamic behavior of all the structures proposed in this thesis in each of the frequency ranges as follows:

4.2.3.2 Low frequency (f_l) performance of the nonlocal designs

In this section, we compare the numerically obtained low frequency dynamic responses of all the nolocal structures and their baseline designs in two parts:

(a) **Transfer function scaled acceleration:**

The normalized acceleration ratio (A_r) in Fig. 4.26 illustrates the wave attenuation potential of all the structures in f_l. The lower A_r amplitudes of the different designs are attributed to their enhanced energy attenuation capability. It is observed that the introduction of the nonlocal NLB layer enhances the wave attenuation capability of the baseline designs as evident from the lower A_r amplitudes of TFBF, TTBF, TFBT, and TTBT designs compared to their respective baseline models. Owing to the zero reflection property of the ABHs, the introduction of the ABH plate NLB layer (as in TTBF or TTBT) further increases the energy attenuation bandwidth in comparison to the use of flat plate NLB layer (as in TFBF and TFBT) on the same baseline structure. The transfer function based A_r plot (Fig. 4.26) only illustrates the cumulative dynamic behavior of the nonlocal designs in the f_l range. In depth analysis of the a_{s_o} plots (Fig. 4.27) of flat, TTBF, tapered and TTBT designs are carried out to explore the complete dynamic behavior of these structures for individual frequencies in the f_l range. The following major characteristics are observed in Fig. 4.27:

(i) Although the performance of the baseline and the nonlocal designs have similar effects in the ultra-low frequency range from 0-25 Hz, it is observed that the nonlocal designs (TTBF and TTBT) attenuate more flexural energy within certain short frequency bandwidths marked by the drop in the output acceleration, as at positions 1 and 2 in Fig. 4.27.

(ii) Comparison of the displacement profiles (Fig. 4.28) of the flate plate, TTBF, tapered plate, and TTBT about the position 3 in Fig. 4.27 illustrates the role of the introduced nonlocal ABH plate NLB layer in
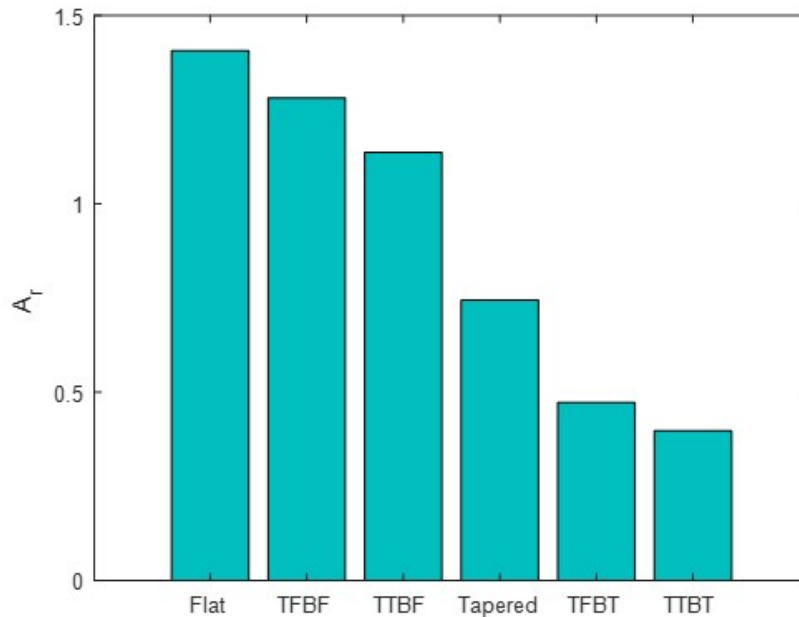
Fig. 4.26.: Comparison of the cumulative normalized acceleration ratio (A_r) of flat, TFBF, TTBF, tapered, TFBT, and TTBT in the f_l range.

controlling the energy attenuation capability of the structure. Comparing the a_{s_o} magnitudes of the local and the nonlocal designs at f=30 Hz in Fig. 4.28, it is observed that the flexural wave energy is significantly attenuated by the introduction of the nonlocal ABH plate NLB layers in TTBF and TTBT.

(iii) The significant drop in the output acceleration at position 4 (Fig. 4.27) corresponds to a wide bandgap (no wave propagation) as observed in the displacement profile of TTBT at a frequency around f=47.5 Hz (position 4) in Fig. 4.29a. The absence of similar low acceleration bandwidth in TTBF signifies the importance of the synergistic effect of the ABH plate NLB layer and the tapered LB layer in enhancing the flexural energy attenuation bandwidth.
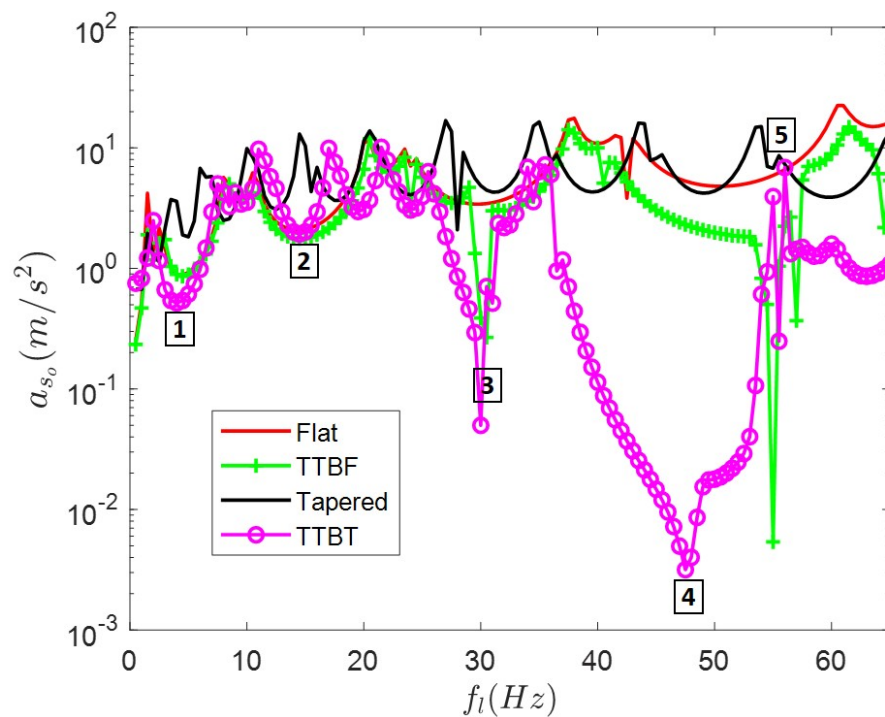
Fig. 4.27.: Scaled output acceleration plot of flat plate, TTBF, tapered plate, and TTBT in the low frequency (f_l) range.
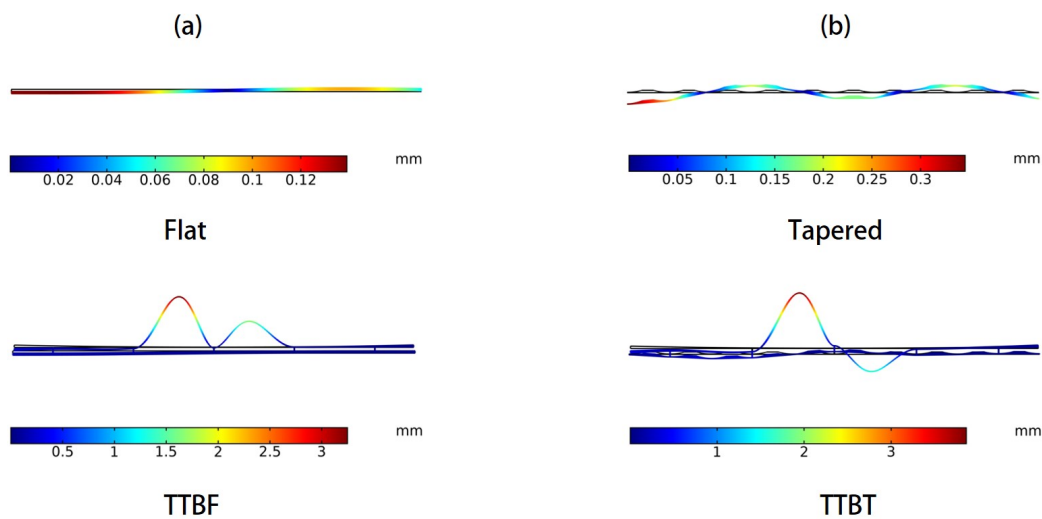
Fig. 4.28.: Displacement profiles of the different configurations at 30 Hz (position 3): (a) flat baseline plate (top) and its nonlocal design TTBF (bottom), (b) tapered baseline plate (top) and its nonlocal design TTBT (bottom).
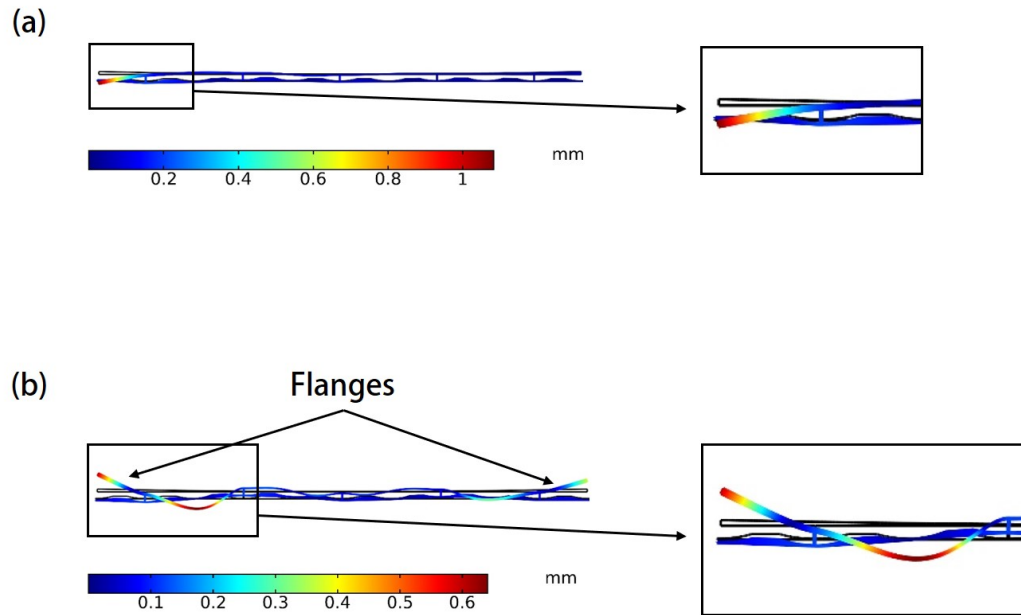
Fig. 4.29.: Displacement profiles of TTBT with zoomed in location of the localized energy on the NLB layer: (a) at 47.5 Hz (position 4) and (b) at 57 Hz (position 5).

(iv) Continuing from position 4 in Fig. 4.27, the sharp rise observed in the output acceleration around position 5 is due to the localized vibration of the flanges of the nonlocal NLB layer, as shown in Fig. 4.29b. As it is hard to control the dynamic behavior of the individual parts of a heterogeneous structure in the design phase, the author proposes to dampen these local resonances using a viscoelastic layer.

(v) In general, the scaled output acceleration plots are observed to have sudden drop in the acceleration amplitudes as depicted by the regions around the positions 1,2,3, and 4, marked in Fig. 4.27. The displacement profiles at frequencies close to these positions indicate the complete attenuation of the flexural energy (Fig. 4.28-4.29a). As it is known that the *bandgaps* correspond to the frequencies at which the input wave fails to propagate through the structure (forming evanescent waves), the bandwidths around the above mentioned positions in Fig. 4.27 can be interpreted as

bandgaps. Complementing the above statement, it is noted that the frequency bandwidth of the rectangular patches depicted in Fig. 4.30 overlaps the bandgaps observed in the dispersion curve of the TTBT structure. Similar comparisons can be produced for all other nonlocal structures.
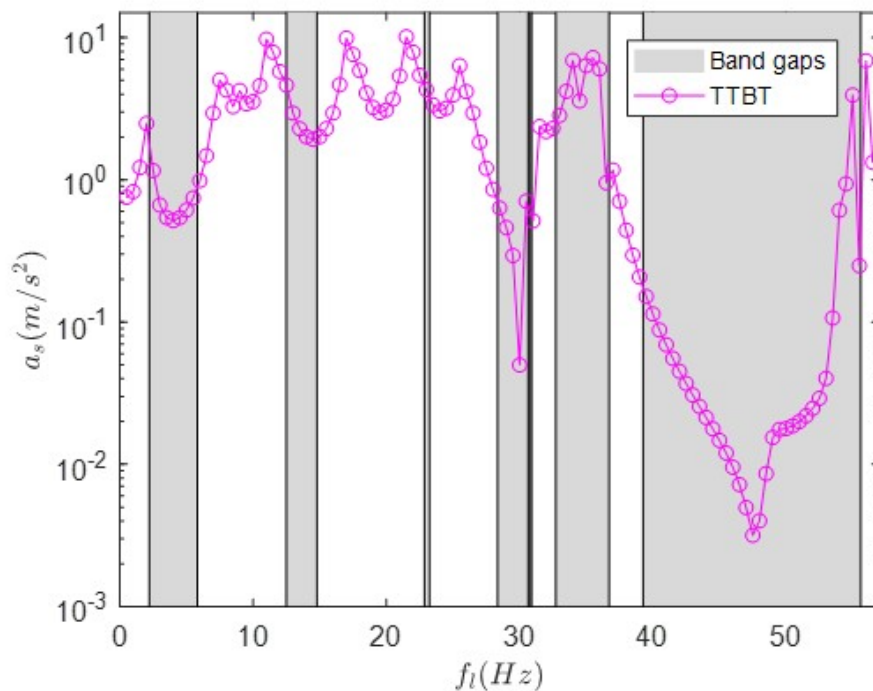
Fig. 4.30.: Scaled acceleration plot of TTBT with its band gaps in the low frequency range

(b) **Spatial average scaled acceleration:**

As mentioned in the last section, the transfer function based A_r and a_{s_o} plots help evaluating the dynamic response of the structure at a boundary point, hence they do not capture the complete dynamic behavior. In this section, we will compare the spatially averaged scaled acceleration based A_m and $\bar{a}_{s_o}$ plots of undamped and damped structures focusing on the response over the complete length of the structure. Comparison of the A_r plots of the baseline structures were presented in the previous section, here we will focus on the A_m plot based comparisons of the nonlocal designs. The A_m plot in Fig. 4.31 illustrates the

wave attenuation potential of all the structures with and without viscoleastic damping layers in the f_l range. From Fig. 4.31, it can be observed that all the undamped and damped nonlocal designs have enhanced attenuation capabilities (lower A_m magnitudes) compared to the baseline structures. Conceptually, the increase in the stiffness and the mass of a structure reduces the damping ratio of the structure. Although the nonlocal designs have higher mass and stiffness compared to their baseline designs, a higher damping is observed in these nonlocal designs. Therefore, the geometric nonlocal connections introduced in these structures are responsible for the increase in the damping. It can also be noted that all the designs with tapered LB layer have higher A_m value compared to their flat LB layered counterparts due to the higher flexibility of the tapered design.

Further, the $\overline{a}_{s_o}$ plots of the damped nonlocal designs in f_l are compared to analyze the detailed dynamic behavior of the nonlocal designs. The $\overline{a}_{s_o}$ and a_{s_o} plots of undamped structures match at their peak and drop positions. The difference is observed only on the magnitudes of the spatially averaged scaled acceleration. Due to this similarity between $\overline{a}_{s_o}$ and a_{s_o} plots of the undamped structures, this section will present only the $\overline{a}_{s_o}$ plots for damped structures. The following observations are made from the $\overline{a}_{s_o}$ plot in Fig. 4.32:

(i) Similar to the observation made in the a_{s_o} plot (Fig. 4.27) in f_l range, we observe that in the ultra-low frequency range from 0-25 Hz of Fig. 4.32, the performance of the baseline and the nonlocal designs remain same except for certain narrow frequency ranges, marked by positions 1-4 in Fig. 4.32. The TTBT and TTBF designs have better performance in the specific frequency ranges as observed at positions 1,4 and 2,3 respectively.

(ii) The second chapter illustrated that the damped ABH metastructures are effective passive vibration attenuation methods in the low frequency ranges. On the contrary, in Fig. 4.32, we observe that the stiffer and heavier damped nonlocal TTBT design has better energy attenuation behavior
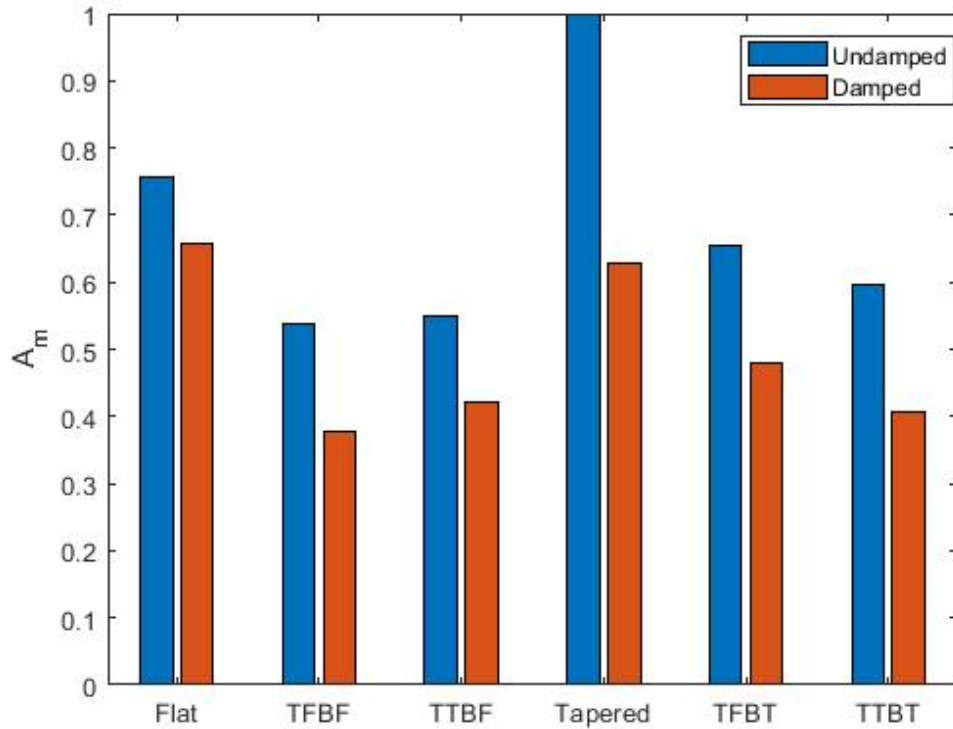
Fig. 4.31.: Comparison of the mean of the spatial average scaled acceleration of all (undamped and damped) structures in the f_l range.

(lower A_m) at positions 1-4 compared to the damped tapered baseline plate. Hence, the nonlocal NLB layer has enhanced the attenuation capability of the tapered baseline plate in f_l.

(iii) The position 5 in the a_{s_o} plot of the undamped TTBT design (Fig. 4.27) is marked by a peak due to the local resonance of the flanges and ABH plate NLB layer, but a drop in this peak at position 5 as shown in the $\overline{a}_{s_o}$ plot in Fig. 4.32 for damped TTBT structure is due to the addition of the viscoelastic damping layer. Hence, the addition of damping layers improves the energy attenuation capability of the proposed nonlocal ABH metastructures.
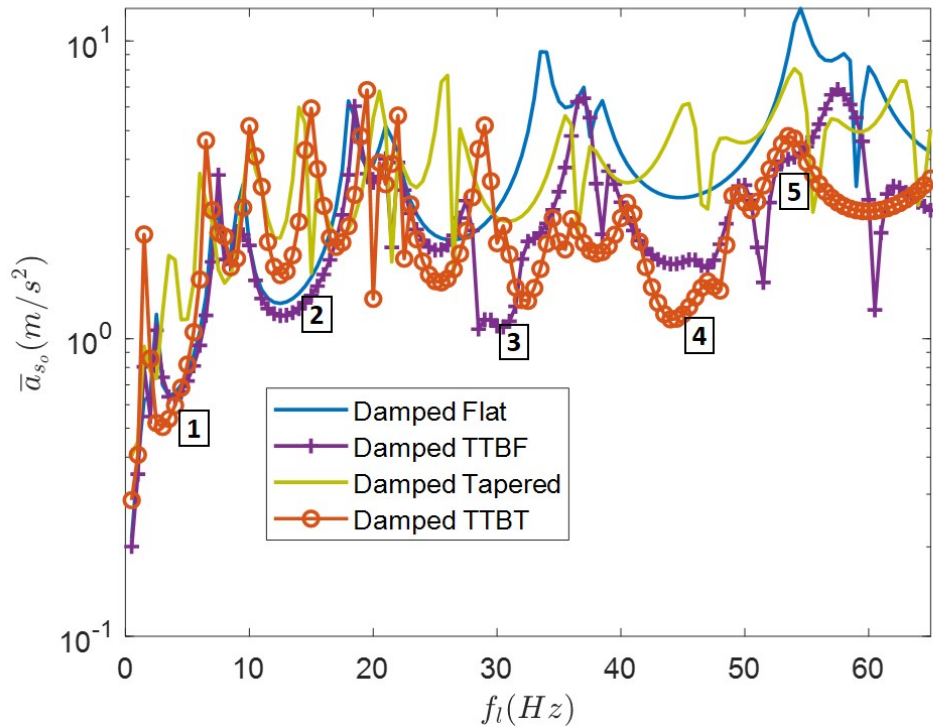
Fig. 4.32.: Comparison of the spatial average scaled acceleration of flat plate, TTBF, tapered plate, and TTBT with viscoelastic damping layers in the f_l range.

(iv) The displacement profile comparison of the undamped and the damped TTBT structure in Fig. 4.33 indicates the energy localization on the NLB layer of the nonlocal designs in f_l. From Fig. 4.33a, we know that the flexural energy is localized on the NLB layer, and this localized response is attenuated (Fig. 4.33b) when a viscoelastic damping layer is introduced on the NLB layer.

(v) From the descriptions above, it can be noted that a single structure cannot be deemed as the best design within f_l as different designs with damping layers have enhanced attenuation capabilities in different narrow frequency ranges. Hence, we split the f_l range further and plot A_m for each design in smaller frequency bins as shown in Fig. 4.34. Based on the application, a

(a)

(b)
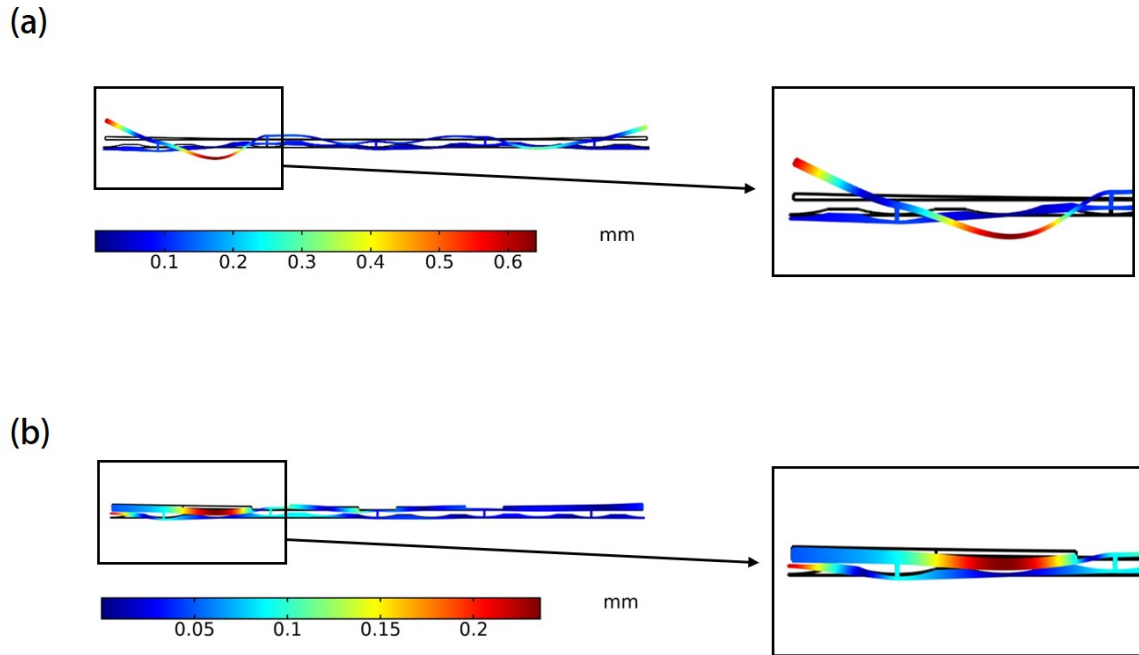
Fig. 4.33.: Displacement profiles at 57 Hz (position 5) with zoomed in location of the localized energy on the NLB layer of: (a) undamped TTBT and (b) damped TTBT.

particular nonlocal design can be chosen to work for the required ultra-low frequency attenuation range from Fig. 4.34.

Following important characteristics can be summarized about the dynamic behavior of all the damped and the undamped structures from Fig. 4.34:

- Although it is difficult to shortlist a single effective design for use in f_l, from the A_m plots of both damped (Fig. 4.34a) and undamped (Fig. 4.34b) designs, it can be concluded that nonlocal designs (TFBF, TTBF, TFBT, and TTBT) can more effectively attenuate flexural energy compared to their corresponding baseline designs (flat and tapered plates).
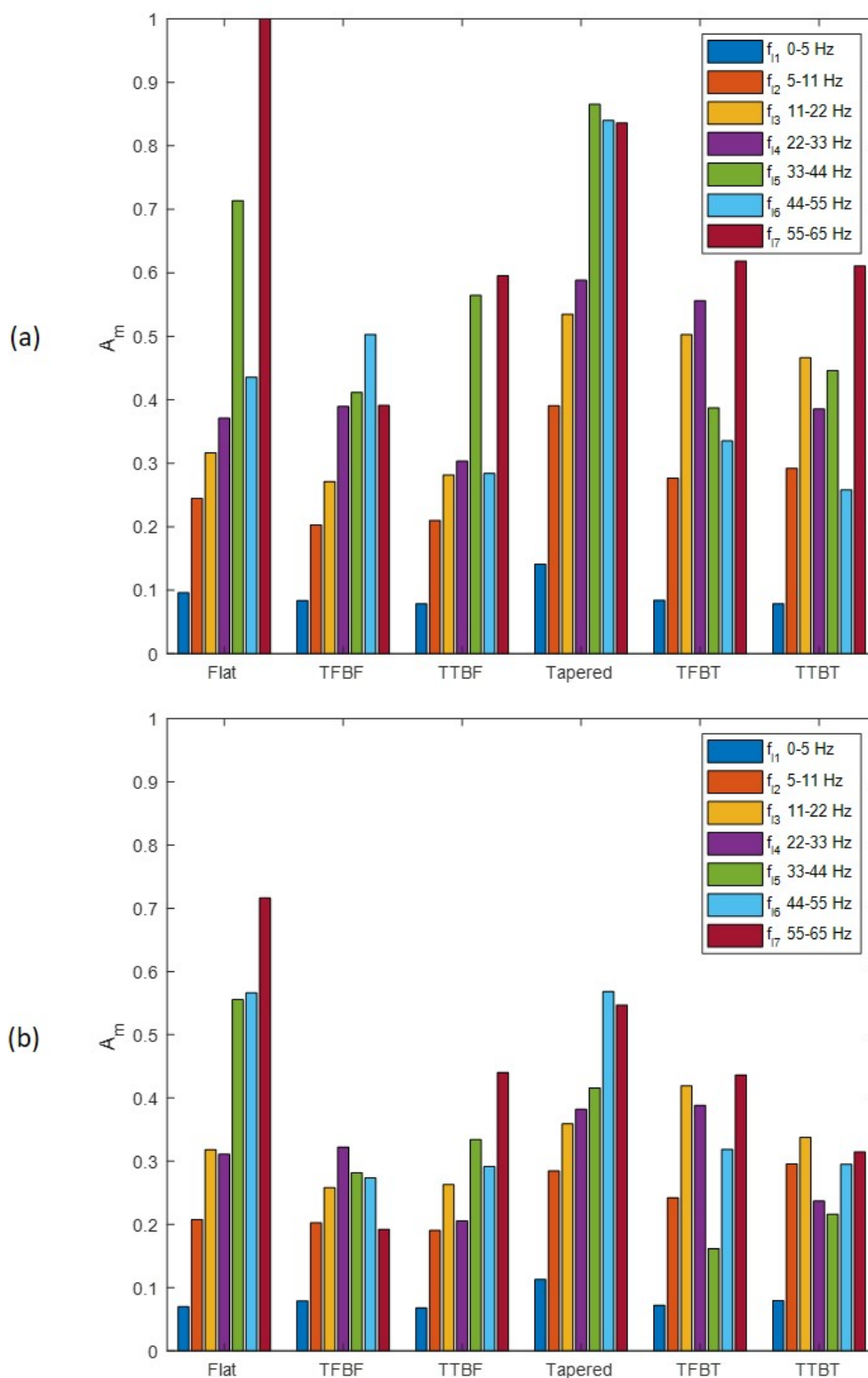
Fig. 4.34.: Schematic comparing the A_m amplitudes in ultra-low frequency bins within f_l for: (a) all the undamped structures, (b) all the damped structures.

- The damped TTBF design effectively attenuates flexural energy in f_{l1}, f_{l2}, and f_{l4} bins, while the damped TFBF design is effective in f_{l3}, f_{l6}, and f_{l7} bins. The f_{l5} bandwidth is most efficiently attenuated by the damped TFBT structure. Similar comparisons can be drawn for the undamped structures also.

4.2.3.3   Mid frequency (f_m) performance of the nonlocal designs

This section will compare the numerically obtained dynamic characteristics of the nonlocal structures in the mid frequency (f_m) range from 65-170.3 Hz in two parts:

(a) **Transfer function scaled acceleration:**

The normalized acceleration ratio (A_r) plotted in Fig. 4.35 illustrates the effectiveness of the individual design in flexural wave attenuation in the f_m range. It can be observed that beyond the cut-on frequency of the tapered plate (65 Hz), nonlocal models proposed with the tapered LB layer are more effective in vibration attenuation than the nonlocal models with the flat LB layer. Although TTBT showcases better wave attenuation characteristics than the tapered baseline plate in f_m, the tapered baseline plate is observed to have a better performance (lower A_r) than TFBT in the same frequency range (Fig. 4.35). Further, the a_{s_o} plots of the nonlocal designs with tapered LB layer will be analyzed for better understanding of their dynamic behavior in f_m. The following observations can be made about the dynamic behavior of the nonlocal designs with a tapered LB layer in the f_m range from Fig. 4.36:

  (i) The nonlocal designs of TFBT and TTBT with common tapered LB layers (Fig. 4.36) have scaled acceleration peaks at approximate positions 6 and 7 due to the local resonance of the low thickness regions on the ABH plate NLB layer. The energy is localized on the NLB layer at these frequencies. It is noted that the tapered baseline plate attenuates more energy than the nonlocal designs at these positions.
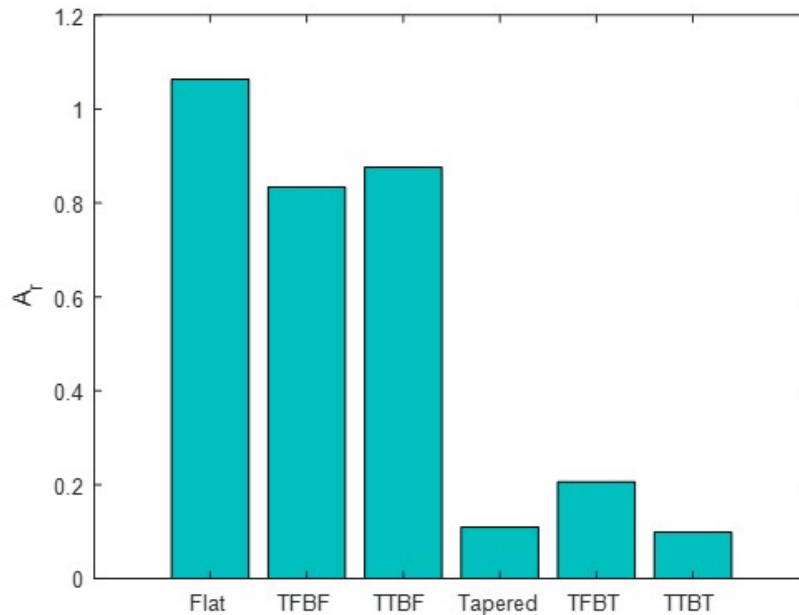
Fig. 4.35.: Comparison of the cumulative normalized acceleration ratios (A_r) of flat, TFBF, TTBF, tapered, TFBT, and TTBT in the f_m range.

(ii) In the frequency range from positions 7-8, the energy is significantly attenuated by the structures with the tapered LB layer as compared to the flat LB layer designs due to the ability of the ABHs to attenuate shorter wavelengths beyond its cut-on frequency.

(iii) The presence of the ABH plate NLB layer in addition to the tapered LB layer, as in TTBT design, effectively enhances the small wavelength (relative to the ABH dimension) attenuation capability in f_m as marked by the low a_{s_o} value at position 8.

(b) **Spatial average scaled acceleration:**

We compare the spatially averaged scaled acceleration of both the undamped and the damped structures in f_m. The A_m plot (Fig. 4.37) clearly indicates the effectiveness of the structures with the tapered LB layer over the flat LB layer based designs. As the ABH effect is significant after the cut-on frequency
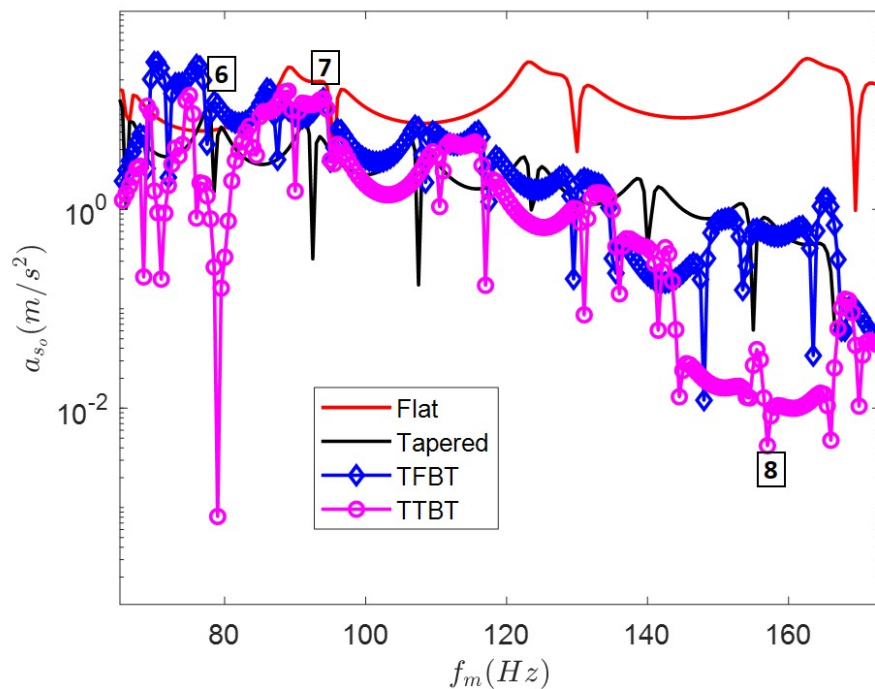
Fig. 4.36.: Scaled output acceleration plot of flat plate, tapered plate, TFBT, and TTBT in the medium frequency (f_m) range.

and as the TTBT design with the nonlocal ABH plate NLB layer has lower damping ratio, the damped tapered baseline plate is visibly the most effective design in the f_m range. It should be noted that a hierarchical structure with an optimized NLB layer might improve the performance of TFBT and TTBT designs in f_m.

Further, the complex dynamics of all the damped structures in f_m are compared using the $\bar{a}_{s_o}$ plot in Fig. 4.36. The major conclusions from this comparison are summarized as follows:

(i) Comparing the peaks at positions 6 and 7 in Fig. 4.36 with the same positions on the $\bar{a}_{s_o}$ plot in Fig. 4.38, it is observed that the peaks of TTBT structure are attenuated by the addition of damping layer, while the effect of viscoleastic damping on TFBT is insignificant. The addition of damping layer on the ABH attenuates the localized energy on the ABH
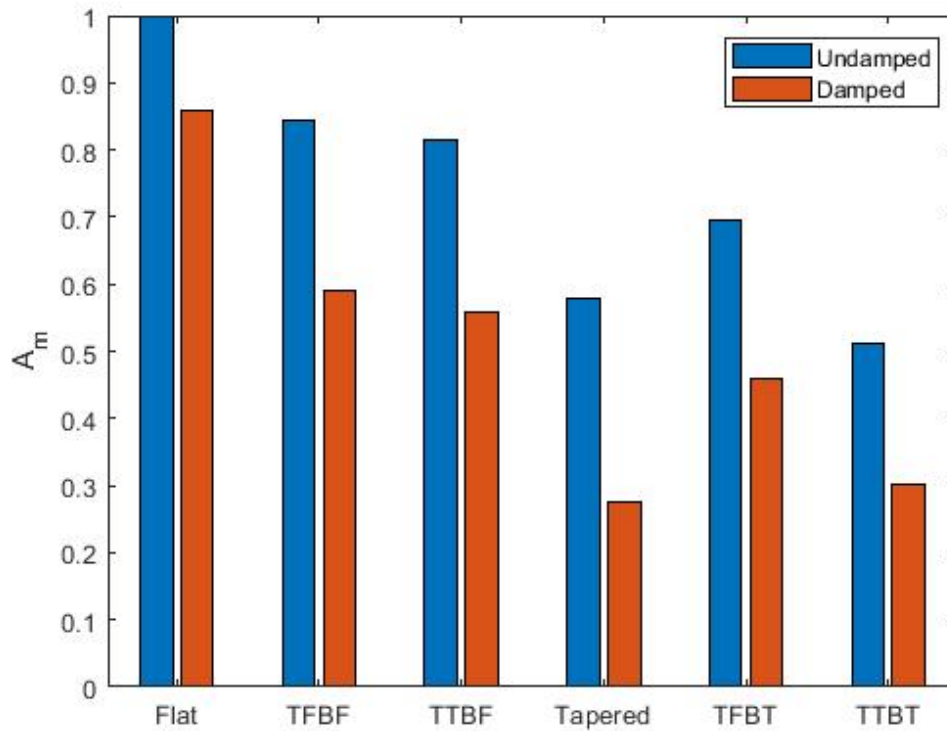
Fig. 4.37.: Comparison of the mean of the spatial average scaled acceleration of all the undamped and the damped structures in the f_m range.

plate NLB layer of the TTBT structure, while the application of the same amount of damping material has negligible effect on the flat plate NLB layer of TFBT design.

(ii) In the higher frequency range beyond position 7 in the $\overline{a}_{s_o}$ plot (Fig. 4.38), the predominant short wavelength (about 2 times the ABH diameter) absorption property of the ABH overshadows the nonlocal effect created by the damped TFBT and the damped TTBT designs, hence these stiffer structures have lower damping compared to the tapered baseline plate in f_m. Peaks of the damped TFBT and the damped TTBT at position 8 can be attributed to the local resonance of the added viscoelastic material.
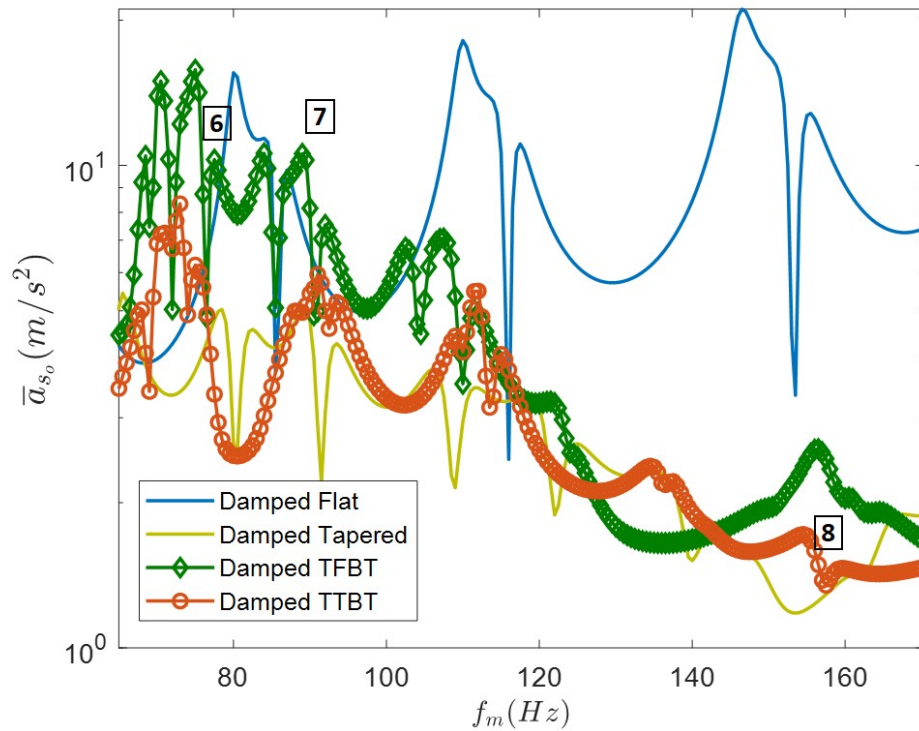
Fig. 4.38.: Comparison of the spatial average scaled acceleration plots of flat plate, tapered plate, TFBT, and TTBT with viscoelastic damping layers in the f_m range.

As all the structures in f_m are observed to have uniform dynamic behavior after 100 Hz (Fig. 4.36 and Fig. 4.38), the A_m plots with subdivided frequency bins are not evaluated for this mid frequency range.

4.2.3.4   High frequency (f_h) performance of the nonlocal designs

This section will compare the dynamic characteristics of the nonlocal structures in the high frequency (f_h) range from 170.3-300 Hz in two parts:

(a) **Transfer function scaled acceleration:**
All the designs with the tapered LB layer (tapered baseline plate, TFBT, and TTBT) are observed to have enhanced flexural wave attenuation property in f_h as indicated by the extremely low A_r amplitudes in Fig. 4.39. The frequency

bandgap (170.3-450 Hz) generated by the combined effect of the periodicity of the metastructure and the effective energy absorption property of the ABH tapers is responsible for the extremely low output acceleration of the tapered baseline plate. Therefore, this section will focus on comparing the dynamic behavior of all the designs with tapered LB layer.

Further, lower A_r amplitude of the tapered baseline plate in comparison to TFBT and TTBT (nonlocal designs) in f_h indicates the superposition of the nonlocal effect by the energy absorption characteristics of the ABH taper beyond the first bandgap. The reduction in the flexural energy attenuation capability of the nonlocal designs in f_h is due to the high frequency response of the additional mass and stiffness introduced by the nonlocal NLB layer. At low frequencies, the nonlocal effect overshadows the reduction in attenuation due to the added mass and stiffness.

The introduction of a nonlocal NLB layer with optimized dimensions and material properties might improve the effectiveness of the nonlocal designs in the f_h range. The frequency dependent dynamic behavior of the structures in the f_h range is nearly uniform throughout as shown in the a_{s_o} plot in Fig. 4.40. Therefore, the cumulative scaled acceleration based A_r plot in Fig. 4.39 can also represent the individual frequency dependent dynamic behavior of all the structures in the f_h range accurately, unlike the varied dynamic response in the smaller bins (Fig. 4.34) of f_l. The peaks observed in Fig. 4.40 around $f=180$ Hz for TTBT and around $f=270$ Hz for TFBT are due to the localized response of the added nonlocal ABH plate NLB layer and flat plate NLB layer respectively.
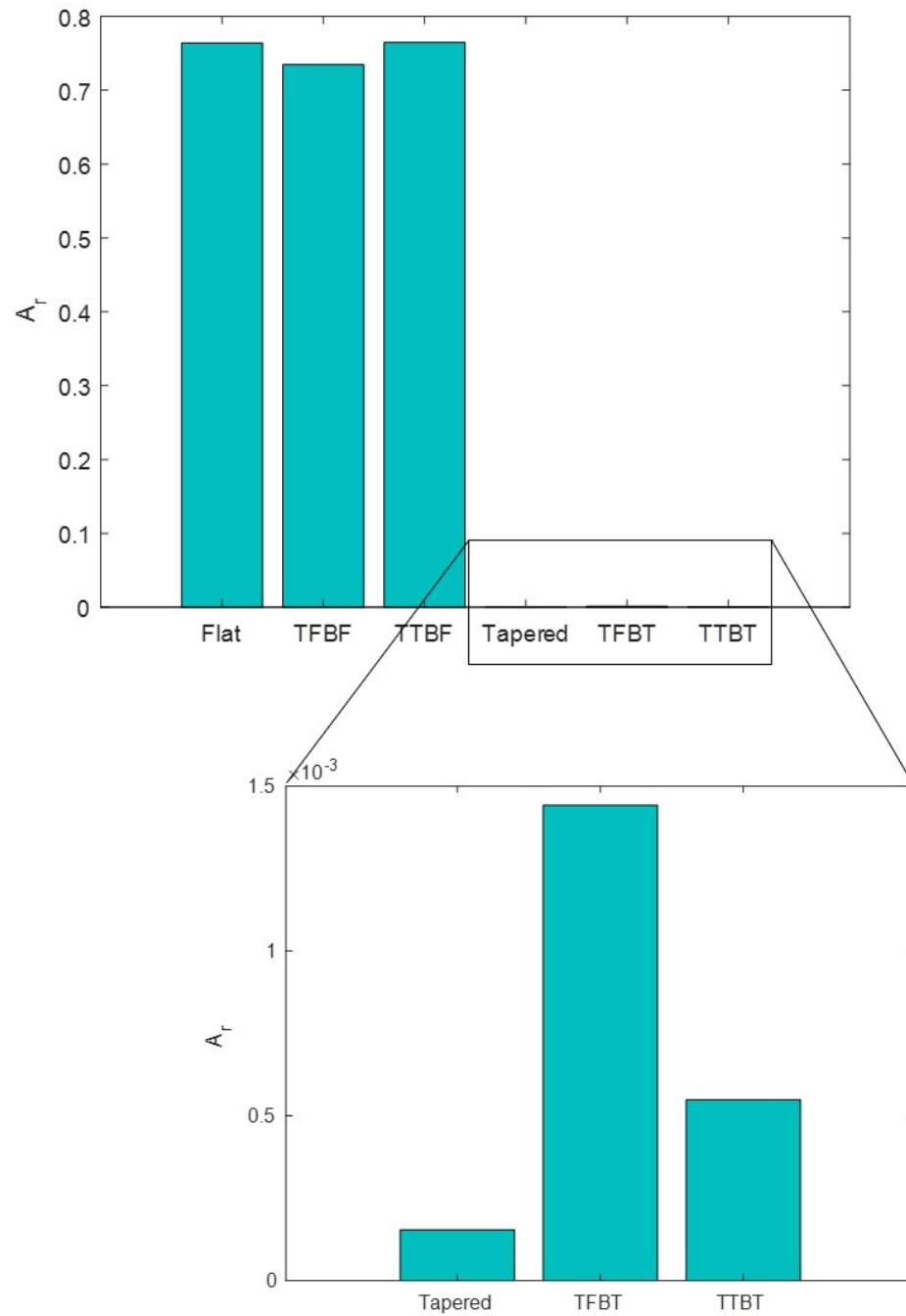
Fig. 4.39.: Comparison of cumulative normalized acceleration ratio (A_r) of flat, TFBF, TTBF, tapered, TFBT, and TTBT in the f_h range (top). Zoomed in image of the A_r plot for tapered plate, TFBT, and TTBT is also presented (bottom).
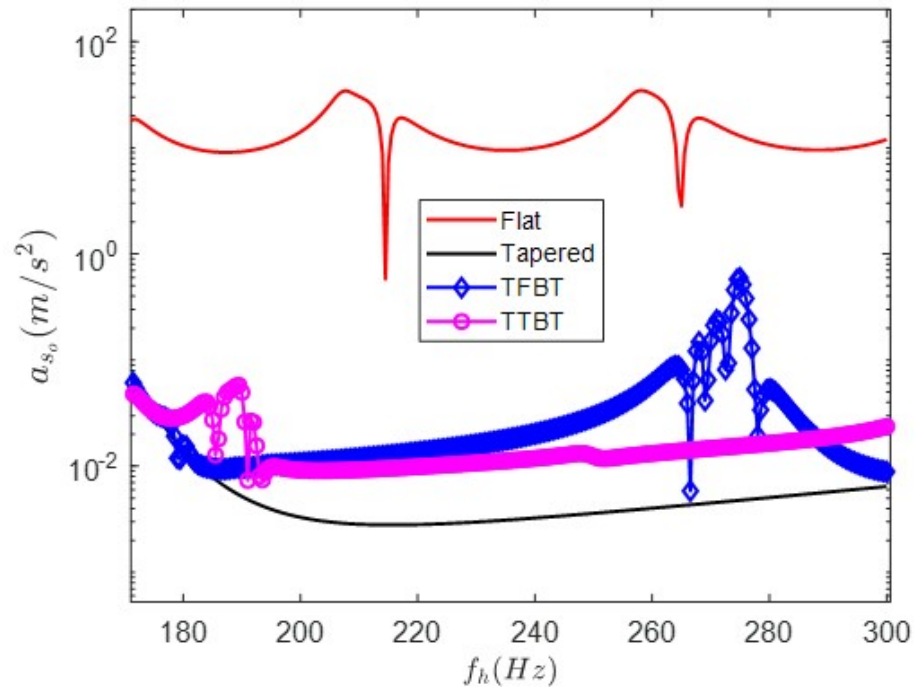
Fig. 4.40.: Scaled output acceleration plot of tapered plate, TFBT and TTBT in the high frequency (f_h) range

(b) **Spatial average scaled acceleration:**

We compare the spatial average scaled output acceleration of all the undamped and the damped structures in f_h range. Similar to A_r plot (Fig. 4.39) in f_h, low A_m amplitudes (Fig. 4.41) of the designs with the tapered LB layer is attributed to the energy attenuation effectiveness of the structure in f_h. Comparing the A_m amplitudes of the damped tapered LB layer designs (damped tapered baseline plate, damped TFBT, and damped TTBT), enhanced energy attenuation is observed in the damped tapered baseline plate due to the effective wave absorption property of the embedded ABHs in f_h. The damped TFBT and TTBT designs in comparison to the tapered baseline plate design are observed to have lower energy attenuation in f_h as the nonlocal effect is overshadowed by the damping reduction due to the added mass and stiffness.
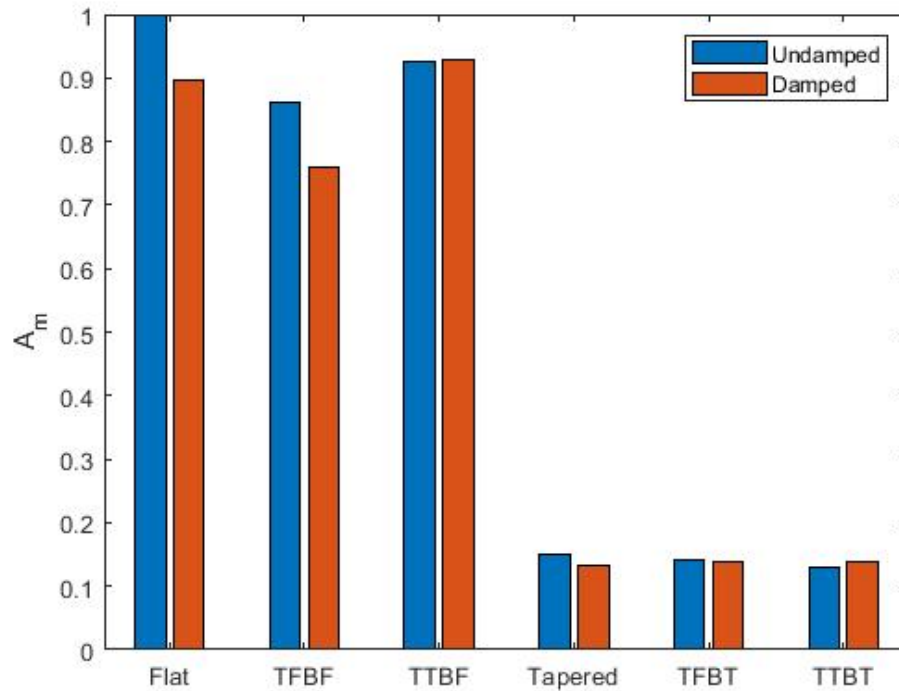
Fig. 4.41.: Comparison of mean of the spatial average scaled acceleration of all the undamped and the damped structures in the f_h range.
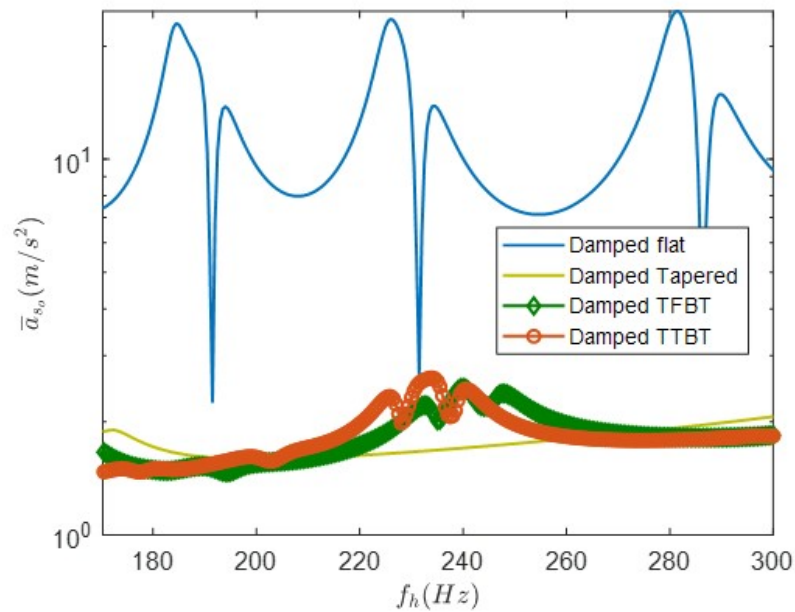

Fig. 4.42.: Comparison of spatial average scaled acceleration plots of flat plate, tapered plate, TFBT, and TTBT with viscoelastic damping layers in the f_h range.

Similar to the a_{s_o} plot in Fig. 4.40, the $\bar{a}_{s_o}$ plot in Fig. 4.42 describes the uniform dynamic behavior of the structures with tapered LB layer in f_h. The $\bar{a}_{s_o}$ peaks of TFBT and TTBT (Fig. 4.42) around $f=235$ Hz can be associated with the localized responses of the added nonlocal NLB layers.

4.2.3.5 Summarizing the results of the forced frequency response study

The previous sections compared the dynamic behavior of all the structural configurations proposed in this work. The analysis was performed in three separate frequency ranges, namely f_l, f_m, and f_h. As the response of the baseline and the nonlocal configurations vary significantly over the range of frequencies, this section will focus on summarizing the major observations and conclusions based on the forced frequency response dynamic study. The major results in each frequency range are listed below:

1. *Low frequency range (f_l):*

    (i) The introduction of the nonlocal NLB layer enhances the energy attenuation capability of the baseline models in f_l by localizing the flexural energy on the added NLB layer.

    (ii) The nonlocal effect is significant in f_l, whereas the wave absorption property of the ABH has minimal effect in this long wavelength regime. This nonlocal effect is controlled by the added NLB layer.

    (iii) The addition of viscoelastic damping layer has minimal effect on enhancing the energy attenuation in the ultra-low frequency regimes from $f_{l1} - f_{l3}$.

    (iv) In the $f_{l4} - f_{l7}$ frequency range, the damped nonlocal designs have better performance in comparison to their undamped versions as the localized response of the extended flanges of the NLB layer and of the ABH center are attenuated by the viscoelastic damping layers.

(v) The cut-on frequency of the ABH metastructures are controlled by the properties of the tapers. A single taper of large radius is used for a nonlocal ABH plate NLB layer, while the tapered LB layer consists of ten tapers with small radii. As a significant structural strength is provided by the LB layer, the taper profile in the LB layer controls the cut-on frequency of the tapered baseline plate, the TFBT, and the TTBT designs. Hence, no significant change in the cut-on frequency is observed by introducing the nonlocal effect.

2. *Mid frequency range (f_m):*

(i) Once above the cut-on frequency of the tapers (f=65 Hz), the ABH metastructures start localizing and eventually absorbing flexural waves when damping is used. Hence, in the f_m range, all the structures with the tapered LB layer will effectively attenuate the flexural energy.

(ii) Although the flexural energy absorption by the ABH enhances significantly above the cut-on frequency, the nonlocal effect is superimposed with the reduction in the damping ratio due to the added mass and stiffness of the nonlocal NLB layer at the higher frequencies in f_m.

(iii) Among the different configurations presented above, the TTBT is the most effective design based on transfer function considerations in f_m, while the tapered baseline plate has better attenuation behavior for applications involving the spatially averaged responses. An optimized nonlocal top layer can enhance the energy attenuation of TTBT in f_m.

3. *High frequency range (f_h):*

(i) The tapered baseline plate effectively attenuates energy in f_h as this frequency range corresponds to the first bandgap of the ABH taper (where the Bragg's criterion is satisfied).

(ii) Similar to f_m, among the designs proposed, the tapered baseline plate has better attenuation performance than its stiffer nonlocal models at high frequencies. An optimized nonlocal top layer can enhance the energy attenuation bandwidth of TFBT and TTBT in f_h.

5. CONCLUSIONS AND RECOMMENDATIONS

5.1 Research Summary

This thesis explored a novel design approach for ABH metastructures that leverages the use of intentionally engineered nonlocality. The main objective was to design load bearing thin walled structures capable of enhanced vibration attenuation performance in the ultra-low frequency range.

In traditional local elastic structures, the stress at a point depends only on the local strain field at that point. In nonlocal structures, the stress at a given point depends on the strain field in a finite area around the point, the so-called horizon of nonlocality. In this work, the nonlocal effects were intentionally introduced using a geometric approach. The approach relies on the use of artificial non-load bearing (NLB) layers attached to the load bearing (LB) layers with rigid beam connectors.

The working principle of the ABH metastructures was studied in Chapter 2. The chapter discussed a variety of transmission mechanisms and dispersion characteristics (like wide bandgap formation and low cut-on frequency) of the ABH metastructures that can be successfully leveraged for vibration attenuation in lightweight applications.

Chapter 3 presented the fundamentals of nonlocal elasticity theory, and introduced the concept of geometric nonlocality. Here, the conceptual analogy with a discrete nonlocal geometric model was exploited to build a continuous nonlocal plate model. This work also presented a semi-analytical approach to simulate the geometric nonlocal effect using a dynamic functional, known as the *nonlocal attenuation factor*. Unlike the traditional models with wavenumber dependent nonlocal material properties, the response of the geometrically nonlocal models vary also as a function of the excitation frequency, thus requiring a semi-analytical approach capable of extracting

a wavenumber and frequency dependent nonlocal attenuation factor. A procedure to solve the Rayleigh-Lamb dispersion equations was also developed in this chapter.

Chapter 4 presented numerical simulations of the dynamic response of the nonlocal ABH metastructures. The dispersion curves and the steady state frequency responses of the nonlocal structures were evaluated and compared using finite element simulations. The dispersion results revealed the existence of enlarged low frequency bandgaps in the nonlocal designs, while the ultra-low frequency flexural energy attenuation was illustrated via the steady state dynamic responses. Thus, these numerical results effectively characterized the attenuation behavior introduced by the engineered geometric nonlocality. Semi-analytical dispersion curves were also plotted by numerically solving the Rayleigh-Lamb equation using the frequency and the wavenumber dependent dynamic nonlocal attenuation factors. Both the semi-analytical and the numerical dispersion curves were in good agreement for the propagating dispersion bands at low frequencies. At high frequencies, the semi-analytical dispersion curves deviate from the results of the numerical simulation due to their inability to capture the complex dynamic response of the nonlocal ABH metastructure.

Overall, the theoretical and numerical results provided clear evidence of the potential of engineered nonlocal ABH metastructures as an efficient ultra-low frequency passive attenuation technique for lightweight systems.

5.2   Thesis Contributions

The major contributions of this thesis can be summarized as follows:

5.2.1   Engineered geometric nonlocality

The novel design concept of intentionally nonlocal metastructure was presented. The new design combines the ABH metastructures with geometrically tailored flexible layers to produce a nonlocal dynamic behavior. The new structural design creates multiple energy paths by connecting distant structural locations. This results in an

action at a distance equivalent to the concept of long range interactions.

Although the introduction of the nonlocal layer resulted in an additional weight penalty of 15% and 26% on both the flat and the tapered baseline plates respectively, the nonlocal designs with the tapered LB layer had 25% weight reduction in comparison to the flat baseline plate. Hence, the concept of vibration attenuation using the nonlocal ABH metastructure design is still a viable approach for lightweight structural applications.

5.2.2 Enhanced ultra-low frequency attenuation

The geometric nonlocal design was capable of attenuating structural vibrations in the ultra-low frequency range. The traditional ABH metastructure (tapered baseline plate) generates the first bandgap at a frequency around 170 Hz, while the proposed nonlocal ABH metastructure introduced bandgaps at frequencies as low as 2 Hz. The introduction of the nonlocal NLB layers enable bandgaps formation at ultra-low frequencies, and it allows controlling the bandwidth of these gaps by properly choosing the type of the NLB layer used in the nonlocal design. The ultra-low frequency bandgaps generated by a nonlocal structure with the ABH plate as the NLB layer is around four times the bandwidth of the gap produced by the same structure with the flat plate as the NLB layer. The application of viscoelastic damping layers on the tapers further enhanced the energy attenuation capabilities of these nonlocal ABH metastructures.

5.2.3 Semi-analytical model of the nonlocal ABH metastructures

In linear elasticity, the traditional material nonlocality is mathematically defined as a function of the location-dependent nonlocal attenuation factor. However, given that, in this thesis, the nonlocal behavior was obtained by the use of geometrically tailored physical connections, the nonlocal attenuation factor required a dependence from both temporal and the spatial variables. Hence, a semi-analytical methodology

was developed to extract these dynamic nonlocal attenuation factors.

The nonlocal constitutive relations formulated by Eringen and updated by Nowinski were modified to obtain new analytical relations governing the geometric nonlocal behavior. The parameters necessary to solve the analytical relations were calculated numerically. These parameters were substituted into the modified constitutive relations to evaluate the dynamic nonlocal attenuation factor. These factors were then used to plot the dispersion curves by numerically solving the Rayleigh-Lamb relations. The qualitative agreement between the semi-analytical and the numerical dispersion bands validated the effectiveness of this technique.

5.3   Recommendations For Future Work

While this work presented the idea of intentionally nonlocal metastructure and performed a feasibility study to asses its functioning, much work is still left in order to optimize both design and performance towards practical engineering applications. Some recommendations for future work are presented here below:

5.3.1   Optimization of the nonlocal design

This work mainly explored the novel idea and the potential of intentionally nonlocal ABH metastructures. Although the numerical simulations demonstrated the potential of the proposed approach, the design was not optimized for performance. The future work should focus on the identification of key design parameters and optimization strategies to maximize the attenuation performance. More specifically, one should explore the low frequency attenuation range, and optimize the dimensions and material preferences of the NLB and LB layers based on the general behavior described in this thesis. A strategy should be developed to optimize the position and thickness of the viscoelastic damping layer for enhanced flexural energy attenuation of the nonlocal ABH metastructures.

5.3.2   Development of multilayered hierarchical nonlocal model

In order to reduce the complexity of the design, the thesis focused on developing a single NLB layered nonlocal ABH metastructures. In the proposed designs, the structure directly transitioned from ten small tapers in the LB layer to one large taper on the NLB layer. It is believed that a multilayered (more than one NLB layers) hierarchical nonlocal ABH metastructure with gradual variation in the number, size, and position of the tapers would provide much benefit and fine tuning of the performance. A parametric study should be conducted to optimize the position of the rigid beam connectors between the multiple layers for efficient nonlocal damping.

5.3.3   Experimental investigation of the dynamic behavior of the nonlocal ABH metastructure

The main conclusions put forward in this thesis were based on a combination of theoretical and numerical analyses. An extensive experimental study should be conducted in order to study the physical response of the proposed thin walled nonlocal structures in the ultra-low frequency range to validate the models, asses the performance, and highlight any possible fabrication constraint.

REFERENCES

[1] S. Kim and J. Jones, "A study of piezoelectric actuators for active noise and vibration control," Ph.D. dissertation, 1992.

[2] S. S. Rao, *Vibration of continuous systems.* Wiley Online Library, 2007, vol. 464.

[3] M. H. Hansen, "Aeroelastic instability problems for wind turbines," *Wind Energy: An International Journal for Progress and Applications in Wind Power Conversion Technology*, vol. 10, no. 6, pp. 551–577, 2007.

[4] Y. Y. Yu, "Thermally induced vibration and flutter of a flexible boom." *Journal of Spacecraft and Rockets*, vol. 6, no. 8, pp. 902–910, 1969.

[5] H. Haddadpour, M. Kouchakzadeh, and F. Shadmehri, "Aeroelastic instability of aircraft composite wings in an incompressible flow," *Composite Structures*, vol. 83, no. 1, pp. 93–99, 2008.

[6] D. H. Hodges, M. J. Patil, and S. Chae, "Effect of thrust on bending-torsion flutter of wings," *Journal of Aircraft*, vol. 39, no. 2, pp. 371–376, 2002.

[7] NTSB, "Deteriorated parts allowed flutter which led to fatal crash at 2011 reno air races," https://www.ntsb.gov/news/press-releases/Pages/PR20120827.aspx.

[8] P. Gardonio, "Review of active techniques for aerospace vibro-acoustic control," *Journal of aircraft*, vol. 39, no. 2, pp. 206–214, 2002.

[9] H. K. Ozcan and S. Nemlioglu, "In-cabin noise levels during commercial aircraft flights," *Canadian Acoustics*, vol. 34, no. 4, pp. 31–35, 2006.

[10] A. D. Dimarogonas, "Vibration of cracked structures: a state of the art review," *Engineering fracture mechanics*, vol. 55, no. 5, pp. 831–857, 1996.

[11] A. Powell, "On the fatigue failure of structures due to vibrations excited by random pressure fields," *The Journal of the Acoustical Society of America*, vol. 30, no. 12, pp. 1130–1135, 1958.

[12] A. Grbovic and B. Rasuo, "Fem based fatigue crack growth predictions for spar of light aircraft under variable amplitude loading," *Engineering Failure Analysis*, vol. 26, pp. 50–64, 2012.

[13] NTSB, "Aircraft accident report: Braniff airways," http://libraryonline.erau.edu/online-full-text/ntsb/aircraft-accident-reports/AAR69-03.pdf.

[14] L. Cocco, P. Gazzola, S. Rapuano, and L. Rossi, "Vibrations measurements of formula one car electronic devices," 2008.

[15] H. H. Hubbard, "Aeroacoustics of flight vehicles: Theory and practice. volume 1. noise sources," Tech. Rep., 1991.

[16] E. J. Richards and D. Mead, *Noise and Fatigue in Aeronautics*. Wiley, 1968.

[17] B. Chemoul and E. Louaas, "Vibration and acoustic dimensioning of ariane launchers," in *Proc. The 2000 International Conference on Noise and Vibration Engineering*, 2000.

[18] R. Vaicaitis, "Noise transmission into a light aircraft," *Journal of Aircraft*, vol. 17, no. 2, pp. 81–86, 1980.

[19] R. Alkhatib and M. Golnaraghi, "Active structural vibration control: a review," *Shock and Vibration Digest*, vol. 35, no. 5, p. 367, 2003.

[20] Y.-R. Hu and A. Ng, "Active robust vibration control of flexible structures," *Journal of sound and vibration*, vol. 288, no. 1-2, pp. 43–56, 2005.

[21] J. C. Chang and T. T. Soong, "Structural control using active tuned mass dampers," *Journal of the Engineering Mechanics Division*, vol. 106, no. 6, pp. 1091–1098, 1980.

[22] S. Masri, G. Bekey, and T. Caughey, "On-line control of nonlinear flexible structures," *Journal of Applied Mechanics*, vol. 49, no. 4, pp. 877–884, 1982.

[23] R. Miller, S. Masri, T. Dehghanyar, and T. Caughey, "Active vibration control of large civil structures," *Journal of engineering mechanics*, vol. 114, no. 9, pp. 1542–1570, 1988.

[24] R. Klein, C. Cusano, and J. Stukel, "Investigation of a method to stabilize wind-induced oscillations in large structures," in *Mechanical engineering*, vol. 95, no. 2. ASME-AMER, 1973, pp. 53–53.

[25] T. Soong, "State-of-the-art review: active structural control in civil engineering," *Engineering Structures*, vol. 10, no. 2, pp. 74–84, 1988.

[26] J. Qiu, H. Ji, and K. Zhu, "Semi-active vibration control using piezoelectric actuators in smart structures," *Frontiers of Mechanical Engineering in China*, vol. 4, no. 3, pp. 242–251, 2009.

[27] V. BANKAR and A. Aradhye, "A review on active, semi-active and passive vibration damping," *International Journal of Current Engineering and Technology*, vol. 6, no. 6, pp. 1–5, 2016.

[28] L. Kela and P. Vähäoja, "Recent studies of adaptive tuned vibration absorbers/neutralizers," *Applied Mechanics Reviews*, vol. 62, no. 6, p. 060801, 2009.

[29] G. Pennisi, "Passive vibration control by using nonlinear energy sink absorbers. theoretical study and experimental investigations," Ph.D. dissertation, Institut superieur de l'eronautique et de l'espace (isae), 2016.

[30] J. D. Ferry, *Viscoelastic properties of polymers*. John Wiley & Sons, 1980.

[31] D. I. Jones, *Handbook of viscoelastic vibration damping*. John Wiley & Sons, 2001.

[32] C. D. Johnson, "Design of passive damping systems," *Journal of Mechanical Design*, vol. 117, no. B, pp. 171–176, 1995.

[33] J. D. Ferry, E. R. Fitzgerald, L. D. Grand, and M. L. Williams, "Temperature dependence of dynamic mechanical properties of elastomers, relaxation distributions," *Industrial & Engineering Chemistry*, vol. 44, no. 4, pp. 703–706, 1952.

[34] V. Denis, "Vibration damping in beams using the acoustic black hole effect," Ph.D. dissertation, Université du Maine, 2014.

[35] D. Mead, D. Zhu, and N. Bardell, "Free vibration of an orthogonally-stiffened flat plate," *Recent advances in structural dynamics*, p. 111, 1988.

[36] D. I. Jones, "Response and damping of a simple beam with tuned dampers," *The journal of the acoustical society of America*, vol. 42, no. 1, pp. 50–53, 1967.

[37] R. Adkins, D. Jones, and A. Nashif, "Effect of tuned dampers on vibrations of simple structures." *AIAA Journal*, vol. 5, no. 2, pp. 310–315, 1967.

[38] J. C. Snowdon, *Vibration and shock in damped mechanical systems.* J. Wiley, 1968.

[39] T. Pinkaew, P. Lukkunaprasit, and P. Chatupote, "Seismic effectiveness of tuned mass dampers for damage reduction of structures," *Engineering Structures*, vol. 25, no. 1, pp. 39–46, 2003.

[40] R. Rana and T. Soong, "Parametric study and simplified design of tuned mass dampers," *Engineering structures*, vol. 20, no. 3, pp. 193–204, 1998.

[41] T. E. Saaed, G. Nikolakopoulos, J.-E. Jonasson, and H. Hedlund, "A state-of-the-art review of structural control systems," *Journal of Vibration and Control*, vol. 21, no. 5, pp. 919–937, 2015.

[42] A. Sinha and J. Griffin, "Friction damping of flutter in gas turbine engine airfoils," *Journal of Aircraft*, vol. 20, no. 4, pp. 372–376, 1983.

[43] J. R. Fricke, "Lodengraf damping: An advanced vibration damping technology," *SV Sound and vibration*, vol. 34, no. 7, pp. 22–27, 2000.

[44] A. Sinha and J. Griffin, "Stability of limit cycles in frictionally damped and aerodynamically unstable rotor stages," *Journal of Sound and Vibration*, vol. 103, no. 3, pp. 341–356, 1985.

[45] H. Panossian, "Structural damping enhancement via non-obstructive particle damping technique," *Journal of Vibration and Acoustics*, vol. 114, no. 1, pp. 101–105, 1992.

[46] O. Romberg, M. Tausche, C. Pereira, and L. Panning, "Passive damping of spacecraft sandwich panels," in *10th European Conference on Spacecraft Structures, Materials & Mechanical Testing*, 2007, pp. 10–13.

[47] X. Fang, J. Tang, and H. Luo, "Granular damping analysis using an improved discrete element approach," *Journal of Sound and Vibration*, vol. 308, no. 1-2, pp. 112–131, 2007.

[48] W. Liu, G. Tomlinson, and J. Rongong, "The dynamic characterisation of disk geometry particle dampers," *Journal of Sound and Vibration*, vol. 280, no. 3-5, pp. 849–861, 2005.

[49] C. Wong, M. Daniel, and J. Rongong, "Energy dissipation prediction of particle dampers," *Journal of Sound and Vibration*, vol. 319, no. 1-2, pp. 91–118, 2009.

[50] K. Mao, M. Y. Wang, Z. Xu, and T. Chen, "Simulation and characterization of particle damping in transient vibrations," *Journal of vibration and acoustics*, vol. 126, no. 2, pp. 202–211, 2004.

[51] A. Papalou, E. Strepelias, D. Roubien, S. Bousias, and T. Triantafillou, "Seismic protection of monuments using particle dampers in multi-drum columns," *Soil Dynamics and Earthquake Engineering*, vol. 77, pp. 360–368, 2015.

[52] S. Ashley, "A new racket shakes up tennis," *Mechanical Engineering-CIME*, vol. 117, no. 8, pp. 80–82, 1995.

[53] D. Chronopoulos, B. Troclet, O. Bareille, and M. Ichchou, "Modeling the response of composite panels by a dynamic stiffness approach," *Composite Structures*, vol. 96, pp. 111–120, 2013.

[54] D. Chronopoulos, M. Ichchou, B. Troclet, and O. Bareille, "Efficient prediction of the response of layered shells by a dynamic stiffness approach," *Composite Structures*, vol. 97, pp. 401–404, 2013.

[55] J.-L. Guyader and C. Lesueur, "Acoustic transmission through orthotropic multilayered plates, part i: Plate vibration modes," *Journal of Sound and Vibration*, vol. 58, no. 1, pp. 51–68, 1978.

[56] C. Vemula, A. Norris, and G. Cody, "Attenuation of waves in plates and bars using a graded impedance interface at edges," *Journal of Sound and Vibration*, vol. 196, no. 1, pp. 107–127, 1996.

[57] L. Cremer and M. Heckl, *Structure-borne sound: structural vibrations and sound radiation at audio frequencies.* Springer Science & Business Media, 2013.

[58] M. Mironov, "Propagation of a flexural wave in a plate whose thickness decreases smoothly to zero in a finite interval," pp. 318–319, 1988.

[59] S. Conlon, F. Semperlotti, and J. Fahnline, "Passive control of vibration and sound transmission for vehicle structures via embedded acoustic black holes," in *INTER-NOISE and NOISE-CON Congress and Conference Proceedings*, vol. 246, no. 1. Institute of Noise Control Engineering, 2013, pp. 176–184.

[60] S. C. Conlon, J. B. Fahnline, F. Semperlotti, and P. A. Feurtado, "Enhancing the low frequency vibration reduction performance of plates with embedded acoustic black holes," in *INTER-NOISE and NOISE-CON Congress and Conference Proceedings*, vol. 249, no. 8. Institute of Noise Control Engineering, 2014, pp. 175–182.

[61] C. Pekeris, "Theory of propagation of sound in a half-space of variable sound velocity under conditions of formation of a shadow zone," *The Journal of the Acoustical Society of America*, vol. 18, no. 2, pp. 295–315, 1946.

[62] V. V. Krylov, "Acoustic'black holes' for flexural waves and their potential applications," 2002.

[63] H. Zhu and F. Semperlotti, "Phononic thin plates with embedded acoustic black holes," *Physical Review B*, vol. 91, no. 10, p. 104304, 2015.

[64] V. Krylov, "Laminated plates of variable thickness as effective absorbers for flexural vibrations," in *Proceedings of the 17th International Congress on Acoustics*, 2001, pp. 270–271.

[65] P. A. Feurtado, S. C. Conlon, and F. Semperlotti, "A normalized wave number variation parameter for acoustic black hole design," *The Journal of the Acoustical Society of America*, vol. 136, no. 2, pp. EL148–EL152, 2014.

[66] V. Denis, F. Gautier, A. Pelat, and J. Poittevin, "Measurement and modelling of the reflection coefficient of an acoustic black hole termination," *Journal of Sound and Vibration*, vol. 349, pp. 67–79, 2015.

[67] V. Denis, A. Pelat, and F. Gautier, "Scattering effects induced by imperfections on an acoustic black hole placed at a structural waveguide termination," *Journal of Sound and Vibration*, vol. 362, pp. 56–71, 2016.

[68] L. Zhao, S. C. Conlon, and F. Semperlotti, "Broadband energy harvesting using acoustic black hole structural tailoring," *Smart materials and structures*, vol. 23, no. 6, p. 065021, 2014.

[69] A. Pelat, F. Gautier, F. Semperlotti, and S. Conlon, "Passive control of vibrations using acoustic black holes," in *INTER-NOISE and NOISE-CON Congress and Conference Proceedings*, vol. 255, no. 2. Institute of Noise Control Engineering, 2017, pp. 5789–5798.

[70] L. Zhao, S. C. Conlon, and F. Semperlotti, "An experimental study of vibration based energy harvesting in dynamically tailored structures with embedded acoustic black holes," *Smart Materials and Structures*, vol. 24, no. 6, p. 065039, 2015.

[71] C. Zhao and M. G. Prasad, "Acoustic black holes in structural design for vibration and noise control," in *Acoustics*, vol. 1, no. 1. Multidisciplinary Digital Publishing Institute, 2019, pp. 220–251.

[72] V. V. Krylov, "Acoustic black holes for flexural waves: A smart approach to vibration damping," *Procedia engineering*, vol. 199, pp. 56–61, 2017.

[73] E. Bowyer, V. Krylov, and D. O'Boy, "Damping of flexural vibrations in rectangular plates by slots of power-law profile," in *Acoustics 2012*, 2012.

[74] E. Bowyer and V. V. Krylov, "Damping of flexural vibrations in turbofan blades using the acoustic black hole effect," *Applied Acoustics*, vol. 76, pp. 359–365, 2014.

[75] F. Gautier, J. Cuenca, V. V. Krylov, and L. Simon, "Experimental investigation of the acoustic black hole effect for vibration damping in elliptical plates," *Journal of the Acoustical Society of America*, vol. 123, no. 5, p. 3318, 2008.

[76] J. Cuenca, "Wave models for the flexural vibrations of thin plates," Ph.D. dissertation, Citeseer, 2009.

[77] V. Georgiev, J. Cuenca, F. Gautier, L. Simon, and V. Krylov, "Damping of structural vibrations in beams and elliptical plates using the acoustic black hole effect," *Journal of sound and vibration*, vol. 330, no. 11, pp. 2497–2508, 2011.

[78] L. Brillouin, *Wave propagation in periodic structures: electric filters and crystal lattices*.   Courier Corporation, 2003.

[79] Y. Xiao, J. Wen, D. Yu, and X. Wen, "Flexural wave propagation in beams with periodically attached vibration absorbers: band-gap behavior and band formation mechanisms," *Journal of Sound and Vibration*, vol. 332, no. 4, pp. 867–893, 2013.

[80] D. J. Mead, "Free wave propagation in periodically supported, infinite beams," *Journal of Sound and Vibration*, vol. 11, no. 2, pp. 181–197, 1970.

[81] S. Rytov, "Electromagnetic properties of a finely stratified medium," *Soviet Physics JEPT*, vol. 2, pp. 466–475, 1956.

[82] M.-H. Lu, L. Feng, and Y.-F. Chen, "Phononic crystals and acoustic metamaterials," *Materials today*, vol. 12, no. 12, pp. 34–42, 2009.

[83] S. Chen, Y. Fan, Q. Fu, H. Wu, Y. Jin, J. Zheng, and F. Zhang, "A review of tunable acoustic metamaterials," *Applied Sciences*, vol. 8, no. 9, p. 1480, 2018.

[84] B.-I. Popa, L. Zigoneanu, and S. A. Cummer, "Tunable active acoustic metamaterials," *Physical Review B*, vol. 88, no. 2, p. 024303, 2013.

[85] T. J. Cui, S. Liu, and L. Zhang, "Information metamaterials and metasurfaces," *Journal of Materials Chemistry C*, vol. 5, no. 15, pp. 3644–3668, 2017.

[86] G. Ma and P. Sheng, "Acoustic metamaterials: From local resonances to broad horizons," *Science advances*, vol. 2, no. 2, p. e1501595, 2016.

[87] F. Qin, L. Ding, L. Zhang, F. Monticone, C. C. Chum, J. Deng, S. Mei, Y. Li, J. Teng, M. Hong *et al.*, "Hybrid bilayer plasmonic metasurface efficiently manipulates visible light," *Science advances*, vol. 2, no. 1, p. e1501168, 2016.

[88] Y. Pang, J. Wang, Q. Cheng, S. Xia, X. Y. Zhou, Z. Xu, T. J. Cui, and S. Qu, "Thermally tunable water-substrate broadband metamaterial absorbers," *Applied Physics Letters*, vol. 110, no. 10, p. 104103, 2017.

[89] Z. Wang, L. Jing, K. Yao, Y. Yang, B. Zheng, C. M. Soukoulis, H. Chen, and Y. Liu, "Origami-based reconfigurable metamaterials for tunable chirality," *Advanced Materials*, vol. 29, no. 27, p. 1700412, 2017.

[90] Y. Fan, Z. Wei, H. Li, H. Chen, and C. M. Soukoulis, "Low-loss and high-q planar metamaterial with toroidal moment," *Physical Review B*, vol. 87, no. 11, p. 115417, 2013.

[91] Z. Liu, S. Du, A. Cui, Z. Li, Y. Fan, S. Chen, W. Li, J. Li, and C. Gu, "High-quality-factor mid-infrared toroidal excitation in folded 3d metamaterials," *Advanced Materials*, vol. 29, no. 17, p. 1606298, 2017.

[92] M. Sigalas and E. N. Economou, "Band structure of elastic waves in two dimensional systems," *Solid state communications*, vol. 86, no. 3, pp. 141–143, 1993.

[93] M. S. Kushwaha, P. Halevi, L. Dobrzynski, and B. Djafari-Rouhani, "Acoustic band structure of periodic elastic composites," *Physical review letters*, vol. 71, no. 13, p. 2022, 1993.

[94] M. S. Kushwaha, P. Halevi, G. Martinez, L. Dobrzynski, and B. Djafari-Rouhani, "Theory of acoustic band structure of periodic elastic composites," *Physical Review B*, vol. 49, no. 4, p. 2313, 1994.

[95] Z. Liu, C. T. Chan, and P. Sheng, "Analytic model of phononic crystals with local resonances," *Physical Review B*, vol. 71, no. 1, p. 014103, 2005.

[96] C. Croënne, E. Lee, H. Hu, and J. Page, "Band gaps in phononic crystals: Generation mechanisms and interaction effects," *AIP Advances*, vol. 1, no. 4, p. 041401, 2011.

[97] R. Martínez-Sala, J. Sancho, J. V. Sánchez, V. Gómez, J. Llinares, and F. Meseguer, "Sound attenuation by sculpture," *nature*, vol. 378, no. 6554, p. 241, 1995.

[98] B. Morvan, A. Tinel, A.-C. Hladky-Hennion, J. Vasseur, and B. Dubus, "Experimental demonstration of the negative refraction of a transverse elastic wave in a two-dimensional solid phononic crystal," *Applied Physics Letters*, vol. 96, no. 10, p. 101905, 2010.

[99] A. S. Gliozzi, M. Miniaci, F. Bosia, N. M. Pugno, and M. Scalerandi, "Metamaterials-based sensor to detect and locate nonlinear elastic sources," *Applied Physics Letters*, vol. 107, no. 16, p. 161902, 2015.

[100] W. Kan, V. M. García-Chocano, F. Cervera, B. Liang, X.-y. Zou, L.-l. Yin, J. Cheng, and J. Sánchez-Dehesa, "Broadband acoustic cloaking within an arbitrary hard cavity," *Physical Review Applied*, vol. 3, no. 6, p. 064019, 2015.

[101] B. Gurevich and S. Lopatnikov, "Velocity and attenuation of elastic waves in finely layered porous rocks," *Geophysical Journal International*, vol. 121, no. 3, pp. 933–947, 1995.

[102] M. A. Biot, "Theory of propagation of elastic waves in a fluid-saturated porous solid. ii. higher frequency range," *The Journal of the acoustical Society of america*, vol. 28, no. 2, pp. 179–191, 1956.

[103] K. A. Wear, "A stratified model to predict dispersion in trabecular bone," *IEEE transactions on ultrasonics, ferroelectrics, and frequency control*, vol. 48, no. 4, pp. 1079–1083, 2001.

[104] B. Berkowitz and H. Scher, "On characterization of anomalous dispersion in porous and fractured media," *Water Resources Research*, vol. 31, no. 6, pp. 1461–1466, 1995.

[105] A. Stulov and V. I. Erofeev, "Frequency-dependent attenuation and phase velocity dispersion of an acoustic wave propagating in the media with damages," in *Generalized Continua as Models for Classical and Advanced Materials*. Springer, 2016, pp. 413–423.

[106] A. C. Eringen, "Linear theory of nonlocal elasticity and dispersion of plane waves," *International Journal of Engineering Science*, vol. 10, no. 5, pp. 425–435, 1972.

[107] E. Kröner, "Elasticity theory of materials with long range cohesive forces," *International Journal of Solids and Structures*, vol. 3, no. 5, pp. 731–742, 1967.

[108] J. Nowinski, "On the non-local aspects of stress in a viscoelastic medium," *International journal of non-linear mechanics*, vol. 21, no. 6, pp. 439–446, 1986.

[109] C. Lim, G. Zhang, and J. Reddy, "A higher-order nonlocal elasticity and strain gradient theory and its applications in wave propagation," *Journal of the Mechanics and Physics of Solids*, vol. 78, pp. 298–313, 2015.

[110] C. Polizzotto, "Nonlocal elasticity and related variational principles," *International Journal of Solids and Structures*, vol. 38, no. 42-43, pp. 7359–7380, 2001.

[111] Z. P. Bažant and M. Jirásek, "Nonlocal integral formulations of plasticity and damage: survey of progress," *Journal of Engineering Mechanics*, vol. 128, no. 11, pp. 1119–1149, 2002.

[112] R. Peerlings, M. Geers, R. De Borst, and W. Brekelmans, "A critical comparison of nonlocal and gradient-enhanced softening continua," *International Journal of solids and Structures*, vol. 38, no. 44-45, pp. 7723–7746, 2001.

[113] E. C. Aifantis, "Update on a class of gradient theories," *Mechanics of materials*, vol. 35, no. 3-6, pp. 259–280, 2003.

[114] S. A. Silling, "Reformulation of elasticity theory for discontinuities and long-range forces," *Journal of the Mechanics and Physics of Solids*, vol. 48, no. 1, pp. 175–209, 2000.

[115] S. A. Silling, M. Zimmermann, and R. Abeyaratne, "Deformation of a peridynamic bar," *Journal of Elasticity*, vol. 73, no. 1-3, pp. 173–190, 2003.

[116] J. Nowinski, "On the nonlocal theory of wave propagation in elastic plates," *Journal of Applied Mechanics*, vol. 51, no. 3, pp. 608–613, 1984.

[117] V. Krylov and F. Tilman, "Acoustic 'black holes' for flexural waves as effective vibration dampers," *Journal of Sound and Vibration*, vol. 274, no. 3-5, pp. 605–619, 2004.

[118] C. Zhao and M. Prasad, "Studies on sound radiation from beams with acoustic black holes," in *INTER-NOISE and NOISE-CON Congress and Conference Proceedings*, vol. 252, no. 2. Institute of Noise Control Engineering, 2016, pp. 713–719.

[119] V. V. Krylov, "Propagation of plate bending waves in the vicinity of one-and two-dimensional acoustic 'black holes'," 2007.

[120] P. Kravchun, "Generation and methods of reduction of noise and vibration," 1991.

[121] V. V. Krylov and R. Winward, "Experimental investigation of the acoustic black hole effect for flexural waves in tapered plates," *Journal of Sound and Vibration*, vol. 300, no. 1-2, pp. 43–49, 2007.

[122] D. O'Boy, E. P. Bowyer, and V. V. Krylov, "Damping of flexural vibrations in thin plates using one and two dimensional acoustic black hole effect," 2010.

[123] P. A. Feurtado and S. C. Conlon, "An experimental investigation of acoustic black hole dynamics at low, mid, and high frequencies," *Journal of Vibration and Acoustics*, vol. 138, no. 6, p. 061002, 2016.

[124] V. Kralovic and V. V. Krylov, "Damping of flexural vibrations in tapered rods of power-law profile: Experimental studies," 2007.

[125] ——, "Some new methods of damping impact-induced vibrations in badminton racquets," 2008.

[126] Z. Hou and B. M. Assouar, "Modeling of lamb wave propagation in plate with two-dimensional phononic crystal layer coated on uniform substrate using plane-wave-expansion method," *Physics Letters A*, vol. 372, no. 12, pp. 2091–2097, 2008.

[127] L. K. Lamontagne, "Band structures and the meaning of the wave vector k."

[128] J. S. for Strength and F. of Materials, *Proceedings of the first international conference on fracture.* The Japanese Society for Strength and Fracture of Materials, 1966, vol. 1.

[129] E. . D. Kröner, "BKZ Physik (1966) 196: 203," https://doi.org/10.1007/BF01330987.

[130] M. Di Paola, G. Failla, and M. Zingales, "Physically-based approach to the mechanics of strong non-local linear elasticity theory," *Journal of Elasticity*, vol. 97, no. 2, pp. 103–130, 2009.

[131] C. R. Steele and C. D. Balch, "Introduction to the theory of plates," *Lecture Notes, Stanford University, Department of Mechanical Engineering, Division of Mechanics and Computation*, pp. 1–41, 2009.

[132] S. P. Timoshenko and S. Woinowsky-Krieger, *Theory of plates and shells.* McGraw-hill, 1959.

[133] M. Šofer, P. Ferfecki, and P. Šofer, "Numerical solution of rayleigh-lamb frequency equation for real, imaginary and complex wavenumbers," in *MATEC Web of Conferences*, vol. 157. EDP Sciences, 2018, p. 08011.

[134] Z. Liu, X. Zhang, Y. Mao, Y. Zhu, Z. Yang, C. T. Chan, and P. Sheng, "Locally resonant sonic materials," *science*, vol. 289, no. 5485, pp. 1734–1736, 2000.

[135] S. Yang, J. H. Page, Z. Liu, M. Cowan, C. T. Chan, and P. Sheng, "Ultrasound tunneling through 3d phononic crystals," *Physical review letters*, vol. 88, no. 10, p. 104301, 2002.

[136] H. Sanchis-Alepuz, Y. A. Kosevich, and J. Sánchez-Dehesa, "Acoustic analogue of electronic bloch oscillations and resonant zener tunneling in ultrasonic superlattices," *Physical review letters*, vol. 98, no. 13, p. 134301, 2007.

[137] D. Garcia-Pablos, M. Sigalas, F. M. De Espinosa, M. Torres, M. Kafesaki, and N. Garcia, "Theory and experiments on elastic band gaps," *Physical review letters*, vol. 84, no. 19, p. 4349, 2000.

[138] J. Vasseur, P. A. Deymier, B. Chenni, B. Djafari-Rouhani, L. Dobrzynski, and D. Prevost, "Experimental and theoretical evidence for the existence of absolute acoustic band gaps in two-dimensional solid phononic crystals," *Physical Review Letters*, vol. 86, no. 14, p. 3012, 2001.

[139] M. Torres, F. M. De Espinosa, D. Garcia-Pablos, and N. Garcia, "Sonic band gaps in finite elastic media: surface states and localization phenomena in linear and point defects," *Physical Review Letters*, vol. 82, no. 15, p. 3054, 1999.

[140] M. Kafesaki, M. Sigalas, and N. Garcia, "Frequency modulation in the transmittivity of wave guides in elastic-wave band-gap materials," *Physical Review Letters*, vol. 85, no. 19, p. 4044, 2000.

[141] A. Khelif, B. Djafari-Rouhani, J. Vasseur, and P. A. Deymier, "Transmission and dispersion relations of perfect and defect-containing waveguide structures in phononic band gap materials," *Physical Review B*, vol. 68, no. 2, p. 024302, 2003.

[142] D. Morin, "Dispersion," http://www.people.fas.harvard.edu/~djmorin/waves/dispersion.pdf, [Online; accessed 12-July-2019].

A. APPENDIX

A.1 Characteristics of Dispersion Curves

This section focuses on illustrating the characteristic features of a dispersion curve. Disperion curves are obtained by relating wavenumbers (k) of propagating wave to its frequencies (ω) in periodic structures. Periodic arrangement of scatterers and their material properties define flexural wave propagation pattern in these structures.

As described in the literature in previous chapters, dynamic behavior of periodic ABH metastructures have been the domain of study for sometime now. This section will only introduce the major characteristics of dispersion with simple 1D periodic systems, readers can go through [63, 134–141] for detailed review on dispersion curves of complex ABH metastructures.

Initially, the wave propagation in discrete 1D chain of atoms is studied in order to understand the band formation concepts in dispersion curves. As dispersion relation for the atomic scale systems involve quantum effects, the first section will use 1D chain of atoms only to describe the basic dispersion band characteristics applicable for systems of all size scales. Further, the dispersion relation for wave propagation in strings is introduced in order to analyze flexural wave characteristics through a simple continuous medium.

A.1.1 Bloch theorem, Brillouin zone and Bragg's criterion: 1D array of atoms

Let us assume a 1D chain of N atoms separated by a distance a each, a periodic boundary condition is enforced such that the Nth atom of the $N - 1^{th}$ chain is linked

to the 1st atom of the Nth chain. This periodic connection can be mathematically represented by a wave function, ϕ, as:

$$\phi(x) = \phi(x + Na) \tag{A.1}$$

For a uniform periodic chain with constant interatomic distance, the electron density (ρ) for individual atom on the chain will remain same, i.e $\rho(x + a) = \rho(x)$. As per band structure theory presented by Lamontagne [127], we know $\rho(x) = \phi^*(x)\phi(x)$ (here * represents conjugate) is real. A complex entity μ with $\mu^*\mu = 1$ will satisfy the $\phi(x + a) = \mu\phi(x)$ relation [127]. Further, this relation can be extended for N atoms as $\phi(x + Na) = \mu^N\phi(x)$. Comparing Eq. (A.1) with $\phi(x + Na) = \mu^N\phi(x)$, we get:

$$\mu = e^{i2\pi p/N} = cos\left(\frac{2\pi p}{N}\right) + isin\left(\frac{2\pi p}{N}\right) \tag{A.2}$$

where p is a number varying in [-N, N] and wavenumber is defined as $k = 2\pi p/(Na)$, varying as a function of number of atoms (N) involved. With the solution to wave function, $\phi(x) = e^{ikx}$, and with the perioidic relation, $\phi(x + a) = e^{ika}\phi(x)$, we can generalize the wave function interms of a periodic displacement relation $u(x) = u(x + a)$ as follows:

$$\phi(x) = e^{ikx}u(x) \tag{A.3}$$

The above relation for ϕ (Eq. (A.3)) is termed as *Bloch function*. The function depends on the wavenumber (k) as well as on the periodic displacement function ($u(x)$). Based on Bloch function, it is known that at $k = 0$ the structure is swamped by an infinite wavelength and each unit cell would be in phase with the other, while at $k = \pm\pi/a$, the propagating waves will pass through nodes and therefore the unit cells would be out of phase with one another.

The Bloch or Floquet condition (Eq. (A.3)) governs the propagation of acoustic waves in the periodic structures. The Bloch theorem develops the band structure for the phononic crystals or array of atoms within a phase space known as *Brillouin zone*.

The Brillouin zone can be defined as a primitive unit cell in a reciprocal phase space of the periodic structure. From the definition of the periodic lattice, it is known that the wavenumbers in the Brillouin zone must satisfy $e^{ika} = 1$ [127]. Thus, in the k-space, the first Brillouin zone is defined from $(-\pi/a, \pi/a)$. The first Brillouin zone, also known as the *Wigner-Seitz* primitive cell of lattice structure, passes through the entire range of k-space from the origin without crossing a single Brillouin boundary or also known as *Bragg plane.* Second Brillouin zone encounters waves propagating through one Bragg plane. Similarly, the Nth Brillouin zone will constitute of all the points from the origin in k-space with the wave passing through $N - 1$ Bragg planes. On generalizing this band trends and plotting dispersion curves for the array of atoms, it is found that the Bragg planes correspond to the position of band gap initiation for the chain. The wavelength (λ) at the band gap is related to the unit cell distance (a) by *Bragg's crietrion* as shown below:

$$a = n\frac{\lambda}{2} \qquad where \ \ n = 1, 2, 3 \tag{A.4}$$

The Bloch's (Floquet) theorem, the Brillouin zone and the Bragg's criterion govern the formation of the basic band structure and the dispersion curve for an array of atoms. Analogous to the propagation of electron wave in the chain of atoms, the elastic wave propagation in solid structures also have the same basic dispersion characteristics. A unit cell in a periodic ABH metastructure can be analogized to a single atom in the atomic chain. Hence, the Floquent boundary conditions, the Brillouin boundaries and the Bragg's criteria will also govern the characteristic features for band formation in dispersion of periodic ABH metastructures.

A.1.2 Dispersion bands in a continuous system: mass embedded infinite string

This section will introduce the elastic wave propagation characteristics through a simple continuous medium of *infinite string* and will elaborate its dispersion behavior. Wave propagation in a continuous string is mathematically represented as:

$$\frac{\partial^2 \phi}{\partial t^2} = c^2 \frac{\partial^2 \phi}{\partial x^2} \tag{A.5}$$

where ϕ is the wave function and c is the wave velocity.

Substituting an assumed exponential approximation, $\phi = A\, e^{i(kx - \omega t)}$, and solving the wave equation (Eq. (A.5)), generates the dispersion relation for wave propagation in infinite string as $\omega = ck$. The linear relationship between ω and k of the form $c = \omega/k$ represents the trivial continuous system with no dispersion. In such systems, the phase and group velocities (c_p and c_g respectively) of the propagating wave, indicated by slope of the dispersion curves, are always equal i.e $c_p = c_g$. Unlike a dispersionless continuous string, most real periodic structures have dispersive wave propagation properties and varying phase and group velocities.

Consider a continuous string with beads of mass m embedded periodically over a distance a as shown in Fig. (A.1). Let us assume a flexural wave propagation along the length of the string with tension T. The dispersion relation for this periodic structure is given by [142]:

$$\omega(k) = 2\omega_0 sin(\frac{ka}{2}) \tag{A.6}$$

where $\omega_0 = \left(\frac{T}{ma}\right)^{\frac{1}{2}}$. Reader can refer [142] for complete derivation.

Eq. (A.8) is a non linear relation between angular frequency and wavenumber and hence is dispersive in nature. Wave propagation in the dispersive structures constitute flexural waves traveling at varied velocities. The phase velocity (c_p) is defined as the velocity of a single propagating wave in the structure. Whereas, in places were complete wave is a superposition of numerous propagation waves, we have two veloc-
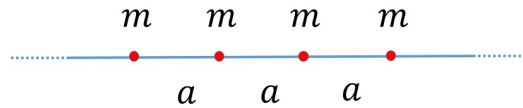
Fig. A.1.: Infinite string with beads of mass m embedded at a distance from each other. *Adapted from* [142].

ities in dispersion medium: a phase velocity for individual wave and a group velocity (c_g) for superpositioned flexural wave propagating through the structure. Although different waves travel at different speeds, it is found that the sum of all the fourier components of waves in superposition move with a single velocity known as the group velocity, $c_g = \dfrac{d\omega}{dk}$ (instantaneous slope). The group velocities reduce in amplitude and flattens out with time near Brillouin boundaries. Thus, dispersing out and hence the name dispersion.

In deriving the real wavenumber (k_{Re}) solution of the wave equation for continuous string with beads, we assume the angular frequency $\omega \leq 2\omega_0$. Real solutions as in Eq. (A.7) correspond to the *propagating bands* of dispersion curves as shown in Fig. (A.2). Further, it is also possible to excite the structures at a frequency higher than $2\omega_0$. If $\omega > 2\omega_0$, the string wave equation (Eq. (A.5)) will generate an exponentially decaying solution (Eq. (A.8)) with imaginary wavenumbers (k_{Im}). These waves are called *evanescent waves*.

Propagating wave:

$$\phi(x,t) = A \, cos(kx - \omega t) \tag{A.7}$$

Evanescent wave:

$$\phi(x,t) = B \, e^{(kx - \omega t)} \tag{A.8}$$

Standing wave:

$$\phi(x,t) = A e^{-\kappa x}(-1)^{x/a} cos(\omega t) \tag{A.9}$$

In Eq. (A.9), time and space variables independent of each other. As time passes, as per Eq. (A.9), waves will expand and contract with applied frequency as the wave

traveling distance (x) is an integral multiple of unit cell length (a), i.e x=na, and there exists a phase difference among the waves incident at the adjacent masses as represented by $(-1)^{x/a}$. As these waves have time independent spatial motion they do not travel and hence are called *standing waves* in dispersion curves. Pure evanescent waves and standing waves developed in periodic structures can be portrayed as band gaps on the dispersion curves (Fig. (A.2)) .
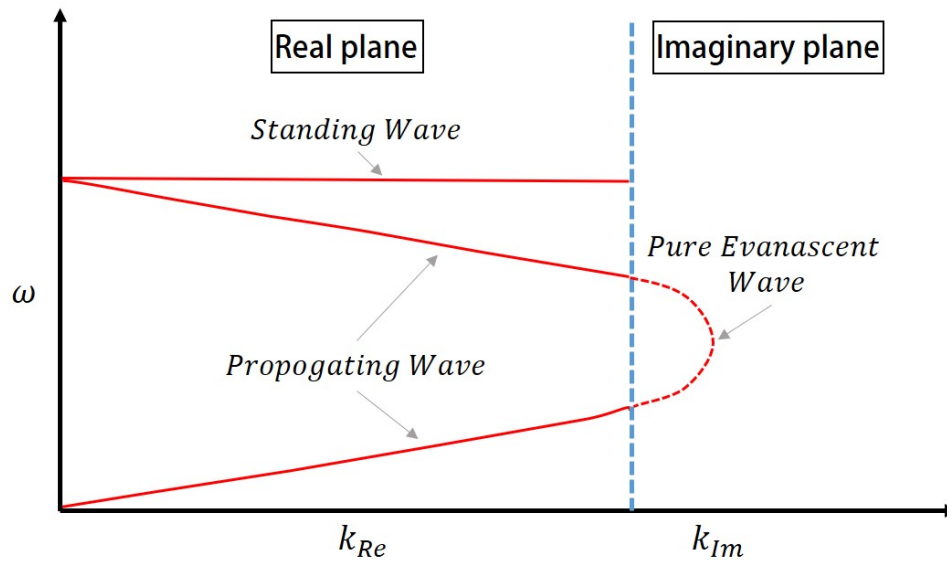

Fig. A.2.: Schematic illustrates a sample dispersion curve with angular frequency, ω, on y-axis and real and imaginary wavenumbers, k_{Re} and k_{Im} respectively, on the x-axis. The sample dispersion bands correspond to the propagating, standing and pure evanescent waves developed on an assumed structure (not necessarily on a string).

Formulating dispersion relations, understanding its theoretical working and learning the concepts for comprehending dispersion bands would essentially help to solve the dispersion relations and plot the dispersion curves of the ABH metastructures developed in the next chapter of this dissertation.